



THESE DE DOCTORAT DE SORBONNE UNIVERSITE

Spécialité

Electroniques et Communications

Ecole doctorale

EDITE ED 130

Présentée par

Fangqing Xiao

Pour obtenir le grade de DOCTEUR de SORBONNE UNIVERSITE

Sujet de la thèse:

Enhanced Power Delay Profile Estimation and Multipath-Aware Sensing for Next-Generation ISAC

soutenue le 02/10/2025

devant le jury composé de :

Prof. Dirk Slock	EURECOM, FR	Directeur de thèse
Prof. Laura Cottatellucci	FAU Erlangen-Nürnberg, DE	Rapporteure/Examinatrice
Prof. Benoit Denis	CEA-Leti, FR	Rapporteur/ Examinateur
Prof. Jérôme Härri	EURECOM, FR	Examinateur
Prof. Luc Deneire	Université Côte d'Azur, FR	Examinateur
Prof. Christoph Mecklenbräuker	TU Wien, AT	Examinateur

Contents

Re	ésum	. é		5
A۱	bstra	ct		7
A	cknov	wledge	ment	9
Li	st of	Symb	ols	10
Li	st of	Abbre	eviations	12
Li	st of	Figure	es	14
Li	st of	Tables	S	15
1	Intr 1.1 1.2	Relate 1.2.1 1.2.2 1.2.3	round and Motivation	16 18 18 20 21 22
2			ntal Limits of RSS and PDP-Based Ranging: A Cramér–Rac	
			rspective	24
	2.1		uction	24
	2.2	Conve 2.2.1	ntional Ranging Approaches and the Case for PDP	$\frac{25}{25}$
		2.2.1 $2.2.2$	Time-Based Ranging Methods	26 26
		2.2.2	Empirical CSI-Based Ranging	$\frac{20}{27}$
		2.2.4	PDP-Based Ranging	27
	2.3		m Model and Statistical Assumptions	28
	2.4		for RSS-based Ranging and PDP-based Ranging	30
		2.4.1	Joint Range Estimation CRB for PDP-Based Ranging	30
		2.4.2	Marginalized Range Estimation CRB for PDP-Based Ranging	32
		2.4.3	CRB For Classical RSSI-Based Ranging	33
	2.5		rical Results and Analysis	34
	2.6	Concli	usions	36

3			n in Linear Systems: From Sparse Recovery to Bayesian In-	
	fere	ence		37
	3.1		uction	37
	3.2	-	Estimation without Prior: Underdetermined Linear Systems	38
		3.2.1	Orthogonal Matching Pursuit (OMP)	38
		3.2.2	Approximate Message Passing (AMP)	39
		3.2.3	Sparse Bayesian Learning (SBL)	40
	3.3		MMSE Estimation and Gaussian Approximation	44
		3.3.1	MMSE Estimation under Gaussian Prior	44
		3.3.2	LMMSE for Non-Gaussian Prior via Gaussian Approximation	44
		3.3.3	Scalar Observation Model with Extrinsic Gaussian Noise	45
		3.3.4	Iterative Gaussian Approximation from Posterior Beliefs	46
	3.4	_	tation-Maximization with Prior Hyperparameter Estimation	48
		3.4.1	Marginal Likelihood and Variational Lower Bound	48
		3.4.2	EM Algorithm for Prior Hyperparameter Learning	48
		3.4.3	Approximate E-Step via Moment Matching	49
	3.5	Conclu	asions	49
4	Hig	h-Reso	olution Power Delay Profile Estimation with Sparse Bayesian	
-		erence	ration I over Belay I forme Estimation with Sparse Bayesian	51
	4.1		uction	51
	4.2		n Model	52
	4.3		rid Sparse Bayesian Inference	54
		4.3.1	Sparse Bayesian Formulation	54
		4.3.2	Stein's Unbiased Risk Estimator for Estimating γ	55
		4.3.3	Expectation Propagation for Estimating $\boldsymbol{\beta}$	56
		4.3.4	Noise Variance λ Estimation	57
		4.3.5	SURE-SBL-EP Delay Estimation Algorithm	57
	4.4	Numer	rical Simulation	57
	4.5	Conclu	asions	59
5	Mu	ltinath	Component Power Delay Profile Based Ranging	61
0	5.1	-	uction	61
	5.2		n model	62
	5.3	·	v of Expectation Maximization (EM)	65
	5.4		ted Vector Approximate Message Passing (ReVAMP)	66
		5.4.1	Extrinsic to variable nodes	68
		5.4.2	Passing the Approximation to the Factor Node	69
		5.4.3	Relation to Expectation Propagation (EP)	70
		5.4.4	Implementation Details	70
	5.5	Rangii	ng estimation with Nakagami-m prior distribution	71
		5.5.1	MPCPDP-based Ranging Method	71
		5.5.2	Theoretical Cramer-Rao Bound (CRB) For $m = 1 \dots \dots$	72
	5.6	Simula	ation Results	73
		5.6.1	Impact of SNR and Number of NLoS Paths	74
		5.6.2	Impact of the propagation fading factor n and Number of NLoS Paths	75
		5.6.3	Impact of the shape parameter m and Number of NLoS Paths	76
		5.6.4	Impart of number of NLoS and the mismatched shape parameter m	76
		5.6.5	Simulation Conclusions	78

	5.7	Concl	usions	78
6	Mu	ltipath	Component Power Delay Profile Based Sensing	7 9
	6.1	_	uction	79
	6.2	Doubl	y Fractional System Model	80
		6.2.1	Transmitter Structures	80
		6.2.2	Time-Domain Equivalent Channel Representation After CP Removal	80
	6.3	MPCI	PDP-Based Sensing Problem Formulation	82
		6.3.1	Delay dictionary construction	83
		6.3.2	MPCPDP-based Ranging and Doppler Shift Estimation	85
	6.4	Expec	tation Maximization (EM) - Expectation Consistant (EC) Algorithm	85
		6.4.1	Review of Expectation Maximization	85
		6.4.2	Expectation Consistent Approach	87
		6.4.3	Estimate LoS range d_0 and related velocity $v\cos(\theta_1)$ in LoS direction	90
		6.4.4	MPCPDP-based Sensing Algorithm	91
	6.5	Theor	etical Performance for the MPCPDP-based Sensing Method	91
	6.6	Simula	ation Results	93
		6.6.1	Impact of SNR	94
		6.6.2	Impact of the Nakagami- m Shape Parameter	94
		6.6.3	Impact of Absolute Velocity (v)	97
		6.6.4	Simulation Conclusions	98
	6.7	Concl	usions	100
7	Cor	clusio	n and Future Work	.01
\mathbf{A}			1	.03
	A.1	Deriva	ation of Nakagami-m Posterior Mean and Variance	103
	A.2	List of	f Publications	105

Résumé

Cette thèse étudie de manière systématique des techniques de mesure de distance et d'estimation de paramètres à haute précision dans des environnements radio riches en trajets multiples, avec un accent sur la détection et la communication intégrées (ISAC) pour les futurs réseaux 6G. Motivé par la demande croissante de connectivité ubiquitaire et de perception fine de l'environnement, ce travail exploite le profil de retard de puissance (PDP) extrait des informations d'état du canal (CSI) afin de relever les défis liés à la multipathie, à la bande passante limitée et aux contraintes matérielles.

La recherche débute par une analyse approfondie de l'estimation du PDP et de la récupération parcimonieuse, et propose un nouveau cadre d'estimation du PDP à haute résolution. En s'appuyant sur l'apprentissage bayésien parcimonieux et des techniques « off-grid », l'approche proposée améliore significativement la discrimination des retards et la séparation des trajets, permettant une précision métrique de la mesure de distance dans des environnements denses en trajets multiples. Cela établit une base théorique pour une estimation robuste de la distance à partir d'ondes OFDM (Orthogonal Frequency Division Multiplexing) standards, largement utilisées dans les systèmes sans fil modernes.

Sur cette base, la thèse développe un cadre de détection OFDM en domaine temporel pour des scénarios à délai et Doppler doublement fractionnaires. Une grille de retards suréchantillonnée est construite pour représenter les retards fractionnaires, et les amplitudes multi-trajets sont modélisées par une enveloppe de Nakagami-m avec phase uniformément distribuée. Un algorithme EM–EC (Expectation–Maximization / Expectation Consistent) efficace est introduit pour estimer conjointement les hyperparamètres d'atténuation de grande échelle, reconstruire la structure parcimonieuse des composantes multi-trajets (MPC) en séparant LoS/NLoS, et extraire la distance et le Doppler de la trajectoire LoS. Le cadre s'appuie sur une linéarisation Doppler du premier ordre et inclut une caractérisation des points fixes clarifiant le comportement de convergence ; une borne "Genie" est utilisée pour étalonner les performances atteignables en simulation.

De vastes simulations numériques évaluent la performance du cadre de récupération parcimonieuse basé sur le PDP, des méthodes de mesure de distance basées sur l'OFDM et de l'algorithme OFDM temporel d'estimation conjointe délai—Doppler. Les résultats montrent des améliorations sensibles par rapport aux méthodes existantes en termes de résolution de retard, de précision de mesure de distance et de robustesse en mobilité, soulignant l'intérêt de combiner récupération parcimonieuse et modélisation statistique rigoureuse pour l'ISAC.

Les contributions de cette thèse fournissent à la fois un cadre théorique et des solutions algorithmiques pratiques pour une détection de haute précision dans les futurs systèmes ISAC. Plusieurs pistes de recherche demeurent ouvertes : (i) validation expérimentale en conditions réelles afin de confirmer la faisabilité face aux imperfections matérielles et à la dynamique des environnements ; (ii) extension de l'unidimensionnel à la localisation et au suivi complets, condition clé pour une position robuste dans des scénarios

complexes ; (iii) étude des limites théoriques de performance en l'absence de bornes de Cramér–Rao (CRB) directement calculables, afin de quantifier la précision fondamentale des algorithmes développés ; (iv) raffinement du modèle Doppler au-delà de la linéarisation du premier ordre (p. ex., expansions d'ordre supérieur ou schémas de compensation de biais) et mise à l'épreuve de la robustesse face à des perturbations non gaussiennes pour renforcer encore la précision en conditions de propagation réalistes.

Abstract

This dissertation systematically investigates high-precision ranging and parameter estimation techniques in multipath-rich wireless environments, with an emphasis on integrated sensing and communication (ISAC) for future 6G networks. Motivated by the increasing demands for ubiquitous connectivity and accurate environmental awareness, this work focuses on exploiting the Power Delay Profile (PDP) extracted from Channel State Information (CSI) to address the challenges of multipath propagation, limited bandwidth, and hardware constraints.

The research begins with an in-depth analysis of PDP estimation and sparse signal recovery, proposing a novel high-resolution PDP estimation framework. By leveraging sparse Bayesian learning and off-grid modeling techniques, the proposed approach significantly improves delay discrimination and path separation capabilities, enabling meter-level ranging accuracy in dense multipath environments. This sets the theoretical foundation for robust distance estimation based on standard OFDM (Orthogonal Frequency Division Multiplexing) waveforms, which are widely adopted in modern wireless systems.

Building upon this foundation, the dissertation develops a time-domain OFDM sensing framework for doubly fractional delay–Doppler scenarios. An oversampled delay grid is constructed to represent fractional delays, and multipath amplitudes are modeled with a Nakagami-m envelope and uniformly distributed phase. A computationally efficient EM–EC algorithm is introduced to jointly estimate large-scale fading hyperparameters, recover the sparse MPC structure (separating LoS/NLoS), and extract the LoS range and Doppler. The framework employs a first-order Doppler linearization and includes a fixed-point characterization that clarifies convergence behavior; a Genie Bound is used to benchmark achievable performance in simulations.

Extensive numerical simulations are conducted to evaluate the performance of the proposed PDP-based sparse recovery framework, the OFDM-based ranging methods, and the time-domain OFDM joint delay—Doppler estimation algorithm. Results demonstrate significant improvements over existing methods in terms of delay resolution, ranging accuracy, and robustness to mobility, highlighting the advantages of integrating sparse signal recovery techniques with principled statistical modeling for ISAC.

The contributions of this dissertation provide not only a theoretical framework but also practical algorithmic solutions for high-precision sensing in future ISAC systems. Looking forward, several research directions remain to be explored. First, real-world implementation and validation are necessary to confirm the proposed methods' feasibility under hardware impairments and environmental dynamics. Second, extending the framework from one-dimensional ranging to full localization and tracking will be crucial for enabling robust positioning in complex scenarios. Third, investigating theoretical performance limits in the absence of directly computable Cramér—Rao Bounds (CRBs) will help quantify the fundamental accuracy of the developed algorithms. Finally, refining the Doppler modeling beyond first-order linearization (e.g., higher-order expansions or bias-

compensation schemes) and stress-testing robustness under non-Gaussian disturbances will further enhance estimation precision in realistic propagation conditions.

Acknowledgement

At this moment, I would like to draw a conclusion to my seven-year journey in France. Looking back, I am deeply aware that without the help and support of many people, it would have been impossible for me to complete my doctoral studies.

First and foremost, I would like to express my heartfelt gratitude to my PhD advisor, Prof. Dirk Slock. Without his insightful guidance, I could hardly imagine completing my doctoral research within three years and successfully defending my thesis. In times when I felt inadequate and often doubted my own ability, his patience and wisdom provided me with the strongest support. He was always able to give me clear directions when I was confused, while at the same time granting me the freedom to pursue my own research interests. This trust and encouragement allowed me to gradually develop independent thinking, which has become one of the most valuable assets of my academic journey. It is also a truly remarkable coincidence that Prof. Slock is the doctoral advisor of Prof. Luc Deneire. It was Prof. Deneire who first offered me an engineering opportunity when I was at Xidian University, which opened the door for me to come to France. Now he is again part of my thesis defense committee, marking the conclusion of this journey. This remarkable connection makes me feel that the world is indeed very small.

I am also very grateful to Prof. Vicente Zarzoso, whose guidance at the I3S laboratory sparked my strong interest in signal processing and estimation theory, which later became the core of my PhD research. I would also like to sincerely thank my thesis reviewers and the members of my defense committee. In particular, I am indebted to Prof. Benoît Denis for carefully reviewing my dissertation and providing many valuable comments. I also wish to thank Prof. Christoph Mecklenbräuker, Prof. Jérôme Härri, Prof. Laura Cottatellucci, and the other committee members for their time, support, and constructive feedback. Beyond academic work, many friends have accompanied me along this journey: Zilu Zhao, Jichao Chen, Zunqi Li, Hongwei Hou, and others, who have always been there to help me through difficulties and confusion.

Finally, I would like to express my deepest gratitude to my wife, Shuyuan Luo. Without her understanding and companionship, it would have been extremely difficult for me, with my tendency to procrastinate, to complete my PhD within three years. One of my strongest motivations to graduate early was the hope of reuniting with her as soon as possible.

In closing, this acknowledgment not only marks the end of my student journey, but also the beginning of a new chapter. Although I have often felt that I am far from gifted, the fact that I persevered through this path and ultimately obtained a doctoral degree remains one of the most precious miracles of my life.

List of Symbols

Symbol	mbol Description	
\overline{a}	Scalar a	
a	Vector a	
\mathbf{A}	Matrix A	
$(\cdot)^*$	Conjugate of a vector or matrix	
$(\cdot)^T$	Transpose of a vector or matrix	
$(\cdot)^H$	Hermitian (conjugate transpose) of a vector or matrix	
$(\cdot)^{\dagger}$	Moore-Penrose pseudo-inverse of a vector or matrix	
\otimes	Kronecker product	
\odot	Hadamard product	
$ \mathbf{a} $	Absolute value of scalar \mathbf{a}	
$ \mathbf{A} $	Determinant of matrix A	
\mathbf{A}^{-1}	Inverse of matrix \mathbf{A}	
$\ \mathbf{a}\ _p$	ℓ_p norm of vector ${\bf a}$	
$\ \mathbf{A}\ _F$	Frobenius norm of matrix \mathbf{A}	
$\mathrm{vec}(\mathbf{A})$	Vectorization of matrix \mathbf{A}	
$\mathbf{a}_{\backslash i}$	Vector \mathbf{a} with the i -th element removed	
$\operatorname{diag}(\mathbf{a})$	Diagonal matrix with vector a as its main diagonal	
\mathbf{I}_N	$N \times N$ Identity matrix	
0	Zero vector or zero matrix	
1	All-ones vector or matrix	
\mathbb{R}	Real number field	
\mathbb{C}	Complex number field	
$\operatorname{Re}\{\cdot\}$	Real part of a complex variable	
$\operatorname{Im}\{\cdot\}$	Imaginary part of a complex variable	
$\max(\cdot)$	Maximum of a set of elements	
$\min(\cdot)$	Minimum of a set of elements	
[.]	Floor function	
∝ 0	Proportional to	
∂	Partial derivative	
$\delta(\cdot)$	Dirac delta function	
$\delta[\cdot]$	Kronecker delta function	
$\ln(\cdot)$	Natural logarithm	
$\exp(\cdot)$	Exponential function	
$\mathbb{E}[\cdot]$	Expectation of a random variable	
$\operatorname{Var}[\cdot]$	Variance of a random variable	
$\mathcal{N}(\mu, au)$	Gaussian pdf with mean μ and variance τ	

List of Abbreviations

Abbreviation	Full Name
3GPP	3rd Generation Partnership Project
5G	5th Generation
5G-A	5G-Advanced
6G	6th Generation
ADMM	Alternating Direction Method of Multipliers
AI	Artificial Intelligence
AFDM	Affine Frequency Division Multiplexing
AMP	Approximate Message Passing
AoA	Angle of Arrival
B5G	Beyond 5G
BP	Belief Propagation
CSI	Channel State Information
CRB	Cramér-Rao Bound
CP	Cyclic Prefix
eMBB	Enhanced Mobile Broadband
EM	Expectation Maximization
EC	Expectation Consistent
EP	Expectation Propagation
FDD	Frequency Division Duplexing
FFT	Fast Fourier Transform
Gbps	gigabit-per-second
i.i.d.	Independent and Identically Distributed
IMT	International Mobile Telecommunications
IoT	Internet of Things
ITU	International Telecommunication Union
LoS	Line of Sight
LASSO	Least Absolute Shrinkage and Selection Operator
LS	Least Squares
MIMO	Multiple Input Multiple Output
MPC	Multipath Component
NLoS	Non-Line of Sight
OFDM	Orthogonal Frequency Division Multiplexing
OMP	Orthogonal Matching Pursuit
PDP	Power Delay Profile
PDF	Probability Density Function
ReVAMP	Reweighted Vector AMP
RMSE	Root Mean Square Error

SBL Sparse Bayesian Learning	
SNR Signal-to-Noise Ratio	
URLLC Ultra-Reliable Low-Latency Communications	
VAMP Vector Approximate Message Passing	

List of Figures

2.1 2.2	Comparision under different SNR with $n = 2$	35 35
4.1 4.2	Reconstructed delay impulses for different SNRs in a single MC realization. RMSE of estimated delays versus SNR, averaged over 10^4 MC realizations. The second-order Taylor refinement method achieves the best performance	59
	across all SNRs	60
5.1 5.2	Factor graph of ReVAMP	67 74
5.3	m=1	74 75
5.4	The impact of the environment propagation fading factor n and the number of NLoS paths on d_0 estimation with $m=1$	75
5.5	The impact of the environment propagation fading factor n and the number of NLoS paths on d_0 estimation with $m = 5 \dots \dots \dots \dots$.	76
5.6	The impact of the Nakagami-m distribution's shape parameter m and the number of NLoS paths on d_0 estimation with $n=3$	77
5.7	The impact of the mismatched Nakagami-m distribution's shape parameter m and the number of NLoS paths on d_0 estimation with true $m=5$	77
6.1	m=1: RMSE of Range Estimation vs. SNR for Different Numbers of Paths and Methods	95
6.2	m=5: RMSE of Range Estimation vs. SNR for Different Numbers of Paths and Methods	95
6.3	m=1: NRMSE of LoS Doppler Shift Estimation vs. SNR for Different Numbers of Paths	96
6.4	m=5: NRMSE of LoS Doppler Shift Estimation vs. SNR for Different Numbers of Paths	96
6.5	RMSE of Range Estimation Across Different Number of Paths and Methods vs. m	97
6.6	NRMSE of LoS Doppler Shift Estimation Across Different Number of Paths of Paths vs. m	98
6.7 6.8	RMSE of Range Estimation Across Different Number of Paths vs. Velocity v NRMSE of LoS Doppler Shift Estimation Across Different Number of Paths	99
	vs. Velocity v	99

List of Tables

2.1	Parameters setting for CRB Comparisons	34
3.1	Comparison of Sparse Estimation Algorithms (No Prior on $\mathbf{x})$	43
4.1	Fractional Delay Recovery Simulation Parameters	57
5.1	Parameters setting for MPCPDP-Based Ranging	74
6.1	Parameters setting for MPCPDP-based Sensing	93

Chapter 1

Introduction

1.1 Background and Motivation

Since the 1980s, modern mobile communication systems have undergone generational upgrades approximately every decade [1]. Propelled by continuous technological advancements, mobile communications have become deeply integrated into nearly every aspect of human life [2]. This integration has not only transformed how people live and work but has also driven global industrial optimization and high-quality economic development. In recent years, the proliferation of mobile internet and the rapid adoption of the Internet of Things (IoT) have triggered an exponential increase in the number of wireless terminals and the volume of data traffic [3]. To meet the growing demands for massive connectivity and high-throughput communication, the fifth generation (5G) of mobile communication technology has emerged [4].

The International Telecommunication Union (ITU) has identified three primary use cases for 5G: enhanced Mobile Broadband (eMBB), massive Machine-Type Communications (mMTC), and ultra-Reliable Low-Latency Communications (URLLC) [5]. These pillars support the growth of services such as high-definition video streaming, the IoT, smart manufacturing, and autonomous driving. By the end of 2024, global 5G subscriptions surpassed 2 billion [6], with projections indicating that 5G connections will exceed 4G by 2028 [7]. Furthermore, 5G is expected to contribute nearly USD 1 trillion to the global economy by 2030 [8], with a user coverage rate reaching 64% and mobile internet penetration approaching 5.5 billion people. Alongside the commercial deployment of 5G, major countries and regions worldwide have launched research initiatives for beyond 5G (B5G) and the sixth generation (6G) of mobile communication technologies.

Europe, in particular, has demonstrated strong strategic foresight and technological leadership in 6G research. In March 2019, the University of Oulu in Finland hosted the world's first 6G Wireless Summit, releasing the inaugural global 6G white paper [9]. In 2021, the European Union launched the Hexa-X project, led by Nokia, marking the world's first comprehensive 6G research initiative [10]. This flagship project, now in its second phase—Hexa-X-II—focuses on developing 6G network architectures, key enabling technologies, and sustainable development strategies, playing a central role in shaping international standards [11].

Beyond Europe's leadership, the ITU officially launched research efforts for the next-generation International Mobile Telecommunications (IMT) systems in 2020, consolidating a global consensus on the vision and direction of 6G [12]. Meanwhile, the United States established the Next G Alliance, and countries such as Japan, South Korea, and China

have introduced national-level strategies. In particular, China formed the IMT-2030 (6G) Promotion Group in 2019, actively participating in international standardization and technical trials [13]. Nonetheless, in policy coordination, technological integration, and cross-industry collaboration, Europe has secured a leading position in 6G, underpinned by its strengths in fundamental research, sustainable strategies, and artificial intelligence integration.

The 3rd Generation Partnership Project (3GPP) is currently finalizing Release 18, set for completion in 2024, marking the transition to 5G-Advanced (5G-A) [14]. As a crucial phase bridging 5G and 6G, 5G-A aims to enhance the performance and capabilities of all three 5G use cases. In June 2023, the ITU released its "Framework and Overall Objectives of the Future Development of IMT for 2030 and Beyond," which outlines the overarching goals and capability requirements of 6G systems [12].

Looking ahead to 2030 and beyond, 6G will address increasingly diverse and complex service needs. Building upon the foundational 5G use cases, 6G is poised to expand in three key directions: immersive communication, ultra-massive connectivity, and extremely reliable low-latency communication [15, 16]. Immersive communication includes applications like extended reality (XR), holographic interaction, and sensory connectivity, all of which demand significant improvements in transmission rates, spectral efficiency, and system capacity [16, 17]. Ultra-massive connectivity will extend mMTC to domains such as industrial automation, intelligent transportation, and digital twins, supporting hundreds of millions of devices [18]. More stringent URLLC capabilities will be crucial for mission-critical applications like remote surgery, autonomous driving, and smart manufacturing [19].

Simultaneously, 6G is expected to integrate transformative capabilities such as ubiquitous connectivity, integrated sensing and communication (ISAC), and deep fusion with artificial intelligence [20]. Ubiquitous connectivity will rely on the convergence of terrestrial and non-terrestrial networks—including satellites and unmanned aerial vehicles—forming a comprehensive, three-dimensional infrastructure [16]. The convergence of communication and sensing will enable high-resolution applications like environmental awareness and centimeter-level positioning [17]. Crucially, 6G will feature native integration of artificial intelligence, leveraging edge intelligence, deep learning, and large-scale data mining to enable autonomous network decisions and collaborative optimization [17, 20]. In this context, the European Hexa-X initiative has explicitly identified "AI-native design" and "sustainability" as foundational principles of 6G architecture [17].

To meet these demands, 6G is expected to achieve significant improvements across nine key performance indicators, building upon the 5G foundation. Peak data rates will reach the terabit-per-second (Tbps) scale, while user-experienced data rates will rise to gigabit-per-second (Gbps) levels [21]. Spectral efficiency will increase by a factor of 1.5 to 3, and device connectivity density will exceed ten million devices per square kilometer. Mobility support will extend to scenarios approaching 1000 km/h, with over-the-air latency reduced to sub-millisecond levels. Furthermore, 6G will support centimeter-level positioning and incorporate green, low-carbon system designs. The European Union has launched initiatives such as Green6G [22] and RISE-6G [23] to advance these efforts.

ISAC technology unifies wireless communication and environmental sensing within a single architecture [24]. By reusing communication signals for high-resolution sensing, ISAC significantly improves spectral and energy efficiency. It enables accurate extraction of parameters like object position, velocity, size, and material properties—vital in high-mobility, high-density environments [25]. ISAC also enhances intelligent tasks such

as resource scheduling and beamforming, creating a cognitive wireless environment that supports applications like autonomous driving, smart manufacturing, and digital twins [26].

However, ISAC systems face significant technical challenges, particularly in achieving high-precision localization and sensing in environments with severe multipath propagation and low SNR [20, 27]. Constructing accurate environment models aided by communication signals remains a research frontier. Channel State Information (CSI) contains rich spatial, temporal, and frequency-domain features, making it a crucial passive sensing source [28].

Positioning methods based on the Power Delay Profile (PDP), a key technique within CSI-based sensing, have attracted significant attention for their advantages in multipath separation and path energy modeling [29, 30]. PDP-based techniques, particularly when combined with high-bandwidth MIMO systems and large-scale antenna arrays, enable precise estimation of propagation paths, facilitating centimeter-level localization in ISAC applications.

Nonetheless, PDP-CSI-based localization faces challenges in complex environments, where severe overlap among multipath components reduces accuracy. Frequency-selective fading and temporal variations further complicate PDP estimation, demanding robust system configurations and algorithms [31]. Moreover, the increased dimensionality of modern wireless channels imposes significant computational burdens, limiting real-time performance. These limitations highlight the urgent need for high-resolution, low-complexity, and interference-resilient PDP extraction and target identification algorithms.

In response to these challenges, this dissertation focuses on leveraging the PDP derived from CSI to infer target distance and motion characteristics in multipath-rich environments. The main contributions are: (1) a high-resolution PDP estimation method incorporating sparse signal recovery and off-grid modeling [32]; (2) a statistical mapping between PDP energy and physical distance, enabling joint communication-sensing distance estimation without additional overhead; and (3) a Doppler-delay joint estimation algorithm under Affine Frequency Division Multiplexing (AFDM), which demonstrates strong robustness in high-mobility scenarios [33].

1.2 Related Works

1.2.1 Channel State Information Based Sensing

Accurate distance estimation is a fundamental aspect of wireless localization systems, especially in diverse propagation environments. Various positioning techniques have been developed to address this challenge, each with unique principles, advantages, and limitations. This section provides a concise yet comprehensive review of these techniques, focusing on their methodologies and key contributions.

Time-based ranging techniques, such as Time-of-Arrival (ToA) and Time-Difference-of-Arrival (TDoA), infer distance by measuring signal propagation delays. ToA estimates absolute travel time to determine range, while TDoA calculates relative delays between receivers, reducing transmitter synchronization requirements.

These methods offer high accuracy in line-of-sight (LOS) scenarios. For instance, [34] demonstrated the scalability and energy efficiency of TDoA in real-time location systems. [35] analyzed the theoretical accuracy limits of ToA-based ranging in UWB systems, accounting for clock drift. To address multipath challenges, [36] proposed a multipath-assisted maximum likelihood estimator that exploits early multipath components to im-

prove indoor positioning robustness. Comprehensive UWB TDoA datasets introduced by [37] have further facilitated algorithm development. Additionally, [38] compared TDoA with Two-Way Ranging (TWR), highlighting trade-offs in complexity and synchronization requirements.

However, time-based techniques face performance degradation in non-line-of-sight (NLOS) conditions and rely heavily on precise time synchronization, limiting their practicality in dynamic environments.

Angle-of-Arrival (AoA) techniques estimate the direction of incoming signals using antenna arrays. By exploiting spatial diversity, AoA can complement or substitute time-based methods, particularly in multipath-rich indoor environments.

AoA-based methods are typically low-cost and achieve high accuracy when sufficient spatial diversity exists. [39] tackled the nonlinear challenges in indoor AoA positioning by introducing a multi-anchor approach with outlier rejection. [40] provided an overview of AoA principles in wireless sensor networks, emphasizing their simplicity and effectiveness. The potential of Bluetooth 5.1 AoA for indoor applications was explored by [41] and further detailed by [42], while [43] compared AoA with Bluetooth channel sounding, discussing their complementary advantages.

Nevertheless, AoA methods require complex antenna array calibration and may struggle in environments with severe reflections and limited angular resolution.

Received Signal Strength Indicator (RSSI)-based methods estimate distance by mapping received signal power to range, typically through empirical path loss models. While inherently coarse-grained, RSSI-based ranging remains appealing for resource-constrained and cost-sensitive scenarios.

[44] proposed the RADAR system, an early RSSI-based framework integrating empirical fingerprinting for improved robustness. [45] explored relative location estimation in wireless sensor networks, addressing challenges of environmental variability. Bluetooth RSSI's role in indoor positioning was examined by [46], while [47] investigated RSSI triangulation with multiple gateways, highlighting limitations due to environmental dynamics. To mitigate these issues, [48] combined RSSI with non-ranging techniques in the RSSI-APIT algorithm to enhance indoor accuracy.

Despite these advances, RSSI-based approaches are susceptible to multipath fading, shadowing, and environmental changes, typically achieving only meter-level accuracy in cluttered indoor environments.

Multipath components (MPCs), once considered a source of error, are now increasingly exploited as valuable geometric information for positioning. By leveraging MPCs, systems can achieve robust localization even in challenging NLOS environments.

[49] analyzed the impact of multipath on ranging and introduced a multipath-mitigating maximum likelihood estimator for UWB signals. Building on this, [50] proposed a machine learning approach to mitigate multipath effects and LOS obstructions in UWB localization. Recent works, including [51, 52, 53], have further advanced MPC-based positioning. Notably, [52, 53] developed graph-based Bayesian frameworks capable of reconstructing LOS paths in fully obstructed scenarios by jointly estimating MPC parameters—eliminating the need for prior radio parameter knowledge.

Additionally, mirror-source modeling has been explored to directly exploit MPCs. [54] quantified the positioning information content of MPCs, while [55] integrated SLAM with MPC exploitation for improved robustness. [56, 57] extended these concepts with belief propagation and SLAM algorithms to jointly estimate user positions and virtual anchors. Most recently, [58] demonstrated the applicability of MPC-based methods in 5G

millimeter-wave vehicular networks.

These studies collectively highlight that MPCs, rather than a hindrance, can be harnessed to achieve robust and precise positioning. However, MPC-based methods typically require sophisticated signal processing and precise modeling, adding complexity to real-world deployment.

In summary, each positioning technique offers unique strengths and faces inherent limitations. Time-based methods excel in LOS scenarios but depend on precise synchronization and degrade in NLOS environments. AoA approaches are cost-effective and accurate in spatially diverse settings but require complex antenna arrays and are sensitive to reflections. RSSI-based methods are simple and resource-efficient, though they offer lower accuracy and are susceptible to environmental changes. Finally, MPC-based techniques provide robust positioning in obstructed environments by leveraging multipath, albeit with increased algorithmic complexity. These trade-offs underscore the need for adaptive hybrid approaches or new paradigms like Integrated Sensing and Communication (ISAC) to overcome existing limitations and meet the demands of next-generation wireless systems.

1.2.2 Sparse Signal Recovery

Sparse signal recovery (SSR) is fundamental in compressed sensing (CS), enabling the reconstruction of signals from underdetermined linear measurements by exploiting the inherent sparsity of many real-world signals. Over the years, a variety of methods have been developed, each offering distinct advantages and facing inherent limitations.

Early SSR methods rely on convex relaxation and greedy algorithms. Basis Pursuit (BP) [59] reformulates the recovery problem as an ℓ_1 -minimization task, offering theoretical guarantees under specific measurement conditions. Orthogonal Matching Pursuit (OMP) [60] and iterative re-weighted ℓ_1/ℓ_2 minimization techniques [61] provide computationally efficient alternatives. However, these methods are typically sensitive to noise, require restrictive measurement conditions, and can struggle with highly sparse signals.

Bayesian frameworks emerged to address these challenges by incorporating measurement noise and prior sparsity knowledge. Sparse Bayesian Learning (SBL) [62], rooted in the Relevance Vector Machine (RVM) [63], uses hierarchical Gaussian scale mixtures as priors to automatically induce sparsity and achieve higher recovery accuracy [64]. Bayesian LASSO [65] further extended these ideas by introducing Laplace priors, allowing for flexible sparsity control. While Bayesian methods improve accuracy and robustness, they are generally more computationally demanding and require careful prior selection.

Empirical Bayes (EB) approaches stand out by estimating hyperparameters directly from the data, reducing reliance on explicit prior knowledge. The Fast Marginalized ML (FMML) algorithm [66] exemplifies this by combining EB estimation with efficient greedy initialization to improve convergence. In parallel, Approximate Message Passing (AMP) [67] and its variants, including Generalized AMP (GAMP) [68, 69, 70] and Vector AMP (VAMP), exploit central limit theorem-based approximations to achieve low-complexity, Bayes-optimal recovery in large random matrix scenarios [71, 72]. While these methods excel in large-scale systems, their performance can degrade in structured or non-random measurement settings.

Variational Bayesian inference [73] and belief propagation (BP) techniques [74] offer scalable alternatives to exact Bayesian inference by employing mean-field (MF) approximations to enhance computational efficiency [75]. Non-parametric methods such as NOPE [76] provide robust recovery by adapting to unknown signal and noise statistics. Covariance-fitting approaches like SPICE [77] jointly estimate hyperparameters and sparse coefficients, aiming to minimize fitting errors. These methods provide scalability and adaptability, though they may have lower accuracy compared to exact Bayesian approaches and require careful convergence handling.

At the core of many SSR advances lies Empirical Bayes learning guided by Stein's Unbiased Risk Estimator (SURE) [78, 79, 80], which directly targets the minimum mean squared error (MSE) in recovery. These principles have been extended to kernel-based system identification [81, 82], hyperparameter selection [83], posterior variance prediction [84], and generalized SURE for exponential family models [85]. Adaptive algorithms with component-wise updates [86] have emerged from SURE-driven optimization, enhancing robustness even in challenging scenarios. However, these methods require careful implementation to balance computational cost with performance improvements.

In summary, convex and greedy methods offer simplicity and computational efficiency, though they are limited by noise sensitivity and strict measurement requirements. Bayesian frameworks provide superior accuracy and robustness but at higher computational cost. Empirical Bayes and message passing methods excel in large-scale systems, while variational and non-parametric approaches offer scalable, adaptable solutions. SURE-driven techniques unify these efforts, directly optimizing recovery error and supporting robust and adaptive SSR. Together, these advances have established a solid foundation for SSR in modern wireless communications, sensing, and signal processing.

1.2.3 Statistical Inference

Statistical inference forms a crucial foundation for parameter estimation and latent variable modeling, particularly within probabilistic frameworks. A cornerstone in this domain is the Expectation-Maximization (EM) algorithm [87], which has been widely used for maximum likelihood estimation in models involving hidden variables. However, the E-step of EM often becomes computationally intractable, especially when dealing with high-dimensional or complex posterior distributions. To address this challenge, a variety of approximate inference techniques have been developed.

Early approaches focused on sampling-based and deterministic variational methods [88], providing approximate solutions that balance accuracy with computational efficiency. More recently, Approximate Message Passing (AMP) algorithms [89, 90, 91] have emerged as powerful tools for scalable variational inference, particularly under large-scale random matrix models. AMP offers precise state evolution characterizations in ideal conditions [92], enabling efficient posterior approximations. Nonetheless, its convergence deteriorates in ill-conditioned or structured measurement scenarios [93, 94].

To enhance robustness, the Vector AMP (VAMP) framework [70] was introduced, leveraging a dual-variable splitting strategy to improve convergence for right-rotationally invariant matrices. Extensions such as EM-VAMP [95] have demonstrated effectiveness in high-dimensional Bayesian learning problems, offering flexible and accurate inference capabilities.

Beyond AMP and VAMP, variational and message-passing frameworks have also been explored in diverse applications. For instance, cooperative localization [96], compressive video sampling [97], and approximate Bayesian computation [98] have benefited from approximate Bayesian inference methods. In addition, non-parametric variational Bayesian approaches [99] have demonstrated flexibility in handling unknown noise models and com-

plex priors, broadening the applicability of variational techniques.

Expectation Consistent (EC) inference [100, 101] represents another promising approach to approximating complex posterior distributions, especially when AMP-based methods are less effective. EC achieves posterior approximations via moment-matching with exponential family distributions and offers a variational energy interpretation [102]. However, convergence can remain a challenge with standard single-loop EC algorithms, leading to the development of double-loop EC methods that provide guaranteed convergence [100].

Taken together, these algorithmic advances significantly enrich the toolbox of statistical inference, offering practical approximations in settings where exact posterior computations are infeasible. As modern applications increasingly demand sophisticated inference in high-dimensional, noisy, and structured environments, these developments continue to bridge the gap between theoretical models and practical implementations.

1.3 Main Contributions and Structure

This dissertation investigates the use of Power Delay Profile (PDP)-based localization in multipath-rich environments, emphasizing Bayesian inference frameworks that exploit underlying sparsity and physical propagation models. The main contributions of this work can be summarized as follows.

First, we derive the fundamental performance limits for RSSI- and PDP-based ranging methods by conducting a rigorous Cramér–Rao Bound (CRB) analysis. This theoretical foundation highlights the advantages of PDP-based techniques in challenging propagation scenarios. Second, we propose a high-resolution PDP estimation framework that integrates sparse signal recovery, off-grid modeling, and empirical Bayesian learning, achieving super-resolved delay estimation even in the presence of dense multipath components. Third, we develop a time-domain OFDM sensing framework for doubly fractional delay—Doppler scenarios. By constructing an oversampled delay grid and modeling multipath amplitudes with a Nakagami-m envelope and uniform phase, we propose an EM–EC algorithm that jointly estimates large-scale fading hyperparameters, recovers the sparse MPC structure (separating LoS/NLoS), and extracts LoS Doppler and range for ISAC.

The remainder of this dissertation is organized as follows. Chapter 2 establishes the theoretical performance limits of RSSI- and PDP-based ranging by deriving and comparing the CRBs. It clarifies the conditions under which PDP-based approaches outperform traditional RSSI-based methods. Chapter 3 introduces key tools from sparse signal recovery and Bayesian inference, reviewing classical and modern approaches for solving underdetermined systems and highlighting their relevance for multipath delay estimation tasks. Chapter 4 focuses on precise delay estimation under fractional delay scenarios, presenting an oversampled parametric dictionary framework and novel algorithms that refine delay estimates through iterative, off-grid sparse Bayesian learning techniques. Chapter 5 develops a multipath component power delay profile (MPCPDP)-based ranging approach, proposing the EM-ReVAMP algorithm to tackle challenges in parameter estimation under Nakagami-m fading, and validates its robustness through extensive simulations. Chapter 6 extends the PDP-based framework to joint delay-Doppler sensing under a time-domain OFDM model with doubly fractional delays and Doppler shifts. It introduces an oversampled delay grid under Nakagami-m fading, and develops an EM-EC algorithm for joint hyperparameter estimation, sparse delay–Doppler recovery, and LoS range/Doppler extraction. Finally, Chapter 7 concludes the dissertation by summarizing the key findings, discussing practical implications, and outlining potential future research directions in PDP-based sensing and positioning.

Furthermore, several key contributions of this dissertation have been published in leading international journals and conferences. These publications are detailed in the appendix A.2.

Chapter 2

Fundamental Limits of RSS and PDP-Based Ranging: A Cramér–Rao Bound Perspective

2.1 Introduction

Accurate distance estimation, known as ranging, is crucial for many wireless localization tasks. In emerging fifth-generation (5G) and beyond 5G (B5G) systems, ranging is increasingly integrated into communication frameworks for applications such as location-aware services, intelligent transportation, emergency response, and physical-layer sensing [103]. While systems like GPS rely on global infrastructure, they often fail indoors or in dense urban environments, making alternative ranging methods essential.

Traditionally, the Received Signal Strength Indicator (RSSI) has been popular for ranging due to its simplicity and low hardware demands. However, RSSI suffers from limited resolution and poor robustness in multipath fading environments. To achieve more accurate ranging, time-based methods such as Time-of-Arrival (ToA) and Round-Trip-Time (RTT) have been employed. Yet these methods demand precise synchronization or high time resolution, which is challenging in bandwidth-constrained or cost-sensitive scenarios.

Recent advancements in Orthogonal Frequency Division Multiplexing (OFDM) and fine-grained channel estimation (e.g., Channel State Information, CSI) have enabled access to richer representations of the radio channel, such as the Power Delay Profile (PDP). The PDP captures the delay and amplitude of individual multipath components and is particularly promising in multipath-rich indoor settings. This raises a key question: can we improve ranging accuracy by leveraging the multipath structure in the PDP, rather than collapsing it as in RSSI-based approaches?

This chapter investigates the theoretical performance limits of PDP-based and RSSI-based ranging using Cramér–Rao Bound (CRB) analysis. Unlike heuristic or model-fitting techniques, the CRB provides a fundamental lower bound on the variance of any unbiased propagation distance estimator. With this approach, we address the following research questions:

• What are the inherent limitations of RSSI-based ranging under a physically grounded multipath propagation model?

- Can detailed multipath information in the PDP be exploited to enhance ranging accuracy?
- How do statistical modeling assumptions about multipath fading (e.g., Rayleigh fading, distance-dependent path gain) impact the CRB?
- Under what conditions does PDP-based ranging outperform RSSI-based methods?

To explore these questions, we develop a unified OFDM-based signal model that includes both RSSI and PDP representations of the channel. Within this framework, we derive the CRB for PDP-based ranging using joint parameter estimation and marginalized estimation approaches. We then compare these bounds to the CRB for RSSI-based ranging under the same statistical assumptions and validate the results through simulations.

The remainder of this chapter is organized as follows. Section 2.2 reviews classical time-based and RSSI-based ranging approaches and motivates the use of PDP. Section 2.3 details the system model and key assumptions. Section 2.4 derives the CRBs for both methods. Section 2.5 presents simulation results and concludes the analysis.

2.2 Conventional Ranging Approaches and the Case for PDP

2.2.1 Time-Based Ranging Methods

Before discussing signal-strength or multipath-aware techniques, it is important to review the traditional category of time-based ranging methods. These methods estimate distance by measuring signal propagation delays, and include:

Time of Arrival (ToA)

To A estimates distance by measuring the absolute time a signal takes to travel from transmitter to receiver:

$$d = c \cdot (t_{\rm rx} - t_{\rm tx}),\tag{2.1}$$

where c is the speed of light, and $t_{\rm tx}, t_{\rm rx}$ denote the transmission and reception times.

Limitation: To A requires precise time synchronization between the transmitter and receiver, which can be challenging in distributed systems.

Time Difference of Arrival (TDoA)

TDoA infers range differences by measuring the difference in arrival times at multiple receivers:

$$\Delta d = c \cdot (t_i - t_j), \tag{2.2}$$

where t_i and t_j are the signal arrival times at receivers i and j, respectively.

Limitation: While it avoids the need for synchronization with the transmitter, TDoA still requires precise inter-receiver synchronization and is sensitive to NLoS-induced biases.

Round-Trip Time (RTT)

RTT determines distance by measuring the round-trip time between two devices:

$$d = \frac{c}{2} \cdot (t_{\text{round}} - t_{\text{proc}}), \tag{2.3}$$

where t_{round} is the round-trip duration and t_{proc} represents internal processing delays.

Advantage: RTT does not require synchronized clocks, making it suitable for systems like Wi-Fi or UWB.

Limitation: Its accuracy depends on precise estimation and compensation of t_{proc} .

Challenges of Time-Based Methods

While time-based methods can achieve high accuracy under LoS conditions, their performance often degrades in practical scenarios. Key challenges include:

- Synchronization Overhead: Achieving tight synchronization typically requires costly hardware or centralized control.
- Bandwidth Limitations: High-resolution delay estimation demands wide bandwidths, which are often unavailable in commercial systems.
- NLoS Bias: In blocked LoS scenarios, the first arriving path may not correspond to the shortest distance, causing overestimated ranges.
- Hardware Delay Variability: Variability in RF and digital processing delays can introduce persistent biases unless carefully calibrated.

2.2.2 RSSI-Based Ranging

RSSI-based ranging estimates distance by relating the received signal power to the transmitter-receiver separation through a path loss model:

$$P_r(d) = P_t - 10n \log_{10}(d) + X_\sigma, \tag{2.4}$$

where n is the path loss exponent and X_{σ} is a Gaussian random variable modeling shadowing effects. This method is appealing due to its simplicity and minimal infrastructure requirements.

Limitations: Despite its practicality, RSSI-based ranging has several drawbacks:

- Low Resolution: It collapses the multipath-rich channel into a single scalar value, discarding valuable structural information.
- **High Sensitivity:** Received power varies significantly due to environmental dynamics, obstacles, and interference, making the method unreliable in changing conditions.
- Model Dependence: Accurate ranging relies heavily on the path loss model, which must be empirically calibrated for each environment.

2.2.3 Empirical CSI-Based Ranging

In recent years, Channel State Information (CSI) has emerged as a promising foundation for fine-grained ranging and localization. CSI provides detailed frequency response information of the wireless channel, capturing multipath propagation, fading, and delay spread. Compared to coarse metrics like RSSI, CSI offers richer observability and finer spatial resolution.

Empirical and Learning-Based Approaches

Early CSI-based ranging approaches are typically data-driven. Some methods use regression or polynomial curve fitting to map CSI amplitudes (e.g., Frobenius norm or average subcarrier magnitude) to distance. Others leverage machine learning models—such as support vector regression, random forests, or deep neural networks—to learn relationships between CSI features and range or location labels. These approaches have shown good empirical performance, particularly in line-of-sight or static environments.

Fingerprinting techniques, which match observed CSI to a pre-recorded database, are also widely used in indoor localization. However, they require extensive training data and frequent recalibration.

Limitations of Existing Methods

Although empirically effective, these methods face several challenges:

- Black-box nature: Model parameters often lack physical interpretability, making generalization and debugging difficult.
- Environment dependence: Most methods require environment-specific training, reducing portability and robustness.
- **Absence of theoretical bounds:** Performance is typically evaluated empirically, with little understanding of fundamental estimation limits.
- Neglect of multipath structure: Many models treat CSI as a monolithic feature vector, overlooking the rich temporal and spatial structure inherent in multipath propagation.

2.2.4 PDP-Based Ranging

To address these shortcomings, an alternative approach is to decompose the CSI into its constituent multipath components—capturing the delay, amplitude, and phase of each propagation path—and build physically motivated statistical models around them. This approach integrates propagation physics with statistical estimation theory, offering both interpretability and theoretical guarantees.

In OFDM systems, the channel impulse response (CIR) can be extracted via frequency-to-time transformation. The resulting Power Delay Profile (PDP) reveals the energy of different multipath components across delays.

In this work, we propose a model-driven CSI-based ranging method that leverages the structure of the PDP. The core idea is to:

• Identify and resolve individual paths from the PDP;

- Assume each path undergoes statistical fading, with power dependent on propagation distance;
- Use known delay differences to relate NLoS paths to the LoS anchor path;
- Construct a statistical framework where path amplitudes serve as observations for inferring the underlying LoS distance.

By adopting this decomposition, we bridge the gap between empirical CSI usage and physically grounded modeling. Our formulation enables the derivation of Cramér–Rao Bounds (CRBs) for both joint and marginal estimation scenarios, providing insights into the fundamental performance limits of these methods in multipath-rich environments.

In the next section, we detail the system model and assumptions that support this formulation.

2.3 System Model and Statistical Assumptions

To evaluate the fundamental performance limits of RSSI- and PDP-based ranging, we establish a unified signal and propagation model that captures the essential characteristics of multipath wireless channels. This model forms the analytical basis for the derivation of Cramér–Rao Bounds (CRBs) in subsequent sections.

OFDM Model With Non-Fractional Delay

The OFDM model we are considering assumes an OFDM symbol length of L, consisting of a Line-of-Sight (LoS) path and K Non-Line-of-Sight (NLoS) propagation paths. This model operates with a sampling period of T_s and an OFDM symbol period of T_0 . One advantage the OFDM model is the elimination of need for precise knowledge of the pulse shape, as it makes use of pilot subcarriers within the pulse shape's passband.

The received signal vector **y** in the OFDM system can be expressed as:

$$y = XTa + v = Ha + v, \tag{2.5}$$

where the received signal vector $\mathbf{v} \in \mathcal{C}^{L \times 1}$ is defined as:

$$\mathbf{y} = \begin{bmatrix} y[s_1] \\ \vdots \\ y[s_L] \end{bmatrix}; \tag{2.6}$$

The matrix $\mathbf{X} \in \mathcal{C}^{L \times L}$ is filled with pilots and given by:

$$\mathbf{X} = \begin{bmatrix} X[s_1]e^{\frac{j2\pi s_1 T_0}{LT_s}} & \cdots & 0 \\ \vdots & \ddots & \vdots \\ 0 & \cdots & X[s_L]e^{\frac{j2\pi s_L T_0}{LT_s}} \end{bmatrix};$$
 (2.7)

The matrix $\mathbf{T} \in \mathcal{C}^{(L \times (K+1))}$ includes pulse shape filtered delayed path responses and is shown as:

$$\mathbf{T} = \begin{bmatrix} P[f_{s_1}]e^{\frac{-j2\pi s_1\tau_0}{LT_s}} & \cdots & P[f_{s_1}]e^{\frac{-j2\pi s_1\tau_K}{LT_s}} \\ \vdots & \ddots & \vdots \\ P[f_{s_L}]e^{\frac{-j2\pi s_L\tau_0}{LT_s}} & \cdots & P[f_{s_L}]e^{\frac{-j2\pi s_1\tau_K}{LT_s}} \end{bmatrix},$$
(2.8)

where τ and P represent the propagation delay and the pulse shape, respectively.

The vector $\mathbf{a} \in \mathcal{C}^{(K+1)\times 1}$ indicates the complex attenuation coefficient (amplitude $\mathbf{m} \in \mathcal{C}^{(K+1)}$ and phase $\phi \in \mathcal{C}^{(K+1)}$) and is presented as:

$$\mathbf{a} = \begin{bmatrix} a_0 \\ \vdots \\ a_K \end{bmatrix} = \begin{bmatrix} m_0 e^{j\phi_0} \\ \vdots \\ m_K e^{j\phi_K} \end{bmatrix} = \mathcal{D}(e^{j\phi})\mathbf{m} = \mathcal{D}(\mathbf{m})e^{j\phi}, \tag{2.9}$$

where $\mathcal{D}(*)$ represents an operation that converts a vector to a diagonal matrix. The vector $\mathbf{v} \in \mathcal{C}^{L \times 1}$ is a complex Gaussian noise vector, and each element v_i follows a distribution $\mathcal{CN}(0, \sigma_v^2)$.

Firstly, we assume that each ϕ_i in ϕ is an independent and identically distributed (i.i.d.) random variable drawn from a uniform distribution on the interval $[0, 2\pi)$.

Secondly, we consider the matrix X to be known and T to have been estimated prior to ranging estimation. Additionally, we presume that the estimation error of T is negligible, as this chapter does not focus on examining its bias impact.

Furthermore, we assume that the multipath scenario includes distinguishable LoS path and NLoS paths. In this context, each delay τ_i between the i_{th} NLoS path and the LoS path is measurable with negligible error. This assumption is grounded in the understanding that the measurement of delays is considerably more accurate compared to the estimation of path complex amplitudes.

Additionally, we assume that the majority of the system's subcarriers are within the pulse shape's passband. In this region, the function P(f) representing the pulse shape is approximately equal to 1. This assumption simplifies the model by considering that most subcarriers experience minimal distortion or attenuation within the passband.

Rayleigh Fading Amplitudes

According to the Saleh-Valenzuela model [104], by identifying the first ray of each cluster as the LoS path and the remaining rays as NLoS paths, the probability density function of the fading amplitude m_k for the k-th path can be described by a Rayleigh distribution:

$$f(m_k|\sigma_{d_k}^2) = \frac{2m_k}{\sigma_{d_k}^2} e^{-\frac{m_k^2}{\sigma_{d_k}^2}},$$
(2.10)

where $\sigma_{d_k}^2$ represents the average power gain of the k-th path. It is evident that $\sigma_{d_k}^2$ is associated with the propagation distance d_k of the k-th path.

LoS + Reverberating NLoS PDP Mode

According to the indoor model proposed by G. Steinböck et al. [105], the average power gain can be decomposed into the primary LoS component and the NLoS reverberating component. The gain of the LoS and NLoS paths at a distance d is given by:

$$G(d) = \begin{cases} G_0 \left(\frac{d_{\text{ref}}}{d}\right)^n; & \text{LoS,} \\ G_0 \left(\frac{d_{\text{ref}}}{d}\right)^n + G_{0,\text{rev}} T e^{\frac{-d}{cT}}; & \text{NLoS,} \end{cases}$$
(2.11)

where G_0 represents the gain at an arbitrary reference distance d_{ref} , $G_{0,\text{rev}}$ is the reference gain of the reverberant component, T is the reverberation time, c is the speed of light, and n is the environment path gain exponent.

For ranging estimation, we assume that the values of G_0 and $G_{0,rev}$ at a reference distance of 1 meter and the value of T are known prior information. Therefore, for each path k with a distance d_k , the average expected gain $\sigma_{d_k}^2$ can be expressed as:

$$\sigma_{d_k}^2 = G(d_k) = \begin{cases} G_0 d_0^{-n}; & k = 0, \\ G_0 d_k^{-n} + G_1 e^{\frac{-d_k}{cT}}; & k \neq 0, \end{cases}$$
 (2.12)

where G_1 represents $G_{0,rev}T$. Furthermore, $\sigma_{d_k}^2$ in (2.10) is a specific expression of $G(d_k)$. Additionally, for each NLoS path distance d_k , it can be represented as:

$$d_k = d_0 + c\tau_k, \tag{2.13}$$

where τ_k is the delay time from the LoS path to the k-th NLoS path, and it is measurable with negligible error as previously hypothesized.

This formulation provides a realistic model for multipath power decay in indoor and dense environments, where both direct and scattered components coexist. The next section presents the derivation of the corresponding Cramér–Rao Bound under joint parameter estimation.

2.4 CRBs for RSS-based Ranging and PDP-based Ranging

We assume that the path delays τ_k are precisely measurable using high-resolution OFDM channel sounding. This assumption allows us to treat all τ_k as known parameters. Consequently, the estimation objective reduces to inferring the LoS propagation distance d_0 , which implicitly governs the power distribution across all resolved paths.

2.4.1 Joint Range Estimation CRB for PDP-Based Ranging

To model the LoS path distance d_0 , we apply a Markov chain, disregarding any information about d_0 in ϕ and \mathbf{T} . This means that we consider d_0 to be independent of the complex attenuation coefficients and the pulse shape filtered delayed path response.

By ignoring the information about d_0 in ϕ and \mathbf{T} , we assume that the variations or dynamics of d_0 do not directly affect or depend on the complex attenuation coefficients or the pulse shape filtered delayed path response. Instead, the evolution of d_0 is modeled using a Markov chain, where the future values of d_0 only depend on its current state and not on its past states.

For the joint parameters estimation of $\boldsymbol{\theta} = [d_0, \mathbf{m}, \boldsymbol{\phi}]$, we can express the Fisher Information Matrix (FIM) as below:

$$\mathbf{FIM} = E_{\mathbf{y},\mathbf{m},\phi} \left[-\frac{\partial^2 \log f(\mathbf{y},\mathbf{m},\phi|d_0)}{\partial \theta \partial \theta^{\mathsf{T}}} \right] = E_{\mathbf{y},\mathbf{m},\phi} \begin{bmatrix} J_{d_0d_0} & J_{d_0\mathbf{m}} & J_{d_0\phi} \\ J_{\mathbf{m}d_0} & J_{\mathbf{m}\mathbf{m}} & J_{\mathbf{m}\phi} \\ J_{\phi d_0} & J_{\phi\mathbf{m}} & J_{\phi\phi} \end{bmatrix}, \qquad (2.14)$$

where τ is matrix transpose operator and the probability density function (pdf) $f(\mathbf{y}, \mathbf{m}, \boldsymbol{\phi}|d_0)$ can be expressed as follows:

$$f(\mathbf{y}, \mathbf{m}, \boldsymbol{\phi}|d_0) = f(\mathbf{y}|\mathbf{m}, \boldsymbol{\phi})f(\mathbf{m}|d_0)f(\boldsymbol{\phi}). \tag{2.15}$$

Within the context of (2.15), it is possible to represent each pdf as follows:

$$f(\mathbf{y}|\mathbf{m}, \boldsymbol{\phi}) = \frac{1}{\pi^L \sigma_v^{2L}} \exp\left(-\frac{(\mathbf{y} - \mathbf{H}\mathcal{D}(\mathbf{m})e^{j\boldsymbol{\phi}})^H (\mathbf{y} - \mathbf{H}\mathcal{D}(\mathbf{m})e^{j\boldsymbol{\phi}})}{\sigma_v^2}\right), \tag{2.16}$$

$$f(\mathbf{m}|d_0) = \prod_{k=0}^{k=K} f(m_k|\sigma_{d_k}^2(d_0)) = \prod_{k=0}^{k=K} \frac{2m_k}{\sigma_{d_k}^2(d_0)} e^{-\frac{m_k^2}{\sigma_{d_k}^2(d_0)}},$$
(2.17)

$$f(\phi) = \prod_{k=0}^{k=K} f(\phi_k) = \left(\frac{1}{2\pi}\right)^{K+1}.$$
 (2.18)

where $()^H$ denotes the conjugate transpose. Upon logarithmically processing (2.15), we obtain:

$$\log f(\mathbf{y}, \mathbf{m}, \boldsymbol{\phi}|d_0) = \log f(\mathbf{y}|\mathbf{m}, \boldsymbol{\phi}) + \log f(\mathbf{m}|d_0) + \log f(\boldsymbol{\phi}). \tag{2.19}$$

Through the process of derivation, we can express each element inside (2.14) as follows:

$$J_{d_0 d_0} = -\frac{\partial^2 \log f(\mathbf{m}|d_0)}{\partial d_0^2},\tag{2.20}$$

$$J_{d_0 \mathbf{m}} = J_{\mathbf{m} d_0}^{\mathsf{T}} = -\frac{\partial^2 \log f(\mathbf{m} | d_0)}{\partial d_0 \partial \mathbf{m}^{\mathsf{T}}},$$
(2.21)

$$J_{d_0\phi} = J_{\phi d_0}^{\mathsf{T}} = -\frac{\partial^2 \log f(\mathbf{y}, \mathbf{m}, \phi | d_0)}{\partial d_0 \partial \phi^{\mathsf{T}}} = \mathbf{0},$$
(2.22)

$$J_{\mathbf{mm}} = -\frac{\partial^2 \log f(\mathbf{y}|\mathbf{m}, \boldsymbol{\phi})}{\partial \mathbf{m} \partial \mathbf{m}^{\mathsf{T}}} - \frac{\partial^2 \log f(\mathbf{m}|d_0)}{\partial \mathbf{m} \partial \mathbf{m}^{\mathsf{T}}}, \tag{2.23}$$

$$J_{\mathbf{mm}} = -\frac{\partial^2 \log f(\mathbf{y}|\mathbf{m}, \boldsymbol{\phi})}{\partial \mathbf{m} \partial \mathbf{m}^{\mathsf{T}}} - \frac{\partial^2 \log f(\mathbf{m}|d_0)}{\partial \mathbf{m} \partial \mathbf{m}^{\mathsf{T}}},$$

$$J_{\boldsymbol{\phi}\boldsymbol{\phi}} = -\frac{\partial^2 \log f(\mathbf{y}|\mathbf{m}, \boldsymbol{\phi})}{\partial \boldsymbol{\phi} \partial \boldsymbol{\phi}^{\mathsf{T}}} - \frac{\partial^2 \log f(\boldsymbol{\phi})}{\partial \boldsymbol{\phi} \partial \boldsymbol{\phi}^{\mathsf{T}}},$$
(2.23)

$$J_{\mathbf{m}\phi} = J_{\phi\mathbf{m}}^{\mathsf{T}} = -\frac{\partial^2 \log f(\mathbf{y}|\mathbf{m}, \phi)}{\partial \mathbf{m} \partial \phi^{\mathsf{T}}}.$$
 (2.25)

Utilizing Equation (2.14), we can calculate the CRB of d_0 when performing joint parameters estimation:

$$CRB_{d_0} = \{E_{\mathbf{y},\mathbf{m},\phi}[J_{d_0d_0}] - E_{\mathbf{y},\mathbf{m},\phi}[J_{d_0\mathbf{m}}][E_{\mathbf{y},\mathbf{m},\phi}[J_{\mathbf{m}\mathbf{m}}]]^{-1}E_{\mathbf{y},\mathbf{m},\phi}[J_{\mathbf{m}d_0}]\}^{-1}.$$
 (2.26)

The expectations w.r.t. \mathbf{m} , $\boldsymbol{\phi}$, and \mathbf{y} inside (5.48) can be expressed as follows:

$$E_{\mathbf{y},\mathbf{m},\phi}J_{\mathbf{mm}} = \frac{2}{\sigma_v^2}diag(\mathbf{H}^H\mathbf{H} + \frac{1}{2}\mathbf{I}), \qquad (2.27)$$

$$E_{\mathbf{y},\mathbf{m},\phi}J_{d_0d_0} = G_0 n^2 d_0^{-(n+2)} + \sum_{k=1}^K \left(\frac{nG_0 d_k^{-n-1} + \frac{G_1}{cT} e^{\frac{-d_k}{cT}}}{G_0 d_k^{-n} + G_1 e^{\frac{-d_k}{cT}}} \right)^2, \tag{2.28}$$

$$E_{\mathbf{y},\mathbf{m},\phi}J_{d_0\mathbf{m}} = E_{\mathbf{y},\mathbf{m},\phi}J_{\mathbf{m}d_0}^{\mathsf{T}} = \left[n\pi d_0^{\frac{n-2}{2}} G_0^{-\frac{1}{2}}, \cdots, \frac{\sqrt{\pi} \left(\frac{G_0 n}{d_k^{n+1}} + \frac{G_1 e^{-\frac{d_k}{T_c}}}{T c} \right)}{\left(G_1 e^{-\frac{d_k}{T_c}} + \frac{G_0}{d_k^{n}} \right)^{3/2}}, \cdots \right], \quad (2.29)$$

where diag() is the operation of retaining the diagonal elements while setting all the non-diagonal elements to 0 of the matrix and I represents the identity matrix.

Having considered all the factors mentioned earlier, we can now proceed to calculate the joint estimation CRB for the estimation of d_0 w.r.t. PDP-based ranging:

$$CRB_{d_0} = \left[\sum_{k=1}^{K} \left(\frac{nG_0 d_k^{-n-1} + \frac{G_1}{cT} e^{\frac{-d_k}{cT}}}{G_0 d_k^{-n} + G_1 e^{\frac{-d_k}{cT}}} \right)^2 + G_0 n^2 d_0^{-(n+2)} - \frac{\sigma_v^2 \pi n^2 d_0^{(n-2)}}{2G_0} \left(\sum_{l=1}^{L} |h_{l0}|^2 + \frac{1}{2} \right)^{-1} - \frac{\sigma_v^2 \pi}{2} \sum_{k=1}^{K} \frac{\left(\frac{G_0 n}{d_k^{n+1}} + \frac{G_1 e^{-\frac{d_k}{T_c}}}{T_c} \right)^2}{\left(G_1 e^{-\frac{d_k}{T_c}} + \frac{G_0}{d_k^n} \right)^3} \left(\sum_{l=1}^{L} |h_{lk}|^2 + \frac{1}{2} \right)^{-1} \right]^{-1}.$$

$$(2.30)$$

2.4.2 Marginalized Range Estimation CRB for PDP-Based Ranging

According to (2.10), the NLoS path complex attenuation coefficients $\mathbf{a} \in \mathcal{C}^{(K+1)\times 1}$ that each element a_k is an i.i.d. complex zero-mean Gaussian random variable can be expressed as follows:

$$\mathbf{a} \sim \mathcal{CN}(0, \mathbf{C_{aa}}), \quad \mathbf{C_{aa}} = \begin{bmatrix} \sigma_{d_0}^2 & \cdots & 0 \\ \vdots & \ddots & \vdots \\ 0 & \cdots & \sigma_{d_K}^2 \end{bmatrix}. \tag{2.31}$$

To estimate d_0 directly and solely based on $\mathbf{y} \in \mathcal{C}^{L \times 1}$, we can establish the pdf of \mathbf{y} given $\sigma^2(d_0) \in \mathcal{R}^{(K+1) \times 1}$ as follows:

$$f(\mathbf{y}|\sigma^2(d_0)) = \pi^{-L}(\det(\mathbf{C}_{\mathbf{y}\mathbf{y}}))^{-1} e^{-\mathbf{y}^H \mathbf{C}_{\mathbf{y}\mathbf{y}}^{-1} \mathbf{y}},$$
(2.32)

where

$$\mathbf{C}_{\mathbf{y}\mathbf{y}} = \mathbf{H}\mathbf{C}_{\mathbf{a}\mathbf{a}}\mathbf{H}^H + \sigma_v^2\mathbf{I}, \quad \sigma^2(d_0) = [\sigma_{d_0}^2 \cdots \sigma_{d_K}^2]^{\mathsf{T}}. \tag{2.33}$$

To compute the FIM from the pdf $f(\mathbf{y}|\sigma^2(d_0))$, which is Gaussian with zero mean and covariance $\mathbf{C}_{\mathbf{y}\mathbf{y}}$, the FIM can be calculated as follows:

$$J_{d_0 d_0} = \left(\frac{\partial \sigma^2(d_0)}{\partial d_0}\right)^{\mathsf{T}} \mathbf{J}_{\sigma^2(d_0)\sigma^2(d_0)} \left(\frac{\partial \sigma^2(d_0)}{\partial d_0}\right). \tag{2.34}$$

For $\mathbf{J}_{\sigma^2(d_0)\sigma^2(d_0)}$, its element $\mathbf{J}_{\sigma^2(d_0)\sigma^2(d_0)_{i,k}}$ can be derived as:

$$\mathbf{J}_{\sigma^{2}(d_{0})\sigma^{2}(d_{0})_{i,k}} = tr \left\{ \mathbf{C}_{\mathbf{y}\mathbf{y}} \frac{\partial \mathbf{C}_{\mathbf{y}\mathbf{y}}^{-1}}{\partial \sigma_{di}^{2}} \mathbf{C}_{\mathbf{y}\mathbf{y}} \frac{\partial \mathbf{C}_{\mathbf{y}\mathbf{y}}^{-1}}{\partial \sigma_{dk}^{2}} \right\} = |\mathbf{e}_{\mathbf{i}}^{H} \mathbf{H}^{H} \mathbf{C}_{\mathbf{y}\mathbf{y}}^{-1} \mathbf{H} \mathbf{e}_{\mathbf{k}}|^{2}.$$
(2.35)

where $\mathbf{e}_i \in \mathcal{R}^{(K+1)\times 1}$ is a column vector with the *i*-th element being 1 and all other elements being 0. The trace operation, denoted by $tr(\cdot)$, computes the sum of the diagonal elements of a matrix. With these definitions, we can compute the FIM as follows:

$$\mathbf{J}_{\sigma^2(d_0)\sigma^2(d_0)} = (\mathbf{H}^H \mathbf{C}_{\mathbf{y}\mathbf{y}}^{-1} \mathbf{H}) \odot (\mathbf{H}^H \mathbf{C}_{\mathbf{y}\mathbf{y}}^{-1} \mathbf{H})^*, \tag{2.36}$$

where \odot represents the Hadamard product (element-wise multiplication) and * denotes the conjugate operation. And

$$\frac{\partial \sigma^2(d_0)}{\partial d_0} = \left[\frac{\partial \sigma_{d_0}^2}{\partial d_0} \cdots \frac{\partial \sigma_{d_K}^2}{\partial d_0} \right]^{\mathsf{T}}, \tag{2.37}$$

where k_{th} element can be presented as:

$$\frac{\partial \sigma_{dk}^2}{\partial d_0} = \begin{cases}
-nG_0 d_0^{-n-1}, & k = 0, \\
-nG_0 d_k^{-n-1} - \frac{G_1}{cT} e^{\frac{-d_k}{cT}}, & k \neq 0.
\end{cases}$$
(2.38)

In conclusion, with (2.35) (2.36) and (2.37), the marginalized CRB of d_0 w.r.t. PDP-based ranging can be calculated as follows:

$$CRB_{d_0} = \left[\left(\frac{\partial \sigma^2(d_0)}{\partial d_0} \right)^{\mathsf{T}} \mathbf{J}_{\sigma^2(d_0)\sigma^2(d_0)} \left(\frac{\partial \sigma^2(d_0)}{\partial d_0} \right) \right]^{-1}. \tag{2.39}$$

2.4.3 CRB For Classical RSSI-Based Ranging

In the case where all data subcarriers can be used and considering the channel model, the RSSI can be measured from the squared Euclidean norm of the magnitude vector \mathbf{y} . Taking into account the law of large numbers, we can express $\|\mathbf{y}\|^2$ as:

$$\|\mathbf{y}\|^2 = E_v \|\mathbf{y}\|^2, \tag{2.40}$$

This expression represents the sum of squared magnitudes of the individual subcarriers.

Utilizing the squared Euclidean norm, the RSSI measurement provides an aggregate measure of the received signal strength across all the subcarriers, enabling an overall assessment of the signal power.

Since we assume that most of the subcarriers used for transmission are within the passband of the pulse slope where $P(f) \approx 1$, $E_v ||\mathbf{y}||^2$ can be derived to:

$$E_V \|\mathbf{y}\|^2 = \alpha \|\mathbf{a}\|^2 + \beta = (\sum_{i=1}^L X_i^2) \|\mathbf{a}\|^2 + L\sigma_v^2, \tag{2.41}$$

where

$$\|\mathbf{a}\|^2 = \sum_{k=0}^K |a_k|^2 = \sum_{k=0}^K (a_k^{re2} + a_k^{im2}).$$
 (2.42)

Using pilots to estimate the channel and perform interference cancellation, the complex attenuation coefficient $a_k = a_k^{re} + j a_k^{im}$ can be decomposed into its real part a_k^{re} and imaginary part a_k^{im} , both of which are Gaussian random variables. Specifically, we have $a_k^{re} \sim \mathcal{N}(0, \frac{\sigma_k^2}{2})$ and $a_k^{im} \sim \mathcal{N}(0, \frac{\sigma_k^2}{2})$.

For the LoS path (k = 0) and NLoS paths $(k \neq 0)$, the variances σ_k^2 of the complex attenuation coefficients can be given as follows:

• For the LoS path
$$(k = 0)$$
:
$$\sigma_0^2 = G_0 d_0^{-n}, \qquad (2.43)$$

• For the NLoS paths $(k \neq 0)$:

$$\sigma_k^2 = G_0 d_k^{-n} + G_1 e^{\frac{-d_k}{cT}}, \tag{2.44}$$

where G_0 is the gain at an arbitrary reference distance d_{ref} , G_1 is the reference gain of the reverberant component, n is the environment path gain exponent, c is the speed of light, and T is the reverberation time. The variables d_0 and d_k represent the distances of the LoS path and NLoS paths, respectively.

Therefore, the real part a_k^{re} and imaginary part a_k^{im} of a_k are Gaussian random variables with variances $\frac{\sigma_k^2}{2}$, where σ_k^2 is given by the expressions mentioned above. If we assume

Table 2.1: Parameters setting for CRB Comparisons

Parameter	Value
Signal-to-Noise Ratio (SNR)	range from 10 dB to 60 dB, default 20 dB.
L	30
n	ranging from 2.0 to 2.5, default 2.0.
K	random between 10 and 15.
$d_0 \; (\mathrm{m})$	20
Propagation distance of NLoS path (m)	random between $1.1d_0$ to $2.0d_0$.
G_0	1
G_1	1
T (ns)	20

that the real part a_k^{re} and imaginary part a_k^{im} of a_k have the same variance σ_0^2 for all k, then the magnitude squared $\|\mathbf{a}\|^2$ follows a Chi-squared distribution with 2(K+1) degrees of freedom. The probability density function (PDF) of the random variable $z = |\mathbf{a}|^2$ given σ_0 can be expressed as:

$$f_{(2K+2)}(z|\sigma_0^2) = \frac{z^K e^{-\frac{z}{\sigma_0^2}}}{\sigma_0^{2(K+1)} \Gamma(K+1)}.$$
 (2.45)

Replacing σ_0^2 by a function of d_0 , we can rewrite the pdf of the random variable $z = ||\mathbf{a}||^2$ as:

$$f_{(2K+2)}(z|d_0) = \frac{z^K e^{-\frac{z}{G_0(\frac{1}{d_0})^n}}}{\left(G_0(\frac{1}{d_0})^n\right)^{(K+1)}\Gamma(K+1)},$$
(2.46)

where $\Gamma()$ is Gamma function and d_{ref} is chosen as 1 meter. It is easily to get:

$$E_Z(z) = \sigma_0^2(K+1). (2.47)$$

Then we can calculate CRB of estimating d_0 from $\|\mathbf{a}\|^2$ w.r.t. classical RSSI-based ranging as

$$CRB_{d_0} = \frac{d_0^2}{n^2(K+1)}. (2.48)$$

In the next section, we present numerical simulations comparing these CRBs under various SNRs and propagation conditions to assess the practical gap between RSSI- and PDP-based ranging.

2.5 Numerical Results and Analysis

In this section, we utilize MATLAB to compute the CRB for PDP-based ranging using joint parameter estimation and marginalized range estimation, as well as classical RSSI-based ranging. The key parameters employed in the simulations are outlined in Table 6.1.

To investigate the factors influencing ranging error, we focus on two primary factors: the Signal-to-Noise Ratio (SNR) of the channel and the path gain exponent. For each factor, we keep all other parameters at their default values and conduct the simulation to observe the behavior of the CRB.

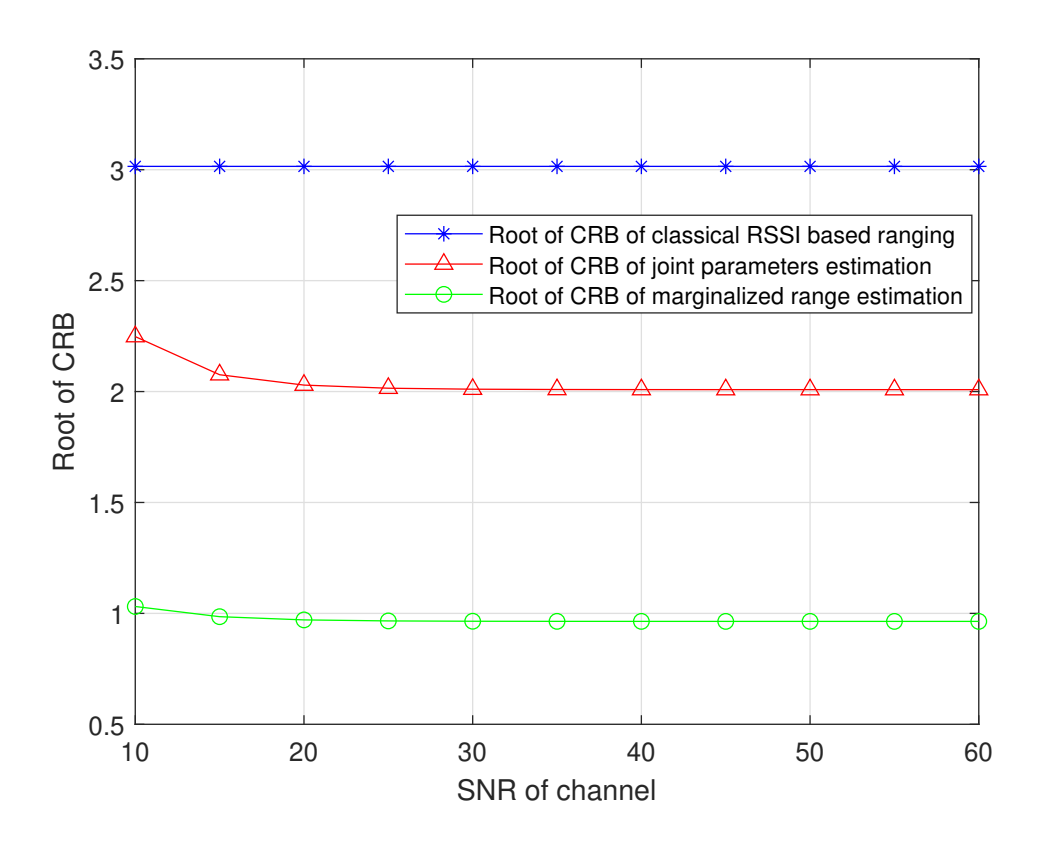


Figure 2.1: Comparision under different SNR with n=2.

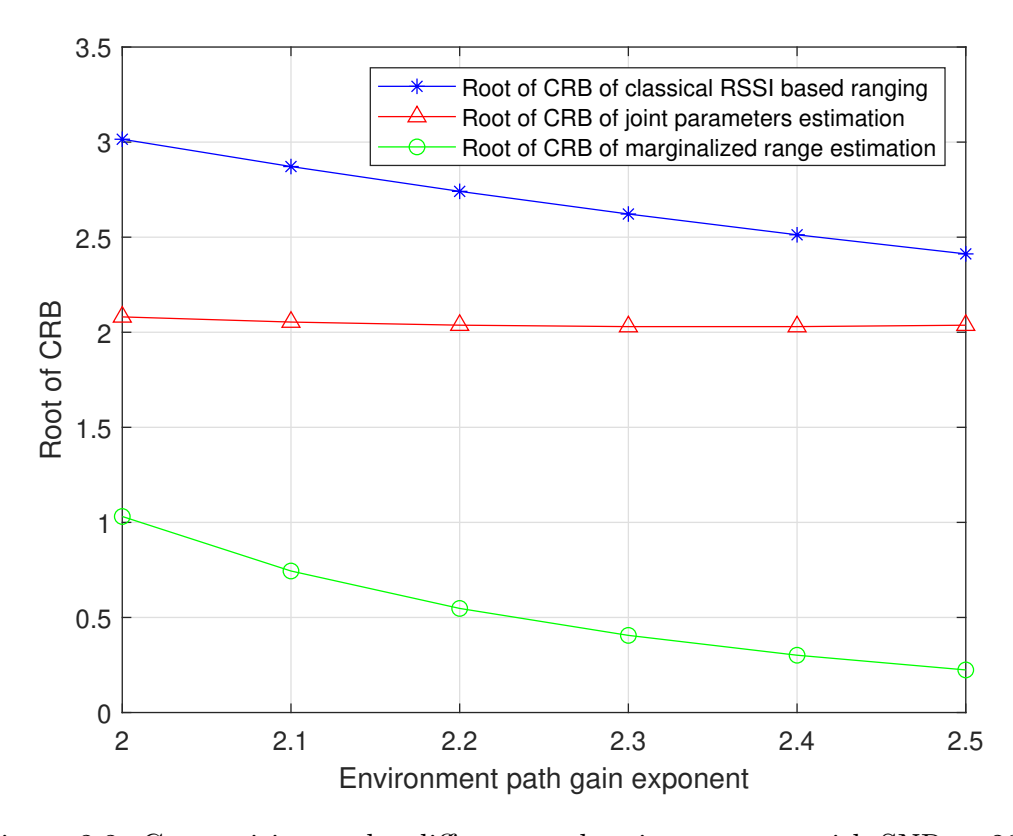


Figure 2.2: Comparision under different path gain exponent with SNR = 20dB.

The obtained performance results are presented in two figures. Figure 2.1 illustrates the behavior of the square root of the CRB for PDP-based ranging as the SNR increases from 10 dB to 60 dB. As expected, the root of the CRB decreases with higher SNR, indicating improved ranging accuracy due to the higher quality of the received signal. Notably, the performance of PDP-based ranging surpasses that of RSSI-based ranging. Moreover, marginalized range estimation demonstrates superior performance compared to joint estimation.

Figure 2.2 compares the CRBs of PDP-based ranging and RSSI-based ranging for various path gain exponents. As the path gain exponent increases, indicating more complex propagation environments, all CRBs decrease. However, PDP-based ranging exhibits better theoretical performance than RSSI-based ranging across all path gain exponents. This suggests that PDP-based ranging can deliver favorable performance even in complex environments, making it a promising technique for ranging applications. Furthermore, marginalized range estimation outperforms joint estimation in terms of ranging accuracy. These findings highlight the advantages of PDP-based ranging and marginalized range estimation, supporting their potential for accurate ranging in diverse scenarios.

2.6 Conclusions

In summary, this chapter presents a comprehensive analysis of the Cramér–Rao Bound (CRB) for PDP-based positioning using both joint and marginalized range estimation, alongside RSSI-based ranging. The derived CRB accounts for distance-dependent path decay in both Line-of-Sight (LoS) and Non-Line-of-Sight (NLoS) paths. We investigate the impact of various factors, including the Signal-to-Noise Ratio (SNR) and the path gain exponent across different environments. Simulation results demonstrate the superiority of PDP-based ranging over RSSI-based methods, with PDP-based approaches achieving better performance in diverse scenarios. Furthermore, the marginalized range estimation approach yields improved accuracy compared to joint estimation. These findings deepen the understanding of PDP-based ranging and highlight its potential for accurate positioning in real-world environments.

Chapter 3

Estimation in Linear Systems: From Sparse Recovery to Bayesian Inference

3.1 Introduction

In the context of modern signal processing and communication systems, recovering high-dimensional structured signals from noisy or incomplete measurements has become a critical and widespread challenge. This is especially true in the framework of *PDP-based sensing*—the focus of this dissertation—where recovery tasks often involve estimating sparse or structured signals while managing uncertainty and complex statistical dependencies. Meeting these challenges demands a solid understanding of key signal estimation and statistical inference tools, as well as their interplay with hyperparameter learning. This motivates the comprehensive review and methodological derivations presented in the following sections.

Section 3.2 introduces the fundamental problem of sparse estimation in underdetermined linear systems, laying out the challenges inherent in such ill-posed scenarios. We discuss how these challenges arise from the mismatch between the number of measurements and the dimensionality of the signal, and highlight how classical and modern methods tackle these sparse recovery problems.

Section 3.3 presents a detailed treatment of linear MMSE estimation and its Gaussian approximation. These approaches leverage second-order statistical information to provide computationally efficient estimators and serve as an important baseline for sparse recovery. We also discuss their limitations when the true signal priors deviate from Gaussianity, motivating the need for more adaptive and robust inference strategies.

Section 3.4 shifts focus to the estimation of prior hyperparameters—an often over-looked but essential part of practical inference tasks. Here, we adopt the Expectation-Maximization (EM) framework to iteratively refine the hyperparameters of the prior distributions that govern the underlying signal structure. In this setting, the observation model remains fixed, while the hyperparameters are adapted to best explain the observed data. Recognizing that exact posterior inference is typically intractable, we emphasize the use of moment-matching approximations within the EM algorithm, leading to robust and scalable hyperparameter learning. This interplay between approximate E-steps and analytical or numerical M-steps ensures stable convergence while leveraging the rich statistical structures inherent in the data.

Together, these three sections lay a comprehensive foundation for the advanced methods and algorithms developed in later chapters of this dissertation. By integrating classi-

cal results, iterative inference refinements, and hyperparameter adaptation strategies, we establish a coherent framework that directly addresses the challenges of PDP-based sensing. In such scenarios, signals exhibit structured sparsity or other statistical priors that must be exploited for accurate reconstruction and efficient computation. The subsequent chapters build on these fundamental insights, presenting novel algorithms and theoretical contributions tailored to PDP-based sensing applications, demonstrating both practical relevance and theoretical rigor. Finally, Section 3.5 summarizes the key insights from these sections and clarifies how they collectively establish a solid statistical foundation for the advanced methods proposed in the remainder of this dissertation.

3.2 Sparse Estimation without Prior: Underdetermined Linear Systems

In many signal processing and inference tasks, one frequently encounters the canonical linear model:

$$\mathbf{y} = \mathbf{A}\mathbf{x} + \mathbf{v},\tag{3.1}$$

where $\mathbf{y} \in \mathbb{R}^M$ is the observed measurement vector, $\mathbf{A} \in \mathbb{R}^{M \times N}$ is a known sensing or projection matrix, $\mathbf{x} \in \mathbb{R}^N$ is the unknown signal to be recovered, and $\mathbf{v} \sim \mathcal{N}(0, \sigma_v^2 \mathbf{I})$ represents additive white Gaussian noise.

When M < N, the system is underdetermined and generally has infinitely many solutions. However, in many practical scenarios, the true signal \mathbf{x} is sparse, meaning only a few components are non-zero. This insight motivates the field of sparse estimation or compressed sensing, which aims to recover sparse signals from incomplete or compressed measurements.

This chapter introduces a family of sparse estimation methods that do not require explicit prior distributions for **x**. Methods such as Orthogonal Matching Pursuit (OMP), Approximate Message Passing (AMP), and Sparse Bayesian Learning (SBL) offer algorithmic pathways for efficiently recovering sparse signals from underdetermined systems.

Relevance to this dissertation: In later chapters, we demonstrate how similar estimation problems naturally arise in the recovery of channel impulse responses (CIR) under bandwidth-limited conditions. In such settings, classical delay estimation methods often struggle due to coarse frequency-domain sampling. By exploiting the inherent sparsity of CIRs—particularly in indoor or LoS-dominated channels—sparse estimation techniques can super-resolve delay components beyond classical Fourier resolution limits. Consequently, the methods presented here form a crucial algorithmic foundation for the practical ranging and positioning strategies developed in this thesis.

3.2.1 Orthogonal Matching Pursuit (OMP)

Orthogonal Matching Pursuit (OMP) is a widely used greedy algorithm for solving sparse linear inverse problems. It is designed to recover a K-sparse signal $\mathbf{x} \in \mathbb{R}^N$ from an underdetermined system $\mathbf{y} = \mathbf{A}\mathbf{x} + \mathbf{v}$, where $\mathbf{A} \in \mathbb{R}^{M \times N}$ with M < N.

Algorithm Intuition: OMP iteratively selects the column (atom) of **A** most correlated with the current residual, then projects the observation \mathbf{y} onto the subspace spanned by the selected atoms. This process continues until the desired number of atoms (sparsity level K) is reached.

Stopping Criteria: OMP typically terminates either after K iterations or when the residual norm falls below a pre-defined threshold ε .

Algorithm 3.1 Orthogonal Matching Pursuit (OMP)

Require: Measurement vector $\mathbf{y} \in \mathbb{R}^M$, dictionary matrix $\mathbf{A} \in \mathbb{R}^{M \times N}$, sparsity level K **Ensure:** Estimated sparse signal $\hat{\mathbf{x}} \in \mathbb{R}^N$

```
1: Initialize:
  2: Residual \mathbf{r}^{(0)} \leftarrow \mathbf{y}
 3: Support set \mathcal{S}^{(0)} \leftarrow \emptyset
  4: Iteration counter t \leftarrow 0
  5: Initial estimate \hat{\mathbf{x}} \leftarrow \mathbf{0}
 6: while t < K and \|\mathbf{r}^{(t)}\|_2 > \varepsilon do
               t \leftarrow t + 1
  7:
               Compute correlations: \mathbf{c} \leftarrow \mathbf{A}^{\top} \mathbf{r}^{(t-1)}
  8:
              Identify index: j_t \leftarrow \arg\max_j |\mathbf{c}_j|
 9:
               Update support: \mathcal{S}^{(t)} \leftarrow \mathcal{S}^{(t-1)} \cup \{j_t\}
10:
               Form submatrix: \mathbf{A}_{\mathcal{S}^{(t)}} \leftarrow \text{columns of } \mathbf{A} \text{ indexed by } \mathcal{S}^{(t)}
11:
               Solve LS problem: \hat{\mathbf{x}}_{\mathcal{S}^{(t)}} \leftarrow \arg\min_{\mathbf{z}} \|\mathbf{y} - \mathbf{A}_{\mathcal{S}^{(t)}}\mathbf{z}\|_{2}^{2}
12:
               Update residual: \mathbf{r}^{(t)} \leftarrow \mathbf{y} - \mathbf{A}_{\mathcal{S}^{(t)}} \hat{\mathbf{x}}_{\mathcal{S}^{(t)}}
13:
14: end while
15: Set \hat{\mathbf{x}} with non-zero entries at \mathcal{S}^{(t)} from \hat{\mathbf{x}}_{\mathcal{S}^{(t)}}
16: return \hat{\mathbf{x}}
```

Discussion: OMP is simple and interpretable. At each iteration, it greedily selects the atom most correlated with the residual and ensures orthogonality by solving a least squares problem. It is particularly effective when the columns of \mathbf{A} are nearly orthogonal and the noise level is low.

However, OMP can suffer from suboptimal support recovery in the presence of high noise or when the columns of **A** are highly correlated. Its performance also depends on knowing the sparsity level K or threshold ε in advance.

Advantages: Simple, fast, and easy to implement.

Limitations: Suboptimal in high-noise environments; greedy selection may lead to inaccurate support recovery.

3.2.2 Approximate Message Passing (AMP)

Approximate Message Passing (AMP) is an iterative algorithm designed for sparse signal recovery in large-scale underdetermined linear systems, particularly when the signal \mathbf{x} is sparse. AMP is derived from belief propagation and leverages statistical physics techniques to efficiently estimate \mathbf{x} under probabilistic models.

Core Principle: AMP assumes a probabilistic prior for \mathbf{x} , often a Laplacian or Bernoulli-Gaussian distribution, and iteratively refines its estimate using a residual-based correction combined with a nonlinear denoising function. A key feature of AMP is the inclusion of an Onsager correction term that improves convergence by accounting for statistical dependencies introduced during the iterative updates.

The algorithm alternates between a linear residual update and a nonlinear shrinkage step:

$$\mathbf{r}^{(t)} = \mathbf{y} - \mathbf{A}\mathbf{x}^{(t)} + \frac{1}{M}\mathbf{r}^{(t-1)} \cdot \operatorname{div}(\eta^{(t-1)}), \tag{3.2}$$

$$\mathbf{x}^{(t+1)} = \eta^{(t)} \left(\mathbf{A}^{\top} \mathbf{r}^{(t)} + \mathbf{x}^{(t)} \right), \tag{3.3}$$

where $\eta^{(t)}$ is a denoising function (e.g., soft thresholding) and $\operatorname{div}(\eta^{(t-1)})$ is its average divergence, representing the average derivative across components.

Algorithm 3.2 Approximate Message Passing (AMP)

Require: Observation $\mathbf{y} \in \mathbb{R}^M$, sensing matrix $\mathbf{A} \in \mathbb{R}^{M \times N}$, noise variance σ_v^2 , threshold λ , max iterations T

Ensure: Estimated signal $\hat{\mathbf{x}} \in \mathbb{R}^N$

```
1: Initialize: \mathbf{x}^{(0)} \leftarrow \mathbf{0}, \, \mathbf{r}^{(0)} \leftarrow \mathbf{y}
```

2: for each iteration t = 1, ..., T do

Compute pseudo-data: $\mathbf{z}^{(t)} \leftarrow \mathbf{x}^{(t-1)} + \mathbf{A}^{\top} \mathbf{r}^{(t-1)}$ 3:

Apply soft-thresholding: $x_i^{(t)} \leftarrow \text{sign}(z_i^{(t)}) \cdot \text{max}(|z_i^{(t)}| - \lambda, 0)$ for all i4:

5:

5: Compute divergence:
6:
$$\operatorname{div}(\eta) \leftarrow \frac{1}{N} \sum_{i=1}^{N} \mathbb{I}(|z_i^{(t)}| > \lambda)$$

7: Update residual:

7:

8:
$$\mathbf{r}^{(t)} \leftarrow \mathbf{y} - \mathbf{A}\mathbf{x}^{(t)} + \mathbf{r}^{(t-1)} \cdot \frac{1}{M} \cdot \operatorname{div}(\eta)$$

9: end for

10: return $\hat{\mathbf{x}} \leftarrow \mathbf{x}^{(T)}$

Advantages:

- Efficient for large-scale problems with i.i.d. Gaussian sensing matrices A;
- Fast convergence with low per-iteration computational complexity;
- Naturally incorporates statistical inference via the use of denoisers.

Limitations:

- Sensitive to the structure of A; performance can degrade for non-Gaussian or illconditioned matrices;
- Requires careful design and tuning of the denoising function and threshold parameter λ ;
- Theoretical guarantees are primarily valid in the large-system limit.

3.2.3 Sparse Bayesian Learning (SBL)

Sparse Bayesian Learning (SBL) formulates sparse signal recovery within a hierarchical Bayesian framework. Each coefficient x_i is modeled as a zero-mean Gaussian random variable with its own precision parameter α_i , enabling automatic sparsity through relevance determination.

Core Principle: SBL assigns the following prior to each element x_i :

$$p(x_i \mid \alpha_i) = \mathcal{N}(x_i \mid 0, \alpha_i^{-1}), \tag{3.4}$$

where α_i is an unknown hyperparameter that controls the variance. While a Gamma prior can be placed on α_i , in practice, point estimates are often obtained via Type-II maximum likelihood. The marginal likelihood of the data is then maximized with respect to α , which automatically prunes irrelevant coefficients by pushing the corresponding $\alpha_i \to \infty$.

Posterior Distribution: Given the observation model $\mathbf{y} = \mathbf{A}\mathbf{x} + \mathbf{v}$, where $\mathbf{v} \sim \mathcal{N}(0, \sigma_v^2 \mathbf{I})$, the posterior over \mathbf{x} is Gaussian:

$$\Sigma = \left(\frac{1}{\sigma_n^2} \mathbf{A}^\top \mathbf{A} + \operatorname{diag}(\boldsymbol{\alpha})\right)^{-1}, \tag{3.5}$$

$$\boldsymbol{\mu} = \frac{1}{\sigma_v^2} \boldsymbol{\Sigma} \mathbf{A}^\top \mathbf{y}. \tag{3.6}$$

Learning Strategy: The hyperparameters α_i are updated iteratively through evidence maximization:

$$\alpha_i \leftarrow \frac{1}{\mu_i^2 + \Sigma_{ii}}.\tag{3.7}$$

Algorithm 3.3 Sparse Bayesian Learning (SBL)

Require: Observation $\mathbf{y} \in \mathbb{R}^M$, dictionary $\mathbf{A} \in \mathbb{R}^{M \times N}$, noise variance σ_v^2 , tolerance ε Ensure: Estimated signal $\hat{\mathbf{x}} \in \mathbb{R}^N$

- 1: Initialize: $\alpha^{(0)} \leftarrow \alpha_0 \cdot \mathbf{1}, t \leftarrow 0$
- 2: repeat
- 3:

4:
$$\Sigma^{(t)} \leftarrow \left(\frac{1}{\sigma_v^2} \mathbf{A}^\top \mathbf{A} + \operatorname{diag}(\boldsymbol{\alpha}^{(t-1)})\right)^{-1}$$
5:
$$\boldsymbol{\mu}^{(t)} \leftarrow \frac{1}{\sigma_v^2} \boldsymbol{\Sigma}^{(t)} \mathbf{A}^\top \mathbf{y}$$
6:
$$\mathbf{for} \ \operatorname{each} \ i = 1, \dots, N \ \mathbf{do}$$
7:
$$\alpha_i^{(t)} \leftarrow \frac{1}{\left(\mu_i^{(t)}\right)^2 + \Sigma_{ii}^{(t)}}$$

5:
$$\boldsymbol{\mu}^{(t)} \leftarrow \frac{1}{2} \boldsymbol{\Sigma}^{(t)} \mathbf{A}^{\top} \mathbf{y}$$

- 6:
- 7:
- end for 8:
- 9: until $\|\boldsymbol{\alpha}^{(t)} \boldsymbol{\alpha}^{(t-1)}\|_2 < \varepsilon$ 10: return $\hat{\mathbf{x}} \leftarrow \boldsymbol{\mu}^{(t)}$

Advantages:

- Promotes sparsity automatically through relevance determination;
- Often outperforms convex optimization methods in highly coherent dictionaries;
- Provides full posterior uncertainty quantification for x.

Limitations:

- Computationally intensive due to matrix inversions required at each iteration;
- Sensitive to initial values and to poorly scaled sensing matrices A;
- May converge slowly in practice, particularly in high-noise settings.

Summary: In summary, we have explored three widely used sparse estimation algorithms—OMP, AMP, and SBL—each offering unique strengths and facing specific challenges. OMP is simple and effective for highly sparse signals but struggles in noisy or coherent environments. AMP leverages probabilistic insights and provides fast convergence for large-scale problems, albeit with sensitivity to system structure. SBL incorporates Bayesian inference to adaptively promote sparsity and offers robustness to coherent dictionaries, though at a higher computational cost.

To provide a clear comparison of these methods, Table 3.1 summarizes their core principles, advantages, and limitations.

Table 3.1: Comparison of Sparse Estimation Algorithms (No Prior on $\mathbf{x})$

Method	Core Principle	Advantages	Limitations
Orthogonal Matching Pur- suit (OMP)	Greedily selects atoms most correlated with the residual; reconstructs via least-squares	 Simple and interpretable Low complexity per iteration Works well with highly sparse signals 	 Sensitive to noise and correlated columns Suboptimal for moderate sparsity Requires knowledge of sparsity level
Approximate Message Passing (AMP)	Iterative refinement with Onsager correction; combines linear residual update with nonlinear denoising	 Scalable to large systems Fast convergence for Gaussian matrices Integrates probabilistic denoisers 	 Performance degrades with non-i.i.d. matrices Sensitive to denoiser and threshold Assumes large-system regime
Sparse Bayesian Learning (SBL)	Places hierarchical prior on coefficients; learns hyperparameters by maximizing marginal likelihood	 Adaptive to unknown sparsity Robust to correlated dictionaries Theoretically grounded in Bayesian inference 	 Computationally intensive (matrix inversion) May converge slowly Sensitive to hyperparameter initialization

3.3 Linear MMSE Estimation and Gaussian Approximation

We consider the standard linear observation model:

$$\mathbf{y} = \mathbf{A}\mathbf{x} + \mathbf{v},\tag{3.8}$$

where $\mathbf{x} \in \mathbb{R}^n$ is the random vector to be estimated, $\mathbf{A} \in \mathbb{R}^{m \times n}$ is a known matrix, and $\mathbf{v} \sim \mathcal{N}(\mathbf{0}, \sigma_v^2 \mathbf{I}_n)$ is white Gaussian noise independent of \mathbf{x} .

3.3.1 MMSE Estimation under Gaussian Prior

When $\mathbf{x} \sim \mathcal{N}(\boldsymbol{\mu}_x, \mathbf{C}_{xx})$ is Gaussian, the MMSE estimator is the conditional expectation, which has a closed-form solution:

$$\hat{\mathbf{x}}_{\text{MMSE}} = \mathbb{E}[\mathbf{x}|\mathbf{y}] = \boldsymbol{\mu}_x + \mathbf{C}_{xx}\mathbf{A}^{\top}(\mathbf{A}\mathbf{C}_{xx}\mathbf{A}^{\top} + \sigma_v^2\mathbf{I}_n)^{-1}(\mathbf{y} - \mathbf{A}\boldsymbol{\mu}_x), \tag{3.9}$$

$$\Sigma_{xx} = \mathbb{E}\left[(\mathbf{x} - \mathbb{E}[\mathbf{x}])(\mathbf{x} - \mathbb{E}[\mathbf{x}])^{\top} \middle| \mathbf{y} \right] = (\sigma_v^{-2} \mathbf{A}^{\top} \mathbf{A} + \mathbf{C}_{xx}^{-1})^{-1}.$$
 (3.10)

3.3.2 LMMSE for Non-Gaussian Prior via Gaussian Approximation

When \mathbf{x} is non-Gaussian, the true MMSE estimator becomes nonlinear and intractable due to high-dimensional integration. In such scenarios, we approximate \mathbf{x} by a Gaussian random vector that matches its mean $\boldsymbol{\mu}_x$ and covariance \mathbf{C}_{xx} :

$$\mathbf{x} \sim p(\mathbf{x}) \approx q(\mathbf{x}) = \mathcal{N}(\boldsymbol{\mu}_x, \mathbf{C}_{xx}).$$
 (3.11)

This approximation can be expressed as:

$$q(\mathbf{x}) = \arg\min_{q(\mathbf{x})} D_{KL}(p(\mathbf{x})||q(\mathbf{x})) = \arg\min_{q} \int p(\mathbf{x}) \log \frac{p(\mathbf{x})}{q(\mathbf{x})} d\mathbf{x},$$
(3.12)

where D_{KL} denotes the Kullback-Leibler divergence. The solution of (3.12) for a Gaussian $q(\mathbf{x})$ is obtained by matching the first and second moments:

$$\mathbb{E}_p[\mathbf{x}] = \mathbb{E}_q[\mathbf{x}], \qquad \mathbb{E}_p[\mathbf{x}\mathbf{x}^\top] = \mathbb{E}_q[\mathbf{x}\mathbf{x}^\top]. \tag{3.13}$$

This leads directly to the LMMSE estimator, which is linear in \mathbf{y} and depends only on second-order statistics:

$$\hat{\mathbf{x}}_{\text{LMMSE}} = \boldsymbol{\mu}_x + \mathbf{C}_{xx} \mathbf{A}^{\top} (\mathbf{A} \mathbf{C}_{xx} \mathbf{A}^{\top} + \sigma_v^2 \mathbf{I}_n)^{-1} (\mathbf{y} - \mathbf{A} \boldsymbol{\mu}_x). \tag{3.14}$$

Although this estimator is no longer the true MMSE solution, it is the optimal linear estimator and often yields satisfactory results. This Gaussian approximation thus provides a compelling justification for the use of LMMSE when the true distribution of \mathbf{x} is non-Gaussian.

3.3.3 Scalar Observation Model with Extrinsic Gaussian Noise

While LMMSE leverages only second-order statistics of \mathbf{x} , further improvements are possible by combining the true prior of each component x_i with a Gaussian approximation of the remaining components. This results in a scalar observation model for each variable, enabling more accurate estimation.

We isolate x_i in the measurement equation:

$$\mathbf{y} = \mathbf{A}_i x_i + \sum_{j \neq i} \mathbf{A}_j x_j + \mathbf{v} = \mathbf{A}_i x_i + \mathbf{n}_i, \tag{3.15}$$

where \mathbf{A}_i is the *i*-th column of \mathbf{A} , and $\mathbf{n}_i = \sum_{j \neq i} \mathbf{A}_j x_j + \mathbf{v}$ represents an effective noise term. We approximate $p(\mathbf{n}_i) \approx \mathcal{N}(\boldsymbol{\mu}_i, \mathbf{C}_i)$ by approximating the distributions of all x_j for $j \neq i$ using:

$$p(x_j) \approx q(x_j) = \mathcal{N}(\mu_{x_j}, \sigma_{x_j}^2), \tag{3.16}$$

where the first and second moments are matched. This yields:

$$\boldsymbol{\mu}_i = \sum_{j \neq i} \mathbf{A}_j \mu_{x_j}, \quad \mathbf{C}_i = \sum_{j \neq i} \sigma_{x_j}^2 \mathbf{A}_j \mathbf{A}_j^\top + \sigma_v^2 \mathbf{I}_n.$$
(3.17)

Consequently, the observation can be approximated as:

$$\mathbf{y} \approx \mathbf{A}_i x_i + \mathbf{z}_{\bar{i}}.\tag{3.18}$$

where $\mathbf{z}_{\bar{i}} \in \mathbb{R}^{m \times 1}$ is a Gaussian random vector with mean $\boldsymbol{\mu}_i$ and covariance \mathbf{C}_i . By treating x_i as deterministic, we obtain an equivalent scalar observation model:

$$r_i = x_i + w_i, \quad w_i \sim \mathcal{N}(0, \tau_i),$$
 (3.19)

where:

$$r_i = \frac{\mathbf{A}_i^{\top} \mathbf{C}_i^{-1} (\mathbf{y} - \boldsymbol{\mu}_i)}{\mathbf{A}_i^{\top} \mathbf{C}_i^{-1} \mathbf{A}_i}, \quad \tau_i = \frac{1}{\mathbf{A}_i^{\top} \mathbf{C}_i^{-1} \mathbf{A}_i}.$$
 (3.20)

Here, r_i is a scalar observation, and τ_i quantifies the uncertainty due to all other x_j $(j \neq i)$ and the noise vector \mathbf{v} . These terms, r_i and τ_i , are also known as the Gaussian extrinsic mean and variance.

Given the scalar model $r_i = x_i + w_i$ and the prior $p(x_i)$, the approximate posterior mean and variance are:

$$\hat{x}_i = \mathbb{E}[x_i|r_i] = \frac{\int x_i \, p(x_i) \, \mathcal{N}(r_i; x_i, \tau_i) \, \mathrm{d}x_i}{\int p(x_i) \, \mathcal{N}(r_i; x_i, \tau_i) \, \mathrm{d}x_i},\tag{3.21}$$

$$\hat{\tau}_i = \operatorname{Var}[x_i|r_i] = \frac{\int (x_i - \hat{x}_i)^2 p(x_i) \mathcal{N}(r_i; x_i, \tau_i) \, \mathrm{d}x_i}{\int p(x_i) \mathcal{N}(r_i; x_i, \tau_i) \, \mathrm{d}x_i}.$$
(3.22)

This approach preserves the true prior information of x_i , unlike the LMMSE, which relies only on its first and second moments. At the same time, it uses a Gaussian approximation for the remaining system, potentially achieving better performance than LMMSE. Moreover, this method decomposes the high-dimensional integral into multiple one-dimensional integrals, significantly reducing computational complexity compared to MMSE.

3.3.4 Iterative Gaussian Approximation from Posterior Beliefs

In the previous section, we used the scalar model:

$$r_i = x_i + w_i, \quad w_i \sim \mathcal{N}(0, \tau_i), \tag{3.23}$$

to obtain the approximate posterior distribution $\tilde{p}(x_i|r_i)$, given the true prior $p(x_i)$.

We now consider the following question: Can we find a Gaussian prior $f(x_i) = \mathcal{N}(x_i; \mu_i, \sigma_i^2)$ such that the resulting approximate Gaussian posterior $\tilde{q}(x_i|r_i)$ is as close as possible to the non-Gaussian posterior $\tilde{p}(x_i|r_i)$?

Formally, we aim to minimize the Kullback–Leibler divergence:

$$D_{KL}(\tilde{p}(x_i|r_i) || \tilde{q}(x_i|r_i)). \tag{3.24}$$

By Bayes' rule, the Gaussian posterior induced by the Gaussian prior is:

$$\tilde{q}(x_i|r_i) = \frac{f(x_i)\mathcal{N}(r_i; x_i, \tau_i^2)}{\int f(x_i)\mathcal{N}(r_i; x_i, \tau_i) \,\mathrm{d}x_i}.$$
(3.25)

This suggests that the optimal Gaussian prior $f(x_i) = \mathcal{N}(x_i; \mu_i, \sigma_i)$ is one for which the resulting posterior matches the true posterior mean and variance. Since the likelihood is Gaussian and we know the true posterior moments:

$$\hat{x}_i = \mathbb{E}[x_i|r_i], \quad \hat{\tau}_i = \text{Var}[x_i|r_i], \tag{3.26}$$

we can determine (μ_i, σ_i^2) by enforcing that the Gaussian posterior $\tilde{q}(x_i|r_i)$ has these same moments.

For scalar Gaussian models with Gaussian prior and likelihood, the posterior is also Gaussian, with:

$$\hat{x}_i = \frac{\sigma_i^2}{\sigma_i^2 + \tau_i} r_i + \frac{\tau_i}{\sigma_i^2 + \tau_i} \mu_i, \tag{3.27}$$

$$\hat{\tau}_i^2 = \left(\frac{1}{\sigma_i^2} + \frac{1}{\tau_i}\right)^{-1}.$$
 (3.28)

Thus, solving for (μ_i, σ_i^2) to match \hat{x}_i and $\hat{\tau}_i^2$ yields:

$$\sigma_i^2 = \left(\frac{1}{\hat{\tau}_i} - \frac{1}{\tau_i}\right)^{-1},\tag{3.29}$$

$$\mu_i = \frac{\left(\sigma_i^2 + \tau_i\right)\hat{x}_i - \sigma_i^2 r_i}{\tau_i}.$$
(3.30)

This ensures that the resulting posterior $\tilde{q}(x_i|r_i)$ exactly matches the true posterior in mean and variance, thus minimizing the KL divergence.

In practice, computing σ_i^2 using (3.29) can result in negative or numerically unstable values, especially when the estimated posterior variance $\hat{\tau}_i^2$ is close to the extrinsic noise variance τ_i^2 . This can yield an ill-defined Gaussian prior and destabilize the iterative process. To address this, we employ one or both of the following strategies:

• Clipping: Enforce a lower bound $\epsilon > 0$ on the prior variance:

$$\sigma_i^2 \leftarrow \max(\sigma_i^2, \epsilon), \tag{3.31}$$

where ϵ is typically set to a small value such as 10^{-6} .

• Damping: To improve numerical stability and mitigate oscillations, we apply damping to the updates of the Gaussian prior parameters. For a damping factor $\lambda \in (0,1]$, the updates are:

$$\sigma_i^{2(t)} \leftarrow (1 - \lambda) \,\sigma_i^{2(t-1)} + \lambda \,\sigma_i^{2(t)},\tag{3.32}$$

$$\mu_i^{(t)} \leftarrow (1 - \lambda) \,\mu_i^{(t-1)} + \lambda \,\mu_i^{(t)},$$
(3.33)

where λ is typically set to 0.1 or 0.5.

These techniques help ensure numerical stability and robustness, particularly in early iterations when the posterior estimates may deviate significantly from the true marginals.

This Gaussian prior is not assumed a priori; rather, it is derived directly from the posterior. Specifically, it represents a local Gaussian approximation to the true prior that best aligns with the observed data by matching the posterior moments. Importantly, this approximation is adapted individually for each variable and updated iteratively, allowing it to capture the true underlying distribution more accurately than static, global approximations like LMMSE.

By minimizing the Kullback-Leibler divergence between the true posterior and the Gaussian-induced posterior, this procedure yields the optimal Gaussian approximation (in the KL sense) for the current observation. When this process is applied to all variables and repeated iteratively, it forms a globally refined inference scheme that can significantly outperform both LMMSE and naive scalar estimators based on fixed priors.

Algorithm 3.4 Iterative Posterior-Matching Gaussian Approximation

```
1: Input: A, y, noise variance \sigma^2, prior p(x_i)
 2: Output: Posterior means \hat{\mathbf{x}}, variances \hat{\boldsymbol{\tau}}
3: Initialize: \mu_i^{(0)}, \sigma_i^{2(0)} for all i (e.g., 0 and 1)
 4: while stopping criterion not met do
 5:
             for each i = 1 to n do
                   Compute scalar observation r_i from \mathbf{y} and current \{\mu_j, \sigma_i^2\}_{j \neq i}
 6:
                    Compute posterior: \hat{x}_i = \mathbb{E}[x_i|r_i], \hat{\tau}_i = \text{Var}[x_i|r_i]
 7:
                   Update prior variance: \sigma_i^2 = \left(\frac{1}{\hat{\tau}_i} - \frac{1}{\tau_i}\right)^{-1}
 8:
                   If \sigma_i^2 < \epsilon, set \sigma_i^2 \leftarrow \epsilon
                                                                                                                                // clipping (optional)
 9:
                   Update prior mean: \mu_i = \frac{(\sigma_i^2 + \tau_i)\hat{x}_i - \sigma_i^2 r_i}{\tau_i}
Damping (optional): \mu_i \leftarrow (1 - \lambda)\mu_i^{\text{old}} + \lambda\mu_i, and similarly for \sigma_i^2
10:
11:
             end for
12:
13: end while
```

The proposed algorithm, summarized in Algorithm 3.4, shares strong conceptual foundations with several existing approximate inference frameworks, including Expectation Propagation (EP), Expectation Consistency (EC), Vector Approximate Message Passing (VAMP), and its variants such as ReVAMP. All these methods iteratively refine Gaussian approximations to the true posterior, typically through moment matching or local updates based on factorized models.

It is important to emphasize that, despite the differences in naming and algorithmic presentation, these methods are fundamentally related. In particular, VAMP can be seen as a special case of the proposed framework, where the variances of the approximate

Gaussian priors are constrained to be equal across all components, i.e., $\sigma_i^2 = \sigma^2$ for all i. This simplification reduces computational complexity and often improves convergence behavior, albeit at the cost of some flexibility.

In subsequent chapters, we may refer to various algorithmic variants or present the same core ideas under different formulations. This is not due to substantive algorithmic differences, but rather to highlight how similar approximate inference schemes can arise from diverse perspectives—such as message passing, variational inference, or statistical linearization. Presenting these viewpoints enriches the reader's understanding and illustrates the broad applicability and interpretability of the underlying principles.

3.4 Expectation-Maximization with Prior Hyperparameter Estimation

In many latent-variable estimation problems, the unknown signal $\mathbf{x} \in \mathbb{R}^N$ is modeled as a random vector with a parametric prior distribution $p(\mathbf{x} \mid \boldsymbol{\theta})$, where $\boldsymbol{\theta}$ denotes the set of hyperparameters (e.g., prior variances or scale parameters). The observation model $p(\mathbf{y} \mid \mathbf{x})$ is assumed to be known and fixed, typically Gaussian. Our goal is to estimate $\boldsymbol{\theta}$ from observations $\mathbf{y} \in \mathbb{R}^M$ using the Expectation-Maximization (EM) algorithm.

3.4.1 Marginal Likelihood and Variational Lower Bound

The marginal likelihood of the observed data is:

$$\log p(\mathbf{y} \mid \boldsymbol{\theta}) = \log \int p(\mathbf{y} \mid \mathbf{x}) p(\mathbf{x} \mid \boldsymbol{\theta}) d\mathbf{x}. \tag{3.34}$$

Direct maximization of this expression is typically intractable due to the integral over the latent variable \mathbf{x} . To address this, we introduce an auxiliary distribution $q(\mathbf{x})$ and apply Jensen's inequality:

$$\log p(\mathbf{y} \mid \boldsymbol{\theta}) = \log \int q(\mathbf{x}) \frac{p(\mathbf{y}, \mathbf{x} \mid \boldsymbol{\theta})}{q(\mathbf{x})} d\mathbf{x}$$

$$\geq \int q(\mathbf{x}) \log \frac{p(\mathbf{y}, \mathbf{x} \mid \boldsymbol{\theta})}{q(\mathbf{x})} d\mathbf{x} \triangleq \mathcal{L}(q, \boldsymbol{\theta}), \tag{3.35}$$

with equality when $q(\mathbf{x}) = p(\mathbf{x} \mid \mathbf{y}, \boldsymbol{\theta})$.

3.4.2 EM Algorithm for Prior Hyperparameter Learning

The EM algorithm maximizes the lower bound (3.35) through alternating steps. Given the current hyperparameter estimate $\boldsymbol{\theta}^{(t)}$, the steps are:

E-Step: Compute the expected log-prior under the current posterior:

$$Q(\boldsymbol{\theta} \mid \boldsymbol{\theta}^{(t)}) = \mathbb{E}_{\mathbf{x} \sim p(\mathbf{x} \mid \mathbf{y}, \boldsymbol{\theta}^{(t)})} \left[\log p(\mathbf{x} \mid \boldsymbol{\theta}) \right]. \tag{3.36}$$

M-Step: Update the hyperparameters by maximizing this expected log-prior:

$$\boldsymbol{\theta}^{(t+1)} = \arg \max_{\boldsymbol{\theta}} Q(\boldsymbol{\theta} \mid \boldsymbol{\theta}^{(t)}). \tag{3.37}$$

This iterative procedure guarantees non-decreasing marginal likelihood and typically converges to a local maximum under mild regularity conditions.

3.4.3 Approximate E-Step via Moment Matching

In practice, the exact posterior $p(\mathbf{x} \mid \mathbf{y}, \boldsymbol{\theta}^{(t)})$ is often intractable due to non-conjugate priors or complex likelihoods. To overcome this, we approximate it with a tractable distribution:

$$q(\mathbf{x}) \approx p(\mathbf{x} \mid \mathbf{y}, \boldsymbol{\theta}^{(t)}),$$
 (3.38)

chosen to match the first and second moments:

$$q(\mathbf{x}) = \prod_{i=1}^{N} \mathcal{N}(x_i \mid \hat{x}_i, \hat{\tau}_i), \tag{3.39}$$

where $\hat{x}_i = \mathbb{E}[x_i \mid \mathbf{y}]$ and $\hat{\tau}_i = \text{Var}[x_i \mid \mathbf{y}]$ are estimated using iterative inference techniques such as scalar message passing, expectation consistency (EC), or expectation propagation (EP).

Substituting this approximation into (3.36) yields:

$$Q(\boldsymbol{\theta} \mid \boldsymbol{\theta}^{(t)}) \approx \sum_{i=1}^{N} \mathbb{E}_{q(x_i)} \left[\log p(x_i \mid \boldsymbol{\theta}) \right],$$
 (3.40)

which enables analytical or numerical optimization in the M-step. The full iterative procedure is summarized in Algorithm 3.5, where the E-step uses approximate posterior moments, and the M-step performs analytic or numerical maximization.

Algorithm 3.5 EM with Approximate Posterior Moment Matching

```
Require: Observation y, prior p(\mathbf{x} \mid \boldsymbol{\theta}), likelihood p(\mathbf{y} \mid \mathbf{x}), init \boldsymbol{\theta}^{(0)}, tolerance \varepsilon
Ensure: Estimated parameter \theta^*
```

1: $t \leftarrow 0$

2: repeat

E-step: Approximate $p(\mathbf{x} \mid \mathbf{y}, \boldsymbol{\theta}^{(t)}) \approx \prod_{i} \mathcal{N}(x_i \mid \hat{x}_i^{(t)}, \hat{\tau}_i^{(t)})$ M-step: $\boldsymbol{\theta}^{(t+1)} \leftarrow \arg \max_{\boldsymbol{\theta}} \sum_{i} \mathbb{E}_{q^{(t)}(x_i)} [\log p(x_i \mid \boldsymbol{\theta})]$ 3:

4:

 $t \leftarrow t + 1$

6: **until** $\|\boldsymbol{\theta}^{(t)} - \boldsymbol{\theta}^{(t-1)}\| < \varepsilon$

7: $\mathbf{return}^{''}\boldsymbol{\theta}^* = \boldsymbol{\theta}^{(t)}$

3.5 Conclusions

In this chapter, we focused on a simplified yet practically significant EM framework in which the model parameters θ appear exclusively in the prior $p(\mathbf{x} \mid \boldsymbol{\theta})$, while the observation model $p(\mathbf{y} \mid \mathbf{x})$ remains known and fixed. This setting not only streamlines the derivation but also captures a broad range of real-world applications, including sparse signal recovery, variational Bayesian learning, and automatic relevance determination.

To address the intractability of exact posterior inference, we introduced a momentmatching approach that replaces the true posterior with a tractable Gaussian approximation. This enables the computation of approximate posterior moments in the E-step, providing a practical means to estimate hyperparameters iteratively. Crucially, these moment-based approximations preserve key features of the underlying distribution while greatly simplifying the computational burden.

The resulting EM algorithm, combining approximate E-steps with analytic or numerical M-steps, ensures a non-decreasing marginal likelihood and offers robustness in high-dimensional and complex inference tasks. By balancing computational tractability and statistical fidelity, this approach offers a powerful framework for learning hyperparameters in challenging latent-variable models.

Chapter 4

High-Resolution Power Delay Profile Estimation with Sparse Bayesian Inference

4.1 Introduction

Accurate estimation of channel delays is essential for understanding multipath characteristics in wireless propagation environments. In practice, received signal delays rarely align precisely with integer multiples of the sampling period. These non-integer, or off-grid delays significantly impact the shape and resolution of the Power Delay Profile (PDP), a key metric for characterizing multipath channels.

The PDP captures the arrival times and power levels of multipath components, serving as the foundation for many positioning and ranging applications. Specifically, PDP-based ranging methods rely heavily on accurate delay estimation to determine distances to scatterers or reflectors. Therefore, precise estimation of off-grid delays is critical for reliable PDP extraction, which directly enhances the accuracy of ranging and localization systems.

Traditional delay estimation methods typically assume delays aligned to integer multiples of the sampling grid, introducing substantial modeling errors, particularly in high-resolution scenarios. These inaccuracies obscure the true PDP structure, leading to biased distance estimates and degraded performance. To address these limitations, advanced estimation algorithms explicitly designed for off-grid delays are essential.

This chapter focuses on estimating off-grid channel delays and determining the number of paths in multipath environments. Leveraging recent developments in sparse signal reconstruction and off-grid parameter refinement, we propose a robust approach for jointly estimating multipath components and their fractional delays. The proposed methods integrate grid-based sparse Bayesian learning (SBL) with iterative off-grid refinements utilizing first- and second-order Taylor expansions, ensuring high precision even under low-SNR conditions.

By enhancing the accuracy of off-grid delay estimation, our techniques facilitate precise PDP reconstruction, significantly benefiting subsequent ranging and distance estimation algorithms. This research establishes a solid foundation for future investigations extending off-grid estimation frameworks to more complex scenarios, such as joint delay and Doppler estimation, where simultaneous temporal and frequency resolutions are required.

4.2 System Model

We consider an OFDM system comprising K subcarriers and a cyclic prefix (CP) sufficiently long to transform linear convolution between the transmitted signal and the channel into a circular convolution. The wireless channel is characterized by L propagation paths, each with complex gain $\alpha_l \in \mathbb{C}$ and non-integer delay $\tau_l \in [0, T)$, where $T = KT_s$ is the OFDM symbol duration and T_s is the sampling interval.

To model fractional delays accurately, we employ sinc interpolation. Thus, the discretetime approximation of the continuous-time channel impulse response is:

$$h[n] = \sum_{l=1}^{L} \alpha_l \cdot \operatorname{sinc}\left(n - \frac{\tau_l}{T_s}\right),\tag{4.1}$$

where $\operatorname{sinc}(x) = \frac{\sin(\pi x)}{\pi x}$. Practically, although the sinc function extends infinitely, we consider a finite set of samples for each OFDM symbol:

$$h[n], \quad n = 0, \dots, K - 1.$$
 (4.2)

This truncation ensures compatibility with the K-point discrete Fourier transform (DFT) at the receiver.

The CP facilitates circular convolution, allowing frequency-domain channel responses through the DFT of the truncated impulse response:

$$H[k] = \sum_{n=0}^{K-1} h[n] \cdot e^{-j\frac{2\pi kn}{K}}.$$
(4.3)

Substituting h[n], we have:

$$H[k] = \sum_{l=1}^{L} \alpha_l \sum_{n=0}^{K-1} \operatorname{sinc}\left(n - \frac{\tau_l}{T_s}\right) e^{-j\frac{2\pi kn}{K}}.$$
 (4.4)

This expression indicates that each frequency-domain channel coefficient is composed of superimposed sinc-shaped frequency responses, each weighted by path gain and shifted by fractional delays.

In practice, the frequency-domain channel coefficients H[k] are estimated using pilot symbols embedded within the OFDM symbols. Let $\mathcal{P} \subseteq \{0, \dots, K-1\}$ denote the set of pilot subcarrier indices.

At each pilot subcarrier $k \in \mathcal{P}$, the received signal is expressed as:

$$y[k] = H[k] \cdot x[k] + w[k],$$
 (4.5)

where x[k] is the known pilot symbol, and w[k] is additive noise. Normalizing by x[k], the channel response becomes:

$$\tilde{y}[k] = \frac{y[k]}{x[k]} = H[k] + \tilde{w}[k],$$
(4.6)

where $\tilde{w}[k] = \frac{w[k]}{x[k]}$ is the scaled noise. Stacking these normalized observations yields:

$$\mathbf{y} = [\tilde{y}[k_1], \dots, \tilde{y}[k_{|\mathcal{P}|}]]^T, \tag{4.7}$$

with noise vector:

$$\mathbf{v} = [\tilde{w}[k_1], \dots, \tilde{w}[k_{|\mathcal{P}|}]]^T. \tag{4.8}$$

Sparse Representation and Delay Dictionary Model

Each frequency-domain channel coefficient H[k] can be represented as a sum of contributions from propagation paths. Define the frequency response contribution of path l at subcarrier k as:

$$\phi_k(\tau_l) = \sum_{n=0}^{K-1} \operatorname{sinc}\left(n - \frac{\tau_l}{T_s}\right) e^{-j\frac{2\pi kn}{K}}.$$
(4.9)

Combining observations across all pilot subcarriers, the model becomes:

$$\mathbf{y} = \mathbf{\Phi}(\boldsymbol{\tau})\mathbf{h} + \mathbf{v},\tag{4.10}$$

where:

- $\mathbf{h} = [\alpha_1, \dots, \alpha_L]^T \in \mathbb{C}^L$ is the vector of path gains,
- $\boldsymbol{\tau} = [\tau_1, \dots, \tau_L]^T$ is the vector of path delays,
- ullet v represents the normalized noise vector,
- $\Phi(\tau) \in \mathbb{C}^{|\mathcal{P}| \times L}$ is the delay-dependent dictionary matrix with entries:

$$\mathbf{\Phi}_{k,l}(\boldsymbol{\tau}) = \sum_{n=0}^{K-1} \operatorname{sinc}\left(n - \frac{\tau_l}{T_s}\right) e^{-j\frac{2\pi kn}{K}}, \quad k \in \mathcal{P}.$$
 (4.11)

This formulation clearly links pilot-normalized observations to channel parameters, laying a solid foundation for accurate channel estimation and sparse recovery methods.

Grid-based Approximation and Off-grid Modeling

Let $\tilde{\tau} = \{\tilde{\tau}_1, \dots, \tilde{\tau}_N\}$ be a uniform delay grid spanning the interval $[0, \tau_{\text{max}})$, with grid spacing $\Delta = \tau_{\text{max}}/N$. Typically, we have $K < N_p \ll N$ where N_p is the length of Cycle Prefix (CP). Each true delay τ_k is assumed close to some grid point $\tilde{\tau}_{n_k}$. We define the offset as:

$$\beta_n = \tau_k - \tilde{\tau}_{n_k}, \quad \beta_n \in \left(-\frac{\Delta}{2}, \frac{\Delta}{2}\right),$$

$$(4.12)$$

where $n = n_k$ indicates the nearest grid index to τ_k .

To capture off-grid effects, we apply a second-order Taylor expansion to the k-th delay steering vector of matrix $\Phi(\tau)$:

$$\phi(\tau_k) \approx \mathbf{a}(\tilde{\tau}_{n_k}) + \mathbf{b}(\tilde{\tau}_{n_k})\beta_n + \frac{1}{2}\mathbf{c}(\tilde{\tau}_{n_k})\beta_n^2, \tag{4.13}$$

with:

$$\mathbf{a}(\tilde{\tau}_{n_k}) = \boldsymbol{\phi}(\tilde{\tau}_{n_k}),$$

$$\mathbf{b}(\tilde{\tau}_{n_k}) = \frac{\partial \boldsymbol{\phi}(\tau)}{\partial \tau} \Big|_{\tau = \tilde{\tau}_{n_k}},$$

$$\mathbf{c}(\tilde{\tau}_{n_k}) = \frac{\partial^2 \boldsymbol{\phi}(\tau)}{\partial \tau^2} \Big|_{\tau = \tilde{\tau}_{n_k}}.$$

$$(4.14)$$

We define dictionary matrices for convenience:

$$\mathbf{A} = [\mathbf{a}(\tilde{\tau}_1), \dots, \mathbf{a}(\tilde{\tau}_N)], \quad \mathbf{B} = [\mathbf{b}(\tilde{\tau}_1), \dots, \mathbf{b}(\tilde{\tau}_N)], \quad \mathbf{C} = [\mathbf{c}(\tilde{\tau}_1), \dots, \mathbf{c}(\tilde{\tau}_N)]. \tag{4.15}$$

Let $\boldsymbol{x} \in \mathbb{C}^N$ be a sparse vector such that:

$$x_n = h_k$$
, if $n = n_k$; $x_n = 0$, otherwise. (4.16)

Absorbing approximation errors into the noise term, the measurement model becomes:

$$\mathbf{y} = \left[\mathbf{A} + \mathbf{B} \operatorname{diag}(\boldsymbol{\beta}) + \frac{1}{2} \mathbf{C} \operatorname{diag}(\boldsymbol{\beta})^{2} \right] \boldsymbol{x} + \mathbf{v}. \tag{4.17}$$

This formulation facilitates simultaneous recovery of the sparse coefficient vector \boldsymbol{x} , indicating active delay bins, and the off-grid deviations $\boldsymbol{\beta}$, thereby refining delay estimates beyond the grid resolution. Setting \mathbf{C} to zero simplifies (4.17) to a first-order off-grid approximation.

Estimating continuous delays τ requires determining both the sparse support in x and the corresponding offsets β . This paper employs a Bayesian inference framework and proposes an iterative algorithm for jointly estimating these parameters, as detailed in the subsequent section.

4.3 Off-Grid Sparse Bayesian Inference

4.3.1 Sparse Bayesian Formulation

Under the assumption of white (circular symmetric) complex Gaussian noise, we have

$$p(\mathbf{v}|\lambda) = \mathcal{CN}(\mathbf{v}|\mathbf{0}, \lambda \mathbf{I}_{N_n}), \tag{4.18}$$

where λ denotes the noise variance. Then the likelihood becomes

$$p(\mathbf{y}|\mathbf{x}, \boldsymbol{\beta}) = \mathcal{CN}(\mathbf{y}|[\mathbf{A} + \mathbf{B}\operatorname{diag}(\boldsymbol{\beta}) + \frac{1}{2}\mathbf{C}\operatorname{diag}(\boldsymbol{\beta})^{2}]\mathbf{x}, \lambda \mathbf{I}_{N_{p}}). \tag{4.19}$$

We assume that the noise variance λ is unknown and will be estimated during inference. In Sparse Bayesian Learning (SBL), the unknown coefficients $\mathbf{x} \in \mathbb{C}^N$ are modeled as decorrelated zero-mean complex Gaussian variables:

$$p(\mathbf{x}|\boldsymbol{\gamma}) = \prod_{n=1}^{N} \mathcal{CN}(x_n|0,\gamma_n), \tag{4.20}$$

where $\boldsymbol{\gamma} = [\gamma_1, \cdots, \gamma_N]^T$ contains the nonnegative hyperparameters that control the sparsity of \mathbf{x} . When $\gamma_n = 0$, the corresponding x_n is forced to zero. Due to automatic relevance determination (ARD), many γ_n naturally converge to zero. Here, we treat $\boldsymbol{\gamma}$ as deterministic but unknown and impose a non-informative prior on it.

The off-grid delay biases β are assumed to follow a uniform prior:

$$p(\boldsymbol{\beta}) = \prod_{n=1}^{N} p(\beta_n) = U\left(\left(-\frac{\Delta}{2}, \frac{\Delta}{2}\right)^N\right), \tag{4.21}$$

where Δ is the uniform grid spacing in the delay domain. This reflects the assumption that the true delays lie near the grid, but not exactly on it.

The joint posterior distribution over the unknowns is therefore:

$$p(\mathbf{x}, \mathbf{y}, \boldsymbol{\beta} | \boldsymbol{\gamma}) = p(\mathbf{x} | \boldsymbol{\gamma}) \cdot p(\mathbf{y} | \mathbf{x}, \boldsymbol{\beta}) \cdot p(\boldsymbol{\beta}), \tag{4.22}$$

with each term defined in (4.19), (4.20), and (4.21). This captures the hierarchical Bayesian formulation for off-grid delay estimation.

4.3.2 Stein's Unbiased Risk Estimator for Estimating γ

We estimate γ and β in an alternating fashion. Assuming a current estimate $\hat{\beta}$, we define:

$$\mathbf{H}(\hat{\boldsymbol{\beta}}) = \mathbf{A} + \mathbf{B}\operatorname{diag}(\hat{\boldsymbol{\beta}}) + \frac{1}{2}\mathbf{C}\operatorname{diag}(\hat{\boldsymbol{\beta}})^{2}, \tag{4.23}$$

and rewrite the model as:

$$\mathbf{y} = \mathbf{H}(\hat{\boldsymbol{\beta}}) \,\mathbf{x} + \mathbf{v}. \tag{4.24}$$

The posterior of \mathbf{x} is Gaussian:

$$p(\mathbf{x}|\mathbf{y}) = \mathcal{CN}(\mathbf{x}|\boldsymbol{\mu}, \boldsymbol{\Sigma}),$$
 (4.25)

with:

$$\Gamma = \operatorname{diag}(\gamma),$$

$$\mathbf{R} = \mathbf{H}(\hat{\boldsymbol{\beta}}) \Gamma \mathbf{H}(\hat{\boldsymbol{\beta}})^{H} + \lambda \mathbf{I}_{N_{p}},$$

$$\boldsymbol{\mu} = \Gamma \mathbf{H}(\hat{\boldsymbol{\beta}})^{H} \mathbf{R}^{-1} \mathbf{y},$$

$$\boldsymbol{\Sigma} = \Gamma - \Gamma \mathbf{H}(\hat{\boldsymbol{\beta}})^{H} \mathbf{R}^{-1} \mathbf{H}(\hat{\boldsymbol{\beta}}) \Gamma.$$
(4.26)

Following the Component-Wise Conditionally Unbiased Linear Minimum Mean-Square Error (CWCU-LMMSE) estimator [106] framework, the instantaneous estimate of x_n is:

$$\hat{x}_n(0) = x_n + \tilde{x}_n(0), \tag{4.27}$$

where $\tilde{x}_n(0)$ has variance $\sigma^2_{\tilde{x}_n(0)}$.

The CWCU-LMMSE estimate of x_n is:

$$\hat{x}_n(0) = \frac{\mathbf{H}_n^H \left(\sum_{j \neq n} \hat{\gamma}_j \mathbf{H}_j \mathbf{H}_j^H + \lambda \mathbf{I} \right)^{-1} \mathbf{y}}{\mathbf{H}_n^H \left(\sum_{j \neq n} \hat{\gamma}_j \mathbf{H}_j \mathbf{H}_j^H + \lambda \mathbf{I} \right)^{-1} \mathbf{H}_n},$$
(4.28a)

$$\sigma_{\tilde{x}_n(0)}^2 = \left[\mathbf{H}_n^H \left(\sum_{j \neq n} \hat{\gamma}_j \mathbf{H}_j \mathbf{H}_j^H + \lambda \mathbf{I} \right)^{-1} \mathbf{H}_n \right]^{-1}.$$
 (4.28b)

The posterior mean in SBL is:

$$\hat{x}_n = \frac{\gamma_n}{\gamma_n + \sigma_{\tilde{x}_n(0)}^2} \hat{x}_n(0). \tag{4.29}$$

Applying Stein's unbiased risk estimation (SURE), we obtain:

$$SURE_{x_n}(\gamma_n) = \left(\frac{\sigma_{\tilde{x}_n(0)}^2}{\gamma_n + \sigma_{\tilde{x}_n(0)}^2}\right)^2 |\hat{x}_n(0)|^2 + 2\frac{\sigma_{\tilde{x}_n(0)}^2 \gamma_n}{\gamma_n + \sigma_{\tilde{x}_n(0)}^2},\tag{4.30}$$

which is minimized when:

$$\hat{\gamma}_n = \max\left(|\hat{x}_n(0)|^2 - \sigma_{\tilde{x}_n(0)}^2, 0\right). \tag{4.31}$$

4.3.3 Expectation Propagation for Estimating β

To estimate β , we consider the posterior:

$$p(\boldsymbol{\beta}|\mathbf{y},\hat{\boldsymbol{\gamma}}) = \frac{p(\mathbf{y}|\boldsymbol{\beta},\hat{\boldsymbol{\gamma}})p(\boldsymbol{\beta})}{\int p(\mathbf{y}|\boldsymbol{\beta},\hat{\boldsymbol{\gamma}})p(\boldsymbol{\beta})d\boldsymbol{\beta}},$$
(4.32)

where

$$p(\mathbf{y}|\boldsymbol{\beta}, \hat{\boldsymbol{\gamma}}) = \mathcal{CN}(\mathbf{y}|\mathbf{0}, \mathbf{R}(\boldsymbol{\beta})),$$
 (4.33)

$$\mathbf{R}(\boldsymbol{\beta}) = \mathbf{H}(\boldsymbol{\beta})\operatorname{diag}(\hat{\boldsymbol{\gamma}})\mathbf{H}^{H}(\boldsymbol{\beta}) + \lambda \mathbf{I}.$$
 (4.34)

This posterior is intractable due to the high-dimensional integral. Thus, we propose an EP-like approximation:

$$p(\boldsymbol{\beta}|\mathbf{y}) \approx q(\boldsymbol{\beta}) = \frac{p(\mathbf{y}|\boldsymbol{\beta}) \prod_{n=1}^{N} \delta(\beta_n - \hat{\beta}_n)}{\int p(\mathbf{y}|\boldsymbol{\beta}) \prod_{n=1}^{N} \delta(\beta_n - \hat{\beta}_n) d\boldsymbol{\beta}}.$$
 (4.35)

To update $\hat{\beta}_n$, we define:

$$\psi(\mathbf{y}|\beta_n) = \int p(\mathbf{y}|\boldsymbol{\beta}) \prod_{i \neq n} \delta(\beta_i - \hat{\beta}_i) d\boldsymbol{\beta}_{\bar{n}}, \tag{4.36}$$

where, $d\beta_{\bar{n}}$ denotes integration with respect to all components of β except β_n , i.e., $d\beta_{\bar{n}} = \prod_{i \neq n} d\beta_i$. The Dirac factors $\prod_{i \neq n} \delta(\beta_i - \hat{\beta}_i)$ fix all coordinates β_i ($i \neq n$) to their current estimates $\hat{\beta}_i$, so that $\psi(\mathbf{y}|\beta_n)$ can be interpreted as the likelihood function of β_n when the remaining coordinates are held constant.

Then compute:

$$\hat{\beta}_n = \frac{\int \beta_n \psi(\mathbf{y}|\beta_n) p(\beta_n) d\beta_n}{\int \psi(\mathbf{y}|\beta_n) p(\beta_n) d\beta_n}.$$
(4.37)

For a Gaussian likelihood,

$$\psi(\mathbf{y}|\beta_n) = \frac{1}{\pi^{N_p} \det(\mathbf{\Xi}_{\bar{n}})} \exp\left(-\mathbf{y}^H \mathbf{\Xi}_{\bar{n}}^{-1} \mathbf{y}\right), \tag{4.38}$$

with:

$$\mathbf{\Xi}_{\bar{n}} = \mathbf{H}(\hat{\boldsymbol{\beta}}_{\bar{n}}) + \beta_n \mathbf{B}_n + \frac{1}{2} \beta_n^2 \mathbf{C}_n. \tag{4.39}$$

Finally, the update is:

$$\hat{\beta}_n = \frac{\int_{-\Delta/2}^{\Delta/2} \beta_n \cdot \frac{1}{\det(\mathbf{\Xi}_{\bar{n}})} e^{-\mathbf{y}^H \mathbf{\Xi}_{\bar{n}}^{-1} \mathbf{y}} d\beta_n}{\int_{-\Delta/2}^{\Delta/2} \frac{1}{\det(\mathbf{\Xi}_{\bar{n}})} e^{-\mathbf{y}^H \mathbf{\Xi}_{\bar{n}}^{-1} \mathbf{y}} d\beta_n}.$$
(4.40)

Even though (4.40) lacks an analytic form, it can be computed numerically as a one dimension integration using appropriate numerical tools.

4.3.4 Noise Variance λ Estimation

Once $\hat{\boldsymbol{\beta}}$ and $\hat{\boldsymbol{\gamma}}$ have been estimated, we construct the matrix $\mathbf{H}(\hat{\boldsymbol{\beta}})$ by selecting the columns corresponding to the nonzero entries in $\hat{\boldsymbol{\gamma}}$, and form a reduced sensing matrix $\hat{\boldsymbol{\Phi}}$. The sparse vector \mathbf{x} is then estimated using the least squares estimator (LSE):

$$\hat{\mathbf{x}} = (\hat{\mathbf{\Phi}}^H \hat{\mathbf{\Phi}})^{-1} \hat{\mathbf{\Phi}}^H \mathbf{y}. \tag{4.41}$$

The noise variance hyperparameter λ is updated via:

$$\hat{\lambda} = \frac{\|\mathbf{y} - \hat{\mathbf{\Phi}}\hat{\mathbf{x}}\|_2^2}{N_p}.$$
(4.42)

As previously discussed, we treat \mathbf{x} as deterministic apart from its sparsity structure. Estimating λ while simultaneously learning $\boldsymbol{\gamma}$ may introduce statistical bias. Therefore, further investigation is warranted to analyze the robustness and impact of this estimation, particularly in the context of sparse Bayesian learning applied to delay estimation.

4.3.5 SURE-SBL-EP Delay Estimation Algorithm

The complete iterative procedure for estimating delay components via the SURE-SBL-EP framework is summarized in Algorithm 4.1. The initialization of hyperparameters used in the simulations is provided in Section 4.4.

4.4 Numerical Simulation

To evaluate the performance of the proposed delay estimation algorithms, extensive simulations were conducted under various signal-to-noise ratio (SNR) conditions. In each Monte Carlo (MC) trial, a random multipath channel was generated using the following parameters:

Parameter	Value
Number of subcarriers, K	64
Cyclic prefix (CP) ratio	$0.25 \ (N_{\rm cp} = 16)$
Sampling period, T_s	$\frac{1}{0.960\mathrm{MHz}}$
CP duration, $T_{\rm cp}$	$N_{ m cp}T_s$
Number of pilots	16 (uniform comb pattern)
Number of paths, L	3 (with minimum delay spacing $0.1 T_{cp}$)
Pilots	BPSK

Table 4.1: Fractional Delay Recovery Simulation Parameters

For each Monte Carlo realization, path delays and complex gains were generated randomly. The path delays were intentionally set as non-integer multiples of the sampling period to emphasize the challenge of off-grid delay estimation. The complex gains were independently drawn from a circularly symmetric complex Gaussian distribution to reflect realistic fading characteristics.

The simulations compared five different delay estimation algorithms. First, the Sparse Bayesian Learning (SBL) algorithm was tested using a fixed delay grid with N = 640. To

Algorithm 4.1 Delay Estimation via SURE-SBL-EP

```
1: Input: Normalized received vector \mathbf{y}, dictionary size N, sparsity level K, thresholds
       \epsilon_1, \, \epsilon_2, \, \epsilon_3
  2: Output: Estimated delays \{\hat{\tau}_k\}_{k=1}^K
 3: Initialize: \gamma^{(1)} \leftarrow \mathbf{1}_N, \beta^{(1)} \leftarrow \mathbf{0}_N, \zeta \leftarrow 1, delay grid \tilde{\tau}, noise level estimate \hat{\lambda}^{(1)} \leftarrow 0.1
  4: Compute dictionary matrices A, B, and C based on \tilde{\tau}
  5: repeat
  6:
              \zeta \leftarrow \zeta + 1
              repeat
                                                                                                                                                             \triangleright Update \gamma
  7:
                     for n = 1 to N do
  8:
                            Update \hat{x}_n(0) and \sigma^2_{\tilde{x}_n(0)} using CWCU-LMMSE
  9:
                            Update \gamma_n^{(\zeta)} using SURE rule in Eq. (4.31)
10:
              \begin{array}{c} \mathbf{end} \ \mathbf{for} \\ \mathbf{until} \ \frac{\|\boldsymbol{\gamma}^{(\zeta)} - \boldsymbol{\gamma}^{(\zeta-1)}\|^2}{\|\boldsymbol{\gamma}^{(\zeta)}\|^2} < \epsilon_1 \end{array}
11:
12:
              Retain top-K entries in \gamma^{(\zeta)}, zero out the rest
13:
                                                                                                                                                             \triangleright Update \beta
14:
              repeat
                     for n = 1 to N do
15:
                            if \gamma_n^{(\zeta)} \neq 0 then
Update \hat{\beta}_n^{(\zeta)} using Eq. (4.40)
16:
17:
                            else
18:
                                   Set \hat{\beta}_n^{(\zeta)} \leftarrow 0
19:
                            end if
20:
              \begin{array}{c} \text{end for} \\ \text{until } \frac{\|\boldsymbol{\beta}^{(\zeta)} - \boldsymbol{\beta}^{(\zeta-1)}\|^2}{\|\boldsymbol{\beta}^{(\zeta)}\|^2} < \epsilon_2 \end{array}
21:
22:
              Update noise variance \hat{\lambda}^{(\zeta)} via Eq. (4.42)
23:
      \text{until } \frac{\|\hat{\lambda}^{(\zeta)} - \hat{\lambda}^{(\zeta-1)}\|}{\|\hat{\lambda}^{(\zeta)}\|^2} < \epsilon_3
25: Return: Estimated delays \{\hat{\tau}_k\}_{k=1}^K corresponding to non-zero entries in \boldsymbol{\beta}^{(\zeta)}
```

address off-grid effects, two refinement approaches based on Taylor expansions were also evaluated: the first-order Taylor refinement, which iteratively improves the delay estimates, and the second-order Taylor refinement, which further enhances the off-grid delay resolution. For comparison, the classical Orthogonal Matching Pursuit (OMP) method, also using a fixed delay grid, was included. Additionally, the Approximate Message Passing (AMP) algorithm was incorporated, which adaptively solves the LASSO problem for delay estimation.

To visualize the off-grid delay estimation capabilities, a single MC realization was performed at two representative SNR levels: 0 dB and 20 dB. For each SNR, the estimated delay impulses were compared to the true impulses to highlight how well each method captures the true (non-integer) delays. Once the delay support was identified, the complex gains were refined using least-squares fitting for all methods.

Figures 4.1a and 4.1b illustrate the reconstructed sparse delay impulses at SNR levels of 0 dB and 20 dB, respectively. These results demonstrate that the refinement-based methods, particularly the second-order Taylor refinement, accurately capture the off-grid delays even in low-SNR scenarios.

To assess the average performance of each algorithm, extensive MC simulations were conducted. For each SNR level from 0 dB to 20 dB in 5 dB increments, 10⁴ independent

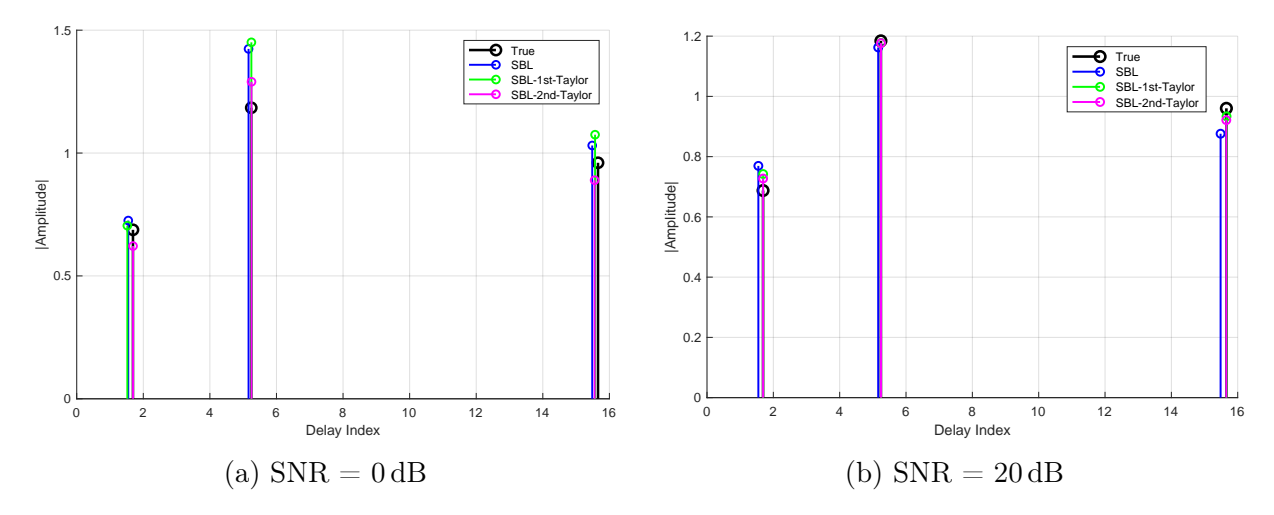


Figure 4.1: Reconstructed delay impulses for different SNRs in a single MC realization.

MC realizations were performed. The root mean square error (RMSE) of the estimated delays was computed and averaged across all trials.

Figure 4.2 shows the RMSE versus SNR for all methods. The second-order Taylor refinement method (*EP-SURE-SBL-2nd*) consistently achieves the lowest RMSE, highlighting its superior delay estimation accuracy across the entire SNR range. Notably, the performance gap between the methods widens at higher SNRs, underscoring the benefits of the proposed refined off-grid delay estimation techniques. These findings confirm the effectiveness of the proposed second-order Taylor refinement method for robust off-grid delay estimation in noisy environments.

4.5 Conclusions

In this chapter, we proposed the EP-SURE-SBL algorithm for estimating the delay and the number of paths in multipath channels. The algorithm divides the estimation problem into two key components: grid-on delay estimation and off-grid error correction. The grid-on estimation leverages sparse Bayesian learning to capture the sparse multipath structure, while the variance hyperparameter is estimated using Stein's Unbiased Risk Estimate (SURE), avoiding reliance on traditional Expectation-Maximization (EM) methods. For the off-grid error correction, we approximate the Minimum Mean Square Error (MMSE) bias through Expectation Propagation (EP), enabling refined delay estimation beyond the grid resolution. Extensive simulations have confirmed the feasibility and accuracy of the proposed approach, showing that it can reliably estimate the true delays and path gains, even in the presence of noise. Future work will focus on extending the approach to jointly estimate delay and Doppler shift, addressing scenarios with doubly off-grid effects. Additionally, this chapter lays the foundation for subsequent distance estimation tasks by introducing a robust framework for estimating the path number and delays, which are critical for reconstructing the power delay profile (PDP).

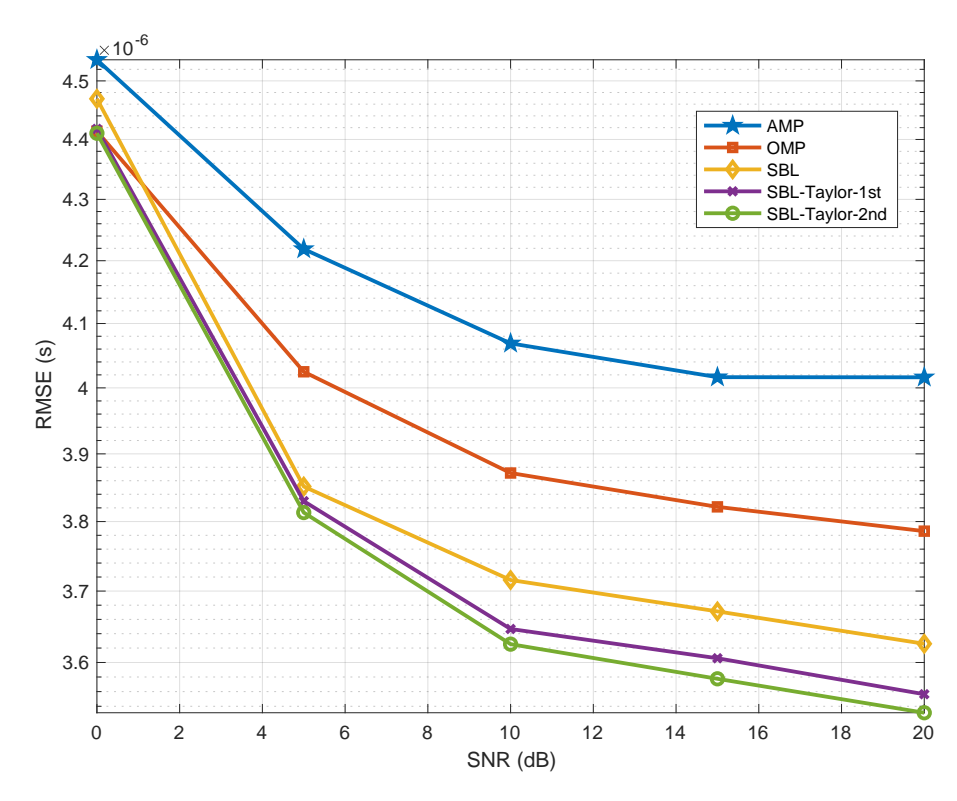


Figure 4.2: RMSE of estimated delays versus SNR, averaged over 10^4 MC realizations. The second-order Taylor refinement method achieves the best performance across all SNRs.

Chapter 5

Multipath Component Power Delay Profile Based Ranging

5.1 Introduction

In our work, we propose a novel multipath component power delay profile (MPCPDP)-based ranging method that exploits the rich multipath structure of the wireless channel. Unlike RSS-based methods that summarize the power delay profile (PDP) into a single metric, our approach leverages the evolution of attenuation across the entire delay spread. Specifically, we model the attenuation of each multipath component (MPC) using a Nakagami-m fading model and establish a relationship between the model parameters and the propagation distance. This formulation allows for a more robust and accurate ranging estimation.

Nevertheless, the Nakagami-*m* fading model complicates the estimation process due to intractable integrals in the likelihood function. To address this challenge, we introduce the EM-ReVAMP algorithm, which combines the Expectation-Maximization (EM) framework with the Revisited Vector Approximate Message Passing (ReVAMP) algorithm. While the EM algorithm is well-suited for problems with latent variables, it often requires approximations of intractable posterior distributions. The ReVAMP algorithm fulfills this need by efficiently approximating the posterior distribution of the complex attenuation coefficients through approximate belief propagation, thus enabling practical implementation of the EM algorithm in our context [107]. Compared to the original VAMP algorithm [108], ReVAMP offers enhanced flexibility by providing individual variance estimates for each MPC, resulting in improved accuracy.

Our comprehensive simulations confirm the theoretical feasibility and effectiveness of the proposed MPCPDP-based ranging method and the EM-ReVAMP algorithm. However, it is important to note that experimental validation in real-world environments remains a future step. This raises potential concerns regarding the generalizability of the Nakagami-m model in diverse scenarios. Fortunately, the EM-ReVAMP algorithm's inherent versatility allows it to adapt to other statistical fading models with minor modifications [107], broadening its applicability.

Although our method may not match the precision of some state-of-the-art techniques that rely on additional measurements or specialized hardware, it significantly outperforms RSS-based ranging methods in terms of accuracy while maintaining a low implementation cost. This makes our approach a practical alternative when additional hardware is unavailable.

The key contributions of this work are summarized as follows:

- We propose a novel MPCPDP-based ranging method that requires only the channel impulse response and models the statistical attenuation of each MPC.
- We introduce the EM-ReVAMP algorithm, a practical and robust approach for maximum likelihood estimation with hidden random variables and intractable posteriors.
- We validate the superior accuracy and robustness of our proposed method and algorithm through comprehensive simulations employing the Nakagami-m fading model.

The remainder of this chapter is organized as follows: Section 5.2 presents the system model, including the OFDM model, the Nakagami-m amplitude fading of MPCs, and the MPCPDP-based ranging estimation. Sections 5.3 and 5.4 detail the EM and ReVAMP algorithms, respectively. Section 5.5 describes the procedure for estimating the line-of-sight (LoS) distance using the EM-ReVAMP algorithm and derives the Cramér-Rao bound (CRB) for the special case where the Nakagami-m model reduces to Rayleigh fading. Section 5.6 showcases the simulation results, and Section 5.7 concludes with a discussion of our findings and directions for future research.

5.2 System model

OFDM model

The widely preferred modulation technique in communication networks is OFDM, which finds extensive application in 5G-NR [109]. In the OFDM model, the received baseband signal can be mathematically expressed as the convolution of the transmitted OFDM signal, denoted as s(t), and the channel impulse response, denoted as g(t). Additionally, complex additive white Gaussian noise, represented as v(t), is added to the received signal. This relationship can be represented as:

$$r(t) = s(t) * g(t) + v(t),$$
 (5.1)

where * denotes the convolution operation. After the received signal, r(t), is sampled at a rate of T_s , time and frequency synchronizations are performed prior to the N-point fast Fourier transform (FFT) operation. The output of the FFT, denoted as \mathbf{y} , can be written as:

$$\mathbf{y} = \mathbf{X}\mathbf{h} + \mathbf{v} \in \mathbb{C}^{N \times 1},\tag{5.2}$$

where **X** is an $N \times N$ diagonal matrix containing the transmitted symbols on its diagonal, **h** represents the channel frequency response (CFR) as a vector, and **v** is a vector of independently and identically distributed (i.i.d.) complex zero-mean Gaussian noise samples with equal variance σ_v^2 .

In the case of a block fading channel that remains constant over the duration of a packet, the channel impulse response (CIR) can be described as follows: [110]

$$g(t) = \sum_{l=0}^{L-1} a_l \delta(t - \kappa_l T_s), \qquad (5.3)$$

where $a_l \in \mathbb{C}$ and $\kappa_l T_s(\kappa_0 < \kappa_1 < ... < \kappa_{L-1}$ and $\kappa_l \in \mathcal{Z}^+$) represent the gain and delay of the l^{th} path, respectively, and $\delta(t)$ denotes the Kronecker delta function. Let

$$\mathbf{h} = [h_0, \ h_1, \ \dots, \ h_{N-1}]^T, \tag{5.4}$$

be the discrete CFR. Under the assumption that the sampling starts at t = 0, the n th element of \mathbf{h} can be written as [111]:

$$h_n = \sum_{l=0}^{L-1} a_l e^{-j\kappa_l \omega} \big|_{\omega = \frac{2\pi[n]_N}{N}},\tag{5.5}$$

where

$$[n]_N = \begin{cases} n, & n \le N/2 - 1, \\ n - N, & n \ge N/2 + 1. \end{cases}$$
 (5.6)

Therefore, we can present (5.5) as

$$\mathbf{h} = \mathbf{Ta} \in \mathbb{C}^{N \times 1} \tag{5.7}$$

where $\mathbf{a} \in \mathbb{C}^{L \times 1}$ is a vector filled with fading gains and $\mathbf{T} \in \mathbb{C}^{N \times L}$ is a transformation matrix that $T_{kl} = e^{-j\kappa_l \omega}|_{\omega = \frac{2\pi[k]_N}{N}}$.

Nakagami-m amplitude fading of MPCs

As discussed in the previous subsection, the received signal in OFDM can be represented as follows:

$$\mathbf{y} = \mathbf{X}\mathbf{T}\mathbf{a} + \mathbf{v} = \mathbf{h}\mathbf{a} + \mathbf{v}; \quad \mathbf{v} \sim \mathcal{CN}(0, \sigma_v^2 \mathbf{I}),$$
 (5.8)

where $\mathbf{a} \in \mathbb{C}^{L \times 1}$ denotes the complex attenuation coefficients (amplitude \mathbf{m} and phase $\boldsymbol{\phi}$). For each individual element $a_i = m_i e^{j\phi_i}$ of \mathbf{a} , we assume its magnitude m_i with a Nakagami-m distribution and phase ϕ_i with a uniform distribution. Therefore, the pdf of magnitude and phase can be expressed as follows:

$$p(m_i|\Omega_i) = \frac{2m^m m_i^{2m-1}}{\Gamma(m)\Omega_i^m} \exp\left[-\frac{m m_i^2}{\Omega_i}\right], m_i > 0, m \ge 0.5;$$
 (5.9a)

$$p(\phi_i) = \frac{1}{2\pi}, \quad \phi_i \in [0, 2\pi),$$
 (5.9b)

where $\Gamma(\cdot)$ denotes the gamma function m is the shape parameter of the Nakagami-m distribution and Ω_i is the average power intensity of path i. The shape parameter m controls the fading characteristics of the distribution. For lower values of m, the distribution resembles a Rayleigh distribution with a more rapid decay. As m increases, the distribution becomes more concentrated around its mean, resembling a more concentrated fading behavior. In practice, m is often estimated from channel measurements to accurately model the fading characteristics of the specific wireless channel. Referring to [112], the parameter Ω_i can be defined as:

$$\Omega_i(d_0) = P_t G_t G_r \left[\frac{\lambda}{4\pi (d_0 + c\tau_i)} \right]^n = G_0 (d_0 + c\tau_i)^{-n}, \tag{5.10}$$

in the given equation, several variables are defined as follows: P_t represents the transmitting power, G_t denotes the transmitting antenna amplification, λ is the wavelength of the electromagnetic wave, c is the velocity of light, n represents the propagation fading factor influenced by the environment, d_0 indicates the LoS distance, and τ_i indicates the propagation delay between the i-th path and the LoS path.

In (5.10), the term $P_tG_tG_r\left(\frac{\lambda}{4\pi}\right)^n$ can be considered as a constant, denoted as G_0 , which combines the effects of transmit power, antenna gains, wavelength, and path loss exponent. The propagation fading factor n plays a crucial role in determining the rate of signal attenuation with distance and can vary depending on the characteristics of the wireless channel and the environment in which the signals propagate. As the propagation distance $d_0 + c\tau_i$ increases, Ω_i decreases following an inverse power-law relationship $(d_0 + c\tau_i)^{-n}$. This allows us to estimate the specific range d_0 based on Ω_i when τ_i is known in a given environment.

Using the Jacobi determinant [113], we can obtain the pdf of complex fading coefficient a_i as follows:

$$p_{a_i}(a_i|\Omega_i(d_0)) = \frac{m^m |a_i|^{2m-2}}{\pi \Gamma(m) \Omega_i^m} \exp\left[-\frac{m |a_i|^2}{\Omega_i}\right].$$
 (5.11)

For simplicity, we denote $p_{a_i}(a_i|\Omega_i(d_0))$ by $p_{a_i}(a_i|d_0)$. Thus, the pdf of the collection **a** can be given as:

$$p_{\mathbf{a}}(\mathbf{a}|d_0) = \prod_{i=0}^{L-1} p_{a_i}(a_i|d_0).$$
 (5.12)

Before presenting the specific ranging estimation process, we assume the presence of a LoS path with an unknown distance d_0 , as well as measurable time delays between NLoS paths and the LoS path. While acknowledging the possibility of measurement and calibration biases, this paper does not focus on their effects. Consequently, we disregard these biases in the subsequent estimation process.

MPCPDP-based Ranging Estimation

Our objective is to estimate d_0 directly from \mathbf{y} . To achieve this, we will employ the maximum likelihood estimation (MLE) method, which transforms the problem into the following equation:

$$\hat{d}_0 = \arg\max_{d_0} \ell(d_0; \mathbf{y}) = \arg\max_{d_0} \ln \mathcal{L}(d_0; \mathbf{y}), \tag{5.13}$$

where $\mathcal{L}(\cdot)$ and $\ell(\cdot)$ represent the likelihood function and log-likelihood function, respectively.

Regarding the optimization problem (5.13), the likelihood function can be expressed as:

$$\mathcal{L}(d_0; \mathbf{y}) = p(\mathbf{y}|d_0) = \int p(\mathbf{a}, \mathbf{y}|d_0) d\mathbf{a} = \int p_{\mathbf{y}}(\mathbf{y}|\mathbf{a}) p_{\mathbf{a}}(\mathbf{a}|d_0) d\mathbf{a}.$$
 (5.14)

The pdf $p(\mathbf{y}|d_0)$ is crucial for estimating the LoS range d_0 based on the received signal \mathbf{y} in (5.13). However, solving the integral problem directly to acquire $p(\mathbf{y}|d_0)$ proves to be intractable, as finding an analytical form poses significant challenges. Furthermore, the latent variable \mathbf{a} is unobserved, and its distribution is unknown before reaching d_0 . To tackle these challenges, the EM-ReVAMP algorithm is introduced in Sections 5.3 and 5.4.

5.3 Review of Expectation Maximization (EM)

As we discussed before, in the linear mixing data model described by (5.8), we have a known measurement matrix $\mathbf{h} \in \mathbb{C}^{M \times L}$ and an non-identically and independent distributed (n.i.i.d.) prior $p_{\mathbf{a}}(\mathbf{a}|d_0) = \prod_{i=0}^{L-1} p_{a_i}(a_i|d_0)$ for the vector \mathbf{a} . Additionally, we consider a zero-mean Gaussian measurement noise $p(\mathbf{v}) = \mathcal{CN}(\mathbf{v}; \mathbf{0}_M, \mathbf{C}_{vv})$ with covariance matrix $\mathbf{C}_{vv} \in \mathcal{R}^{M \times M}$.

To address the optimization problem (5.13), the Expectation-Maximization (EM) algorithm [114] proves to be a suitable solution. This algorithm is effective for estimation problems involving latent variables, such as **a**, which are unobserved.

Using minorization maximization (MM) [115], we construct a more easily optimized lower bound of the log-likelihood function and iteratively approximate the optimal parameters by continuously optimizing this lower bound. Assuming at t th iteration that we have the estimated $d_0^{(t)}$, which allows us to write

$$\ell(d_0) - \ell(d_0^{(t)}) = \ln \int p_{\mathbf{y}}(\mathbf{y}|\mathbf{a}) p_{\mathbf{a}}(\mathbf{a}|d_0) d\mathbf{a} - \ln p(\mathbf{y}|d_0^{(t)})$$

$$= \ln \int \frac{p_{\mathbf{y}}(\mathbf{y}|\mathbf{a}) p_{\mathbf{a}}(\mathbf{a}|d_0)}{p(\mathbf{a}|\mathbf{y}, d_0^{(t)})} p(\mathbf{a}|\mathbf{y}, d_0^{(t)}) d\mathbf{a}$$

$$- \int p(\mathbf{a}|\mathbf{y}, d_0^{(t)}) \ln p(\mathbf{y}|d_0^{(t)}) d\mathbf{a},$$
(5.15)

where $p(\mathbf{a}|\mathbf{y}, d_0)$ is the posterior distribution of \mathbf{a} as which can be expressed by Bayes' rule as

$$p(\mathbf{a}|\mathbf{y}, d_0) = \frac{p_{\mathbf{y}}(\mathbf{y}|\mathbf{a})p_{\mathbf{a}}(\mathbf{a}|d_0)}{p(\mathbf{y}|d_0)} = \frac{p_{\mathbf{y}}(\mathbf{y}|\mathbf{a})p_{\mathbf{a}}(\mathbf{a}|d_0)}{\int p_{\mathbf{y}}(\mathbf{y}|\mathbf{a})p_{\mathbf{a}}(\mathbf{a}|d_0)d\mathbf{a}}.$$
 (5.16)

By using the concavity of $ln(\cdot)$ and Jensen's inequality, (5.15) becomes

$$\ell(d_0) - \ell(d_0^{(t)}) \ge \int p(\mathbf{a}|\mathbf{y}, d_0^{(t)}) \ln \frac{p_{\mathbf{y}}(\mathbf{y}|\mathbf{a})p_{\mathbf{a}}(\mathbf{a}|d_0)}{p(\mathbf{a}|\mathbf{y}, d_0^{(t)})} d\mathbf{a}$$

$$- \int p(\mathbf{a}|\mathbf{y}, d_0^{(t)}) \ln p(\mathbf{y}|d_0^{(t)}) d\mathbf{a}$$

$$= \int p(\mathbf{a}|\mathbf{y}, d_0^{(t)}) \ln \frac{p_{\mathbf{y}}(\mathbf{y}|\mathbf{a})p_{\mathbf{a}}(\mathbf{a}|d_0)}{p(\mathbf{y}|d_0^{(t)})p(\mathbf{a}|\mathbf{y}, d_0^{(t)})} d\mathbf{a}$$

$$= \mathbb{E}_{p(\mathbf{a}|\mathbf{y}, d_0^{(t)})} \left[\ln \frac{p_{\mathbf{y}}(\mathbf{y}|\mathbf{a})p_{\mathbf{a}}(\mathbf{a}|d_0)}{p(\mathbf{y}|d_0^{(t)})p(\mathbf{a}|\mathbf{y}, d_0^{(t)})} \right].$$
(5.17)

The lower bound $\mathcal{B}(d_0, d_0^{(t)})$ can be obtained as

$$\mathcal{B}(d_0, d_0^{(t)}) = \ell(d_0^{(t)}) + \mathbb{E}_{p(\mathbf{a}|\mathbf{y}, d_0^{(t)})} \left[\ln \frac{p_{\mathbf{y}}(\mathbf{y}|\mathbf{a})p_{\mathbf{a}}(\mathbf{a}|d_0)}{p(\mathbf{y}|d_0^{(t)})p(\mathbf{a}|\mathbf{y}, d_0^{(t)})} \right].$$
 (5.18)

The updated $d_0^{(t+1)}$ can be obtained from

$$d_0^{(t+1)} = \arg \max_{d_0} \mathcal{B}(d_0, d_0^{(t)})$$

$$= \arg \max_{d_0} \left\{ \ell(d_0^{(t)}) + \mathbb{E}_{p(\mathbf{a}|\mathbf{y}, d_0^{(t)})} \left[\ln \frac{p_{\mathbf{y}}(\mathbf{y}|\mathbf{a}) p_{\mathbf{a}}(\mathbf{a}|d_0)}{p(\mathbf{y}|d_0^{(t)}) p(\mathbf{a}|\mathbf{y}, d_0^{(t)})} \right] \right\}$$

$$= \arg \max_{d_0} \mathbb{E}_{p(\mathbf{a}|\mathbf{y}, d_0^{(t)})} \left[\ln p(\mathbf{y}, \mathbf{a}|d_0) \right].$$
(5.19)

At convergence we get $d_0^{(t)} = d_0^{(t+1)}$ which leads to the inequality becoming an equality:

$$\ln \int \frac{p_{\mathbf{y}}(\mathbf{y}|\mathbf{a})p_{\mathbf{a}}(\mathbf{a}|d_0^{(t+1)})}{p(\mathbf{a}|\mathbf{y},d_0^{(t)})}p(\mathbf{a}|\mathbf{y},d_0^{(t)})d\mathbf{a} = \ln p(\mathbf{y}|d_0^{(t+1)})$$

$$= \int p(\mathbf{a}|\mathbf{y},d_0^{(t)}) \ln \frac{p_{\mathbf{y}}(\mathbf{y}|\mathbf{a})p_{\mathbf{a}}(\mathbf{a}|d_0^{(t+1)})}{p(\mathbf{a}|\mathbf{y},d_0^{(t)})}d\mathbf{a}$$

$$\iff \ell(d_0^{(t+1)}) - \ell(d_0^{(t)}) = 0.$$
(5.20)

This proves that the EM algorithm can converge to the (local) optimal point. Moreover, the EM iteration can be specified as:

$$d_0^{(t+1)} = \arg \max_{d_0} \mathbb{E}_{p(\mathbf{a}|\mathbf{y}, d_0^{(t)})} \left[\ln p(\mathbf{a}, \mathbf{y}|d_0) \right]$$

$$= \arg \max_{d_0} \mathbb{E}_{p(\mathbf{a}|\mathbf{y}, d_0^{(t)})} \left[\ln p_{\mathbf{a}}(\mathbf{a}|d_0) + \ln p_{\mathbf{y}}(\mathbf{y}|\mathbf{a}) \right]$$

$$= \arg \max_{d_0} \mathbb{E}_{p(\mathbf{a}|\mathbf{y}, d_0^{(t)})} \left[\ln p_{\mathbf{a}}(\mathbf{a}|d_0) \right].$$
(5.21)

When considering the pdf of \mathbf{a} as described in (5.11) and (5.12), the EM iteration in (5.21) can be transformed as follows:

$$d_0^{(t+1)} = \arg \max_{d_0} \mathbb{E}_{p(\mathbf{a}|\mathbf{y}, d_0^{(t)})} \left[\sum_{i=0}^{L-1} (-\ln \Omega_i(d_0) - \frac{|a_i|^2}{\Omega_i(d_0)}) \right]$$

$$= \arg \min_{d_0} \sum_{i=0}^{L-1} \left[\ln \Omega_i(d_0) + \frac{\mathbb{E}_{p(\mathbf{a}|\mathbf{y}, d_0^{(t)})} [|a_i|^2]}{\Omega_i(d_0)} \right],$$
(5.22)

where $\Omega_i(d_0)$ was defined in (5.10). Here, as it is easy to find that both $\ln \Omega_i(d_0)$ and $\frac{1}{\Omega_i(d_0)}$ are convex functions w.r.t. d_0 . This characteristic ensures that the entire optimization function is convex, with only one global minimum point for d_0 .

However, in this scenario, the EM algorithm remains intractable because obtaining the posterior distribution $p(\mathbf{a}|\mathbf{y}, d_0^{(t)})$ is challenging due to the integration involved in (5.16). Therefore, it becomes crucial to develop an algorithm that approximates this posterior distribution with another tractable distribution. To achieve this goal, we propose an algorithm called Revisited Vector Approximate Message Passing (ReVAMP).

5.4 Revisited Vector Approximate Message Passing (Re-VAMP)

Our objective is to find a distribution $q(\mathbf{a})$ that approximates the posterior distribution $p(\mathbf{a}|\mathbf{y},d_0^{(t)})$ with minimal Kullback-Leibler divergence (KLD) between $p(\mathbf{a}|\mathbf{y},d_0^{(t)})$ and $q(\mathbf{a})$, where $d_0^{(t)}$ is given. Mathematically, we have:

$$\hat{q}(\mathbf{a}) = \arg\min_{q(\mathbf{a})} D_{KL} \left[p(\mathbf{a}|\mathbf{y}, d_0) || q(\mathbf{a}) \right]. \tag{5.23}$$

As seen in (5.22), the posterior distribution $p(\mathbf{a}|\mathbf{y}, d_0^{(t)})$ is used to get second order moment of each a_i . To accomplish this, we choose $q(\mathbf{a})$ as complex Gaussian distribution

 $\mathcal{CN}(\mathbf{a}; \mathbf{m}, \mathbf{C}_m)$, which turns to match the first-order and second-order moments of $q(\mathbf{a})$ and $p(\mathbf{a}|\mathbf{y}, d_0^{(t)})$ [116] if (5.23) is satisfied as follows:

$$\mathbb{E}_{q(\mathbf{a})}[\mathbf{a}] = \mathbb{E}_{p(\mathbf{a}|\mathbf{y},d_0^{(t)})}[\mathbf{a}],\tag{5.24a}$$

$$\mathbb{E}_{q(\mathbf{a})}[\mathbf{a}\mathbf{a}^H] = \mathbb{E}_{p(\mathbf{a}|\mathbf{y},d_0^{(t)})}[\mathbf{a}\mathbf{a}^H]. \tag{5.24b}$$

It ensures that even with an approximate distribution $q(\mathbf{a})$, the updated estimation value of $d_0^{(t+1)}$ in (5.22) will be the same as if it were calculated using the true posterior distribution $p(\mathbf{a}|\mathbf{y}, d_0^{(t)})$. However, solving equation (5.23) directly is computationally intractable. Therefore, we introduce the ReVAMP algorithm [107] as a solution.

To begin, we consider the factorization of the joint distribution as follows:

$$p(\mathbf{a}, \mathbf{y}|d_0) = p_{\mathbf{y}}(\mathbf{y}|\mathbf{a}) \prod_{i=0}^{L-1} p_{a_i}(a_i|d_0).$$
 (5.25)

This factorization can be represented as a factor graph, as shown in Fig. 5.1. In this graph, the variable nodes a_i , where i = 0, ..., L - 1, are connected to the factor nodes $p_{\mathbf{y}}(\mathbf{y}|\mathbf{a})$ and $p_{a_i}(a_i)$.

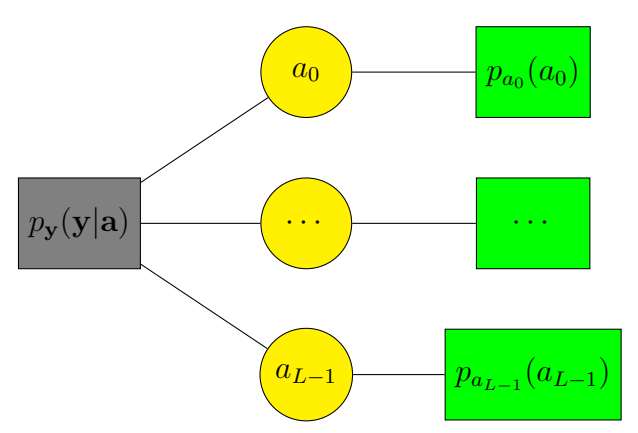


Figure 5.1: Factor graph of ReVAMP

Applying the sum-product rule [108], the message $\mu_{p_{\mathbf{y}}\to a_i}(a_i)$ passed from left factor node $p_{\mathbf{v}}(\mathbf{y}|\mathbf{a})$ to variable node a_i can be expressed as:

$$\mu_{p_{\mathbf{y}}\to a_i}(a_i) \propto \int p_{\mathbf{y}}(\mathbf{y}|\mathbf{a}) \prod_{j\neq i} \mu_{a_j\to p_{\mathbf{y}}}(a_j) da_j,$$
 (5.26)

where $\mu_{a_j \to p_y}(a_j)$ represents the message passed from variable node a_j to left factor node $p_y(\mathbf{y}|\mathbf{a})$. In addition, the message $\mu_{p_{a_i} \to a_i}(a_i)$ passed from right factor node p_{a_i} to variable node a_i can be represented as:

$$\mu_{p_{a_i} \to a_i}(a_i) = p_{a_i}(a_i). \tag{5.27}$$

At variable node a_i , the received messages $b_{sp}(a_i) \propto \mu_{p_{\mathbf{y}} \to a_i}(a_i) \mu_{p_{a_i} \to a_i}(a_i)$ are approximated with a complex Gaussian belief (approximated posterior) $b_{app}(a_i) = q(a_i) = \mathcal{CN}(a_i; \hat{a}_i, \tau_{a_i})$ by minimizing the KLD. This approximation is formulated as:

$$\hat{b}_{app} = \arg\min_{b_{app}} D_{KL}(b_{sp}(a_i)||b_{app}(a_i)).$$
 (5.28)

Analogous to the sum-product rule, the messages $\mu_{a_i \to p_y}(a_i)$ shown in (5.26) can be calculated by:

$$\mu_{a_i \to p_{\mathbf{y}}}(a_i) = \frac{b_{app}(a_i)}{\mu_{p_{\mathbf{y}} \to a_i}(a_i)}.$$
(5.29)

In the following, we will provide a detailed derivation of ReVAMP for the case where the measurement noise is assumed to be complex Gaussian.

5.4.1 Extrinsic to variable nodes

Assuming that at each iteration, the message $\mu_{a_i \to p_y}(a_i)$ passed from each variable node a_i to left factor node $p_y(y|a)$ is redefined as assumed prior $q_i(a_i)$ for all i = 0, ..., L - 1, where $q_i(a_i)$ is supposed to be a complex Gaussian distribution. In this case, we can prove by induction that they will remain complex Gaussian. Without loss of generality, let us define $q_i(a_i) = \mathcal{CN}(a_i; p_i, \tau_{p_i})$, where p_i and τ_{p_i} are the mean and variance of assumed prior of each a_i , respectively.

In this case, the joint distribution $\prod_{i=0}^{L-1} q_i(a_i)$ is equal to $\mathcal{CN}(\mathbf{a}; \mathbf{p}, \mathbf{D}_p)$, where $\mathbf{p} = [p_0 \dots p_{L-1}]^T$ and \mathbf{D}_p is a diagonal matrix whose *i*th entry is τ_{p_i} . The real posterior $p(\mathbf{a}|\mathbf{y})$ is approximated as $q(\mathbf{a}) = \mathcal{CN}(\mathbf{a}; \mathbf{m}, \mathbf{C}_m) \propto p(\mathbf{y}|\mathbf{a}) \prod_{i=0}^{L-1} q_i(a_i)$.

In addition, the message $\mu_{p_{\mathbf{y}}\to a_i}(a_i)$ is recalled as the extrinsic message $q_{\mathbf{y}}(a_i)$ for all $i=0,\ldots,L-1$, where $q_{\mathbf{y}}(a_i)$ is supposed to be a complex Gaussian distribution with mean r_i and variance τ_{r_i} . The extrinsic message for any variable node a_i is obtained by:

$$q_{\mathbf{y}}(a_{i}) \propto \frac{\int_{\mathbf{a}_{/i}} p(\mathbf{y}|\mathbf{a}) \mathcal{C} \mathcal{N}(\mathbf{a}; \mathbf{p}, \mathbf{D}_{p}) d\mathbf{a}_{/i}}{q_{i}(a_{i})} \times \frac{\int_{\mathbf{a}_{/i}} \mathcal{C} \mathcal{N}(\mathbf{a}; \mathbf{m}, \mathbf{C}_{m}) d\mathbf{a}_{/i}}{\mathcal{C} \mathcal{N}(a_{i}; p_{i}, \tau_{p_{i}})},$$

$$(5.30)$$

where $\mathbf{a}_{/i}$ represents a vector that is the same as \mathbf{a} except that it excludes the *i*-th entry, with

$$\mathbf{C}_m = \left(\mathbf{h}^H \mathbf{C}_{vv}^{-1} \mathbf{h} + \mathbf{D}_p^{-1}\right)^{-1}, \tag{5.31a}$$

$$\mathbf{m} = \mathbf{C}_m \left(\mathbf{h}^H \mathbf{C}_{vv}^{-1} \mathbf{y} + \mathbf{D}_v^{-1} \mathbf{p} \right). \tag{5.31b}$$

By following these steps, we can derive the extrinsic messages for the variable nodes, which play a crucial role in the algorithm for handling the complex Gaussian measurement noise. Additionally, we define $\boldsymbol{\tau}_m = \begin{bmatrix} \tau_{m_0} \dots \tau_{m_{L-1}} \end{bmatrix}^T = \operatorname{diag}(\mathbf{C}_m)$. Exploiting the properties of multivariate complex Gaussian distribution and (5.30), the extrinsic message $q_{\mathbf{y}}(a_i)$ is represented by the complex Gaussian distribution $\mathcal{CN}(a_i; r_i, \tau_{r_i})$ with

$$r_i = \frac{\tau_{p_i} m_i - \tau_{m_i} p_i}{\tau_{p_i} - \tau_{m_i}},\tag{5.32a}$$

$$\tau_{r_i} = \frac{\tau_{m_i} \tau_{p_i}}{\tau_{p_i} - \tau_{m_i}}.$$

$$(5.32b)$$

To approximate the belief $q(a_i) = \mathcal{CN}(a_i; \hat{a}_i, \tau_{a_i})$ at variable node a_i as a complex Gaussian distribution, we minimize the KLD as

$$\arg\min_{q(a_i)} D_{KL} \left[p(a_i) \mathcal{CN}(a_i; r_i, \tau_{r_i}) || q(a_i) \right]$$

$$\Leftrightarrow \arg\min_{\hat{a}_i, \tau_{a_i}} D_{KL} \left[p(a_i) \mathcal{CN}(a_i; r_i, \tau_{r_i}) || \mathcal{CN}(a_i; \hat{a}_i, \tau_{a_i}) \right].$$

$$(5.33)$$

Define the normalization factor as

$$Z_i(r_i, \tau_i) = \int p(a_i) \mathcal{CN}(a_i; r_i, \tau_{r_i}) da_i, \qquad (5.34)$$

then we obtain

$$\hat{a}_i = \frac{\int a_i p_{a_i}(a_i) \mathcal{CN}(a_i; r_i, \tau_{r_i}) da_i}{Z_i(r_i, \tau_i)}, \tag{5.35a}$$

$$\tau_{a_i} = \frac{\int |a_i - \hat{a}_i|^2 p_{a_i}(a_i) \mathcal{CN}(a_i; r_i, \tau_{r_i}) da_i}{Z_i(r_i, \tau_i)}.$$
 (5.35b)

It's worth noting that $p_{a_i}(a_i)$ in (5.35) is not restricted to the Nakagami-m propagation model prior of (5.11); it can accommodate other priors as well. When transitioning to a different statistical propagation model, minor adjustments of prior should be made to ensure the continued functionality of the ReVAMP algorithm.

5.4.2Passing the Approximation to the Factor Node

The assumed prior $q_i(a_i)$ can be expressed as the quotient of two complex Gaussian pdfs w.r.t. $q(a_i)$ and $q_y(a_i)$. This ensures that the resulting message distribution $q_i(a_i)$ remains complex Gaussian. Specifically, it is defined as:

$$q_i(a_i) = \mathcal{CN}(a_i; p_i, \tau_{p_i}) \propto \frac{\mathcal{CN}(a_i; \hat{a}_i, \tau_{a_i})}{\mathcal{CN}(a_i; r_i, \tau_{r_i})}.$$
 (5.36)

From (5.36), we can determine p_i and τ_{p_i} as follows:

$$p_i = \frac{\tau_{r_i} \hat{a}_i - \tau_{a_i} r_i}{\tau_{a_i} \tau_{r_i}},\tag{5.37a}$$

$$p_i = \frac{\tau_{r_i} \hat{a}_i - \tau_{a_i} r_i}{\tau_{a_i} \tau_{r_i}}, \qquad (5.37a)$$

$$\tau_{p_i} = \frac{\tau_{r_i} \tau_{a_i}}{\tau_{r_i} - \tau_{a_i}}. \qquad (5.37b)$$

It is worth noting that when using the sequential updating method, the complexity of the matrix inverse operation in (5.31) can be reduced by employing matrix inverse lemma. Let us denote the result of $\tau_{p_i}^{new}$ during the update messages of the a_i and define $\Delta_{p_i} = \frac{\tau_{p_i} - \tau_{p_i}^{new}}{\tau_{p_i} \tau_{p_i}^{new}}$. Moreover, we define $h_{\mathbf{C}}(\cdot)$ as the updating of the \mathbf{C}_m with the new value of $\tau_{p_i}^{new}$ as follows:

$$\mathbf{C}_{m}^{new} = h_{\mathbf{C}}(\mathbf{C}_{m}, \mathbf{e}_{i}, \Delta_{p_{i}}) = \left[\mathbf{C}_{m}^{-1} + \Delta_{p_{i}} \mathbf{e}_{i} \mathbf{e}_{i}^{T}\right]^{-1}$$

$$= \mathbf{C}_{m} - \mathbf{C}_{m} \mathbf{e}_{i} \left(1/\Delta_{p_{i}} + \mathbf{e}_{i}^{T} \mathbf{C}_{m} \mathbf{e}_{i}\right)^{-1} \mathbf{e}_{i}^{T} \mathbf{C}_{m}, \tag{5.38}$$

where \mathbf{e}_i is a unit vector with only the *i*-th entry set to 1. To handle the cycles, we define

The computation for updating \mathbf{m} in (5.31) can also be simplified with the same technique. We define $\Psi_{p_i} = \frac{p_i^{new}}{\tau_{p_i}^{new}} - \frac{p_i}{\tau_{p_i}}$ and denote $h_{\mathbf{m}}(\cdot)$ as its update equation as follows:

$$\mathbf{m}^{new} = h_{\mathbf{m}}(\mathbf{m}, \mathbf{C}_m, \mathbf{e}_i, \Delta_{p_i}, \Psi_{p_i})$$

$$= \mathbf{C}_m^{new}(\mathbf{h}^T \mathbf{C}_{vv}^{-1} \mathbf{y} + \mathbf{D}_p \mathbf{p} + \Psi_{p_i} \mathbf{e}_i)$$

$$= \mathbf{m} + \frac{\Psi_{p_i} - \Delta_{p_i} \mathbf{e}_i^T \mathbf{m}}{1 + \Delta_{p_i} \mathbf{e}_i^T \mathbf{C}_m \mathbf{e}_i} \mathbf{C}_m \mathbf{e}_i.$$
(5.39)

In summary, our algorithm iteratively computes messages from factor nodes to variable nodes and subsequently calculates messages from variable nodes back to factor nodes until convergence is achieved. The final approximation for $p(\mathbf{a}|\mathbf{y})$ is represented by $q(\mathbf{a}) = \mathcal{CN}(\mathbf{a}; \mathbf{m}, \mathbf{C}_m)$. Importantly, these update steps can be performed in parallel, yielding a similar algorithm to VAMP but with individual variance updates. By leveraging the matrix inverse lemma, the sequential update method maintains the same complexity as the parallel update method. Algorithm 5.1 delineates the detailed steps of this process.

5.4.3 Relation to Expectation Propagation (EP)

Algorithm 5.1 can be regarded as an EP algorithm by approximating the factorization in Equation (5.25) as follows:

$$p(\mathbf{a}|\mathbf{y}) \simeq q(\mathbf{a}) \propto p(\mathbf{a}, \mathbf{y}) \simeq p_{\mathbf{y}}(\mathbf{y}|\mathbf{a}) \prod_{i=0}^{L-1} q_i(a_i),$$
 (5.40)

where each $q_i(a_i)$ is a Gaussian distribution with mean p_i and variance τ_{p_i} . To further explore the EP connection, let us consider the optimization problem:

$$\arg\min_{q^{new}} D_{KL} \left[\frac{q(\mathbf{a})}{q_i(a_i)} p(a_i) || q^{new}(\mathbf{a}) \right]$$

$$= \arg\min_{q^{new}} \int_{a_i} \int_{a_{/i}} q(\mathbf{a}) da_{/i} \frac{p(a_i)}{q_i(a_i)} \ln \left[\frac{p(a_i)}{q^{new}(a_i)} \right] da_i.$$
(5.41)

Let us continue by introducing $h(a_i) = \int_{a_{/i}} [q(\mathbf{a})da_{/i}]/q_i(a_i)$ and then we can rewrite the optimization problem (5.41) as follows:

$$\arg\min_{q^{new}} \int_{a_i} h(a_i) p_{a_i}(a_i) \ln\left[\frac{h(a_i) p_{a_i}(a_i)}{h(a_i) q^{new}(a_i)}\right] da_i$$

$$= \arg\min_{q^{new}} D_{KL} \left[h(a_i) p_{a_i}(a_i) || h(a_i) q^{new}(a_i)\right].$$
(5.42)

In Algorithm 5.1, this marginal extrinsic is represented as a complex Gaussian distribution with mean r_i and variance τ_{r_i} . Lastly, the first equality in (5.41) holds because during the update for the *i*-th entry, for all $k \neq i$, the minimum is achieved when $q^{new}(a_k) = q(a_k)$.

5.4.4 Implementation Details

For the practical implementation with finite-dimensional \mathbf{h} , we suggest incorporating small enhancements to reVAMP, as discussed in Algorithm 5.1.

Firstly, it is advisable to clip the variances τ_{r_i} and $\tau_{p_i}^{new}$ within a positive interval $[\gamma_{min}, \gamma_{max}]$. Occasionally, the ReVAMP algorithm may yield negative values for τ_{r_i} and $\tau_{p_i}^{new}$ if not addressed. In our numerical results presented in Section 5.6, we utilized $\gamma_{min} = 10^{-10}$ and $\gamma_{max} = 10^{10}$.

Secondly, rather than mandating ReVAMP to complete several iterations, we propose stopping the iterations when the normalized difference $\|\mathbf{m}^{new} - \mathbf{m}\|/\|\mathbf{m}^{new}\|$ falls below a tolerance threshold ε . In Section 5.6, our numerical results employed $\varepsilon = 10^{-4}$.

Lastly, it's important to note that the ReVAMP algorithm requires the user to initialize \mathbf{p} , $\boldsymbol{\tau}_p$, \mathbf{m} and \mathbf{C}_m . Generally, all elements of $\boldsymbol{\tau}_p$ and all diagonal elements of \mathbf{C}_m must be positive; other initializations do not significantly affect the final result. In our experiments in Section 5.6, we set all elements in \mathbf{m} , \mathbf{p} , and $\boldsymbol{\tau}_p$ to be 1, and \mathbf{C}_m to be an identity matrix.

Algorithm 5.1 ReVAMP (Complex Gaussian measurement noise via sequential updating)

```
Ensure: m, C_m
Require: \mathbf{y}, \mathbf{h}, p_{\mathbf{a}}(\mathbf{a}), p(\mathbf{v})
  1: Initialize: \mathbf{m}, \mathbf{C}_m, \mathbf{p}, \boldsymbol{\tau}_p
  2: repeat
                 repeat [For each i = 0 \dots L - 1]
  3:
                         [Update the extrinsic]
  4:
                         \tau_m = \operatorname{diag}(\mathbf{C}_m)
  5:
                         r_i = \frac{\tau_{p_i} m_i - \tau_{m_i} p_i}{\tau_{p_i} - \tau_{m_i}}
\tau_{r_i} = \frac{\tau_{m_i} \tau_{p_i}}{\tau_{p_i} - \tau_{m_i}}
  6:
  7:
  8:
                          [Approximate the marginal posterior]
                         Update \hat{a}_i with (5.35a)
  9:
                         Update \tau_{a_i} with (5.35b)
10:
                         [Propagate the approximation back]
11:
                        Tropagate the a p_i^{new} = \frac{\tau_{r_i}\hat{a}_i - \tau_{a_i}r_i}{\tau_{r_i} - \tau_{a_i}}
\tau_{p_i}^{new} = \frac{\tau_{r_i}\hat{a}_i}{\tau_{r_i} - \tau_{a_i}}
\Delta_{p_i} = \frac{1}{\tau_{p_i}^{new}} - \frac{1}{\tau_{p_i}}
\Psi_{p_i} = \frac{p_i^{new}}{\tau_{p_i}^{new}} - \frac{p_i}{\tau_{p_i}}
12:
13:
14:
15:
                          [Update the posterior approximation]
16:
                         \mathbf{C}_m = h_{\mathbf{C}}(\mathbf{C}_m, \mathbf{e}_i, \Delta_{p_i})
17:
                         \mathbf{m} = h_{\mathbf{m}}(\mathbf{m}, \mathbf{C}_m, \mathbf{e}_i, \Delta_{p_i}, \Psi_{p_i})
18:
                 until All i-s have been updated
19:
                 \mathbf{p}=\mathbf{p}^{new}
20:
21:
                 oldsymbol{	au}_p = oldsymbol{	au}_p^{new}
22: until Convergence
```

5.5 Ranging estimation with Nakagami-m prior distribution

5.5.1 MPCPDP-based Ranging Method

We propose the EM-ReVAMP algorithm, outlined in Algorithm 5.2, for estimating d_0 . This algorithm utilizes ReVAMP sequentially at each step of the EM algorithm to obtain approximate second-order moments. Specifically, within the ReVAMP part, with given Ω_i in (5.10) w.r.t. \hat{d}_0 and prior distribution in (5.11), the marginal posterior approximation involves the calculation of \hat{a}_i and τ_{a_i} in (5.35a) and (5.35b) can be computed as follows:

$$\hat{a}_{i} = \frac{m\Omega_{i}r_{i}}{m\tau_{r_{i}} + \Omega_{i}} \frac{{}_{1}F_{1}(m+1;2; \frac{\Omega_{i}|r_{i}|^{2}}{m\tau_{r_{i}}^{2} + \tau_{r_{i}}\Omega_{i}})}{{}_{1}F_{1}(m;1; \frac{\Omega_{i}|r_{i}|^{2}}{m\tau_{r_{i}}^{2} + \tau_{r_{i}}\Omega_{i}})};$$
(5.43a)

$$\tau_{a_i} = \frac{m\Omega_i \tau_{r_i}}{m\tau_{r_i} + \Omega_i} \frac{{}_{1}F_{1}(m+1; 1; \frac{\Omega_i |r_i|^2}{m\tau_{r_i}^2 + \tau_{r_i}\Omega_i})}{{}_{1}F_{1}(m; 1; \frac{\Omega_i |r_i|^2}{m\tau_{r_i}^2 + \tau_{r_i}\Omega_i})} - \hat{a}_i \hat{a}_i^*,$$
 (5.43b)

where ${}_{1}F_{1}(a;b;z)$ represents the confluent hypergeometric function [117], defined by the hypergeometric series:

$$_{1}F_{1}(a;b;z) = \sum_{k=0}^{\infty} \frac{(a)_{k}}{(b)_{k}} \frac{z^{k}}{k!}.$$
 (5.44)

The detailed derivation is provided in Appendix.

In Algorithm 5.2, for accelerating convergence, we typically recommend users to initialize \hat{d}_0 based on the actual characteristics of the environment, such as the maximum range or distance resolution. In our subsequent experiments, we initialized it to 0.1 meter. Additionally, we set the EM-loop to terminate when the difference of d_0 before and after the iteration is less than 0.1 meters for greater precision and maximum iteration times to be 20. When transitioning from the Nakagami-m fading model to another statistical model, the EM-ReVAMP algorithm can be adapted by primarily modifying (5.22), (5.35a), and (5.35b). These adjustments will enable the algorithm to effectively accommodate the characteristics of the new statistical model while maintaining its functionality.

5.5.2 Theoretical Cramer-Rao Bound (CRB) For m=1

When m=1, the path complex attenuation coefficients $\mathbf{a} \in \mathbb{C}^{L\times 1}$ that each element a_i $(i=0,\cdots,L-1)$ is an i.i.d. complex zero-mean Gaussian random variable, can be expressed as follows:

$$\mathbf{a} \sim \mathcal{CN}(0, \mathbf{C_{aa}}), \quad \mathbf{C_{aa}} = \begin{bmatrix} \Omega_0(d_0) & \cdots & 0 \\ \vdots & \ddots & \vdots \\ 0 & \cdots & \Omega_{L-1}(d_K) \end{bmatrix}.$$
 (5.45)

To estimate d_0 directly and solely based on \mathbf{y} using the maximum likelihood estimator (MLE) of the pdf of \mathbf{y} given $\Omega(d_0)$, we proceed as follows:

$$p(\mathbf{y}|\mathbf{\Omega}(d_0)) = \pi^{-N} (\det(\mathbf{C}_{\mathbf{y}\mathbf{y}}))^{-1} \exp(-\mathbf{y}^H \mathbf{C}_{\mathbf{y}\mathbf{y}}^{-1} \mathbf{y})$$
(5.46)

where

$$\mathbf{C}_{\mathbf{v}\mathbf{v}} = \mathbf{h}\mathbf{C}_{\mathbf{a}\mathbf{a}}\mathbf{h}^H + \sigma_v^2\mathbf{I}.\tag{5.47}$$

To compute the Fisher Information Matrix (FIM) from the pdf $p(\mathbf{y}|\Omega(d_0))$, the FIM can be represented as follows:

$$J_{d_0 d_0} = \operatorname{tr} \left[\mathbf{C}_{\mathbf{y}\mathbf{y}}^{-1} \frac{\partial \mathbf{C}_{\mathbf{y}\mathbf{y}}}{\partial d_0} \mathbf{C}_{\mathbf{y}\mathbf{y}}^{-1} \frac{\partial \mathbf{C}_{\mathbf{y}\mathbf{y}}}{\partial d_0} \right], \tag{5.48}$$

where tr denotes the trace operator. After some algebraic computations, we obtain the expression in (5.48)

$$\frac{\partial \mathbf{C_{yy}}}{\partial d_0} = \mathbf{h} \frac{\partial \mathbf{C_{aa}}}{\partial d_0} \mathbf{h}^H, \tag{5.49a}$$

$$\frac{\partial \mathbf{C_{aa}}}{\partial d_0} = -nG_0 \begin{bmatrix} (d_0 + c\tau_0)^{-n-1} & \cdots & 0 \\ \vdots & \ddots & \vdots \\ 0 & \cdots & d_0 + c\tau_{K-1})^{-n-1} \end{bmatrix}.$$
(5.49b)

In conclusion, using (5.48) and (5.49), the CRB of d_0 w.r.t. MPCPDP-based ranging can be calculated as follows:

$$CRB_{d_0} = J_{d_0d_0}^{-1}. (5.50)$$

Unfortunately, if $m \neq 1$, the high-dimensional integration required to obtain the likelihood $p(\mathbf{y}|d_0)$ is intractable, making it impossible to calculate its CRB.

Algorithm 5.2 EM-ReVAMP

```
Ensure: \hat{d}_0
Require: \mathbf{y}, \mathbf{h}, p_{\mathbf{v}}(\mathbf{v}), m, [\tau_0, \cdots, \tau_{L-1}], G_0, n
   1: Initialize: d_0
  2: repeat [For t = 0 ... L - 1]
  3: Initialize: \mathbf{m}, \mathbf{C}_m, \mathbf{p}, \boldsymbol{\tau}_p
  4: Update \Omega(\hat{d}_0) w.r.t. G_0, n, \tau_i and \hat{d}_0 with (5.10)
  5:
                 repeat
                         repeat [For each i = 0 \dots L - 1]
  6:
                                 [Update the extrinsic]
   7:
                                \begin{aligned} \boldsymbol{\tau}_{m} &= \operatorname{diag}(\mathbf{C}_{m}) \\ \boldsymbol{r}_{i} &= \frac{\tau_{p_{i}} m_{i} - \tau_{m_{i}} p_{i}}{\tau_{p_{i}} - \tau_{m_{i}}} \\ \boldsymbol{\tau}_{r_{i}} &= \frac{\tau_{m_{i}} \tau_{p_{i}}}{\tau_{p_{i}} - \tau_{m_{i}}} \end{aligned}
  8:
  9:
10:
                                 [Approximate the marginal posterior]
11:
                                 Update \hat{a}_i with (5.43a)
12:
                                 Update \tau_{a_i} with (5.43b)
13:
                                 [Propagate the approximation back]
14:
                                p_i^{new} = \frac{\tau_{r_i} \hat{a}_i - \tau_{a_i} r_i}{\tau_{r_i} - \tau_{a_i}}
\tau_{p_i}^{new} = \frac{\tau_{r_i} \hat{a}_i}{\tau_{r_i} - \tau_{a_i}}
\Delta_{p_i} = \frac{1}{\tau_{p_i}^{new}} - \frac{1}{\tau_{p_i}}
15:
16:
17:
                                 \Psi_{p_i} = \frac{p_i^{n_{ew}}}{\tau_{p_i}^{n_{ew}}} - \frac{p_i}{\tau_{p_i}}
18:
                                 [Update the posterior approximation]
19:
                                 \mathbf{C}_m = h_{\mathbf{C}}(\mathbf{C}_m, \mathbf{e}_i, \Delta_{p_i})
20:
                                 \mathbf{m} = h_{\mathbf{m}}(\mathbf{m}, \mathbf{C}_m, \mathbf{e}_i, \Delta_{p_i}, \Psi_{p_i})
21:
                         until All i-s have been updated
22:
                         \mathbf{p} = \mathbf{p}^{new}
23:
                         oldsymbol{	au}_p = oldsymbol{	au}_p^{new}
24:
                 until Convergence
25:
                 \hat{d}_0 = \arg\min_{d_0} \sum_{i=0}^{L-1} \left[ \ln \Omega_i(d_0) + \frac{\tau_{m_i} + |m_i|^2}{\Omega_i(d_0)} \right) \right]
26:
27: until Convergence
```

5.6 Simulation Results

This section presents the simulation verification using MATLAB to assess the impact of different parameters. Table 6.1 lists the main parameters involved. In general, the primary environmental factors influencing our MPCPDP-based ranging method are the number of distinguishable MPCs, the magnitude of Signal-to-Noise Ratio (SNR), the propagation attenuation factor n, and the shape parameter of Nakagami-m distribution m. In the following subsections, we analyze the effects of these factors on ranging accuracy through simulations. We conducte 10000 times for each scenario and calculate the Root Mean Square Error (RMSE). For m=1, we calculate the square root of CRB (SR-CRB) for our MPCPDP-based ranging method. Moreover, we compare with the SoTA RSS-based ranging method in [118]. In the simulation result figures, we use a solid line to denote the RMSE of the RMSE of the RMSE of the RMSE of the RMSE and a dotted line to denote the SR-CRB.

Table 5.1: Parameters setting for MPCPDP-Based Ranging

Parameter	Value
G_0	1.
SNR (dB)	Range from 0 to 20, default 10.
N	20.
L	Ranging from 2 to 8.
n	Ranging from 2 to 4, default 3.
m	Ranging from 1 to 10, default 5.
$d_0 \; ({ m meter})$	20.
Distance of NLOS path (m)	Random between $1.1d_0$ to $2.0d_0$.
Test repetitions	50.

5.6.1 Impact of SNR and Number of NLoS Paths

In this set of experiments, we set n=3 and examine the influence of SNR and the number of NLoS paths on the estimation bias. Figs. 5.2 and 5.3 illustrate the simulation results for m=1 and m=5, respectively. We observe that varying the SNR from 15dB to 40dB does not significantly affect our performance. Moreover, the estimation accuracy of our method gradually improves with an increasing number of NLoS paths which act better than the RSS-based ranging method under the same conditions. Even for $m \neq 1$, it is hard to get its theoretic CRB, comparison to RSS-based ranging method can show our method's high precision.

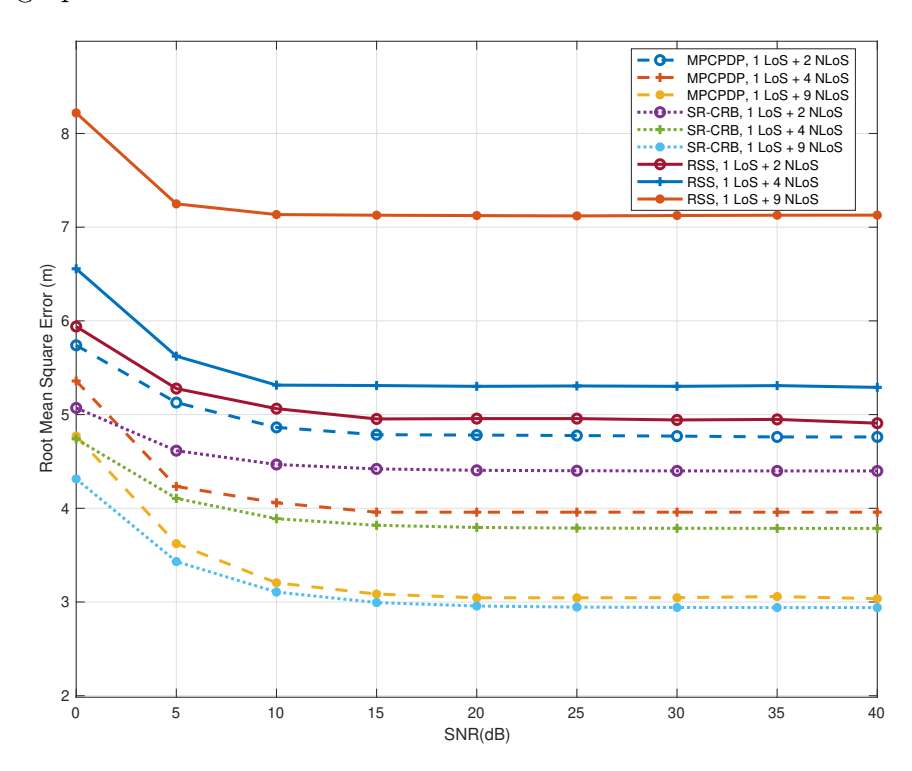


Figure 5.2: The impact of SNR and the number of NLoS paths on d_0 estimation with m=1

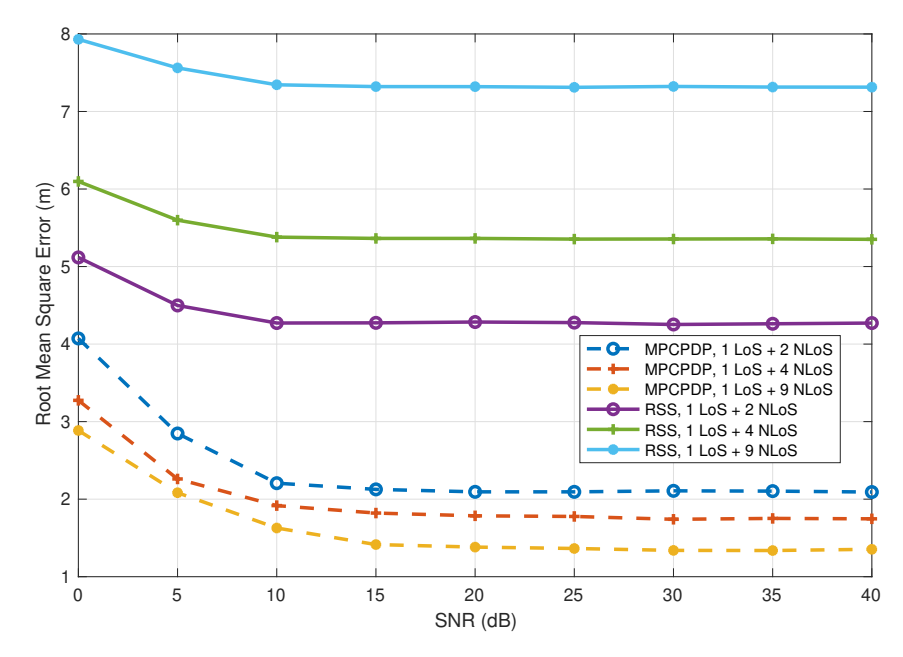


Figure 5.3: The impact of SNR and the number of NLoS paths on d_0 estimation with m=5

5.6.2 Impact of the propagation fading factor n and Number of NLoS Paths

This set of experiments investigates the effects of the environmental propagation fading factor n and the number of NLoS paths on the estimation bias. The simulation results, depicted in Figs. 5.4 and 5.5 for m=1 and m=5, respectively, indicate that the variation of n within the range of 2 to 4 has a obvious impact on our performance. As n increases, the variance of Nakagami-m actually decreases, thus leading to an increase in estimation accuracy for both the RSS-based ranging method and our method. This is theoretically verified by the SR-CRB when m=1. It is clear to see that our method consistently performs better than the RSS-based ranging method for different n.

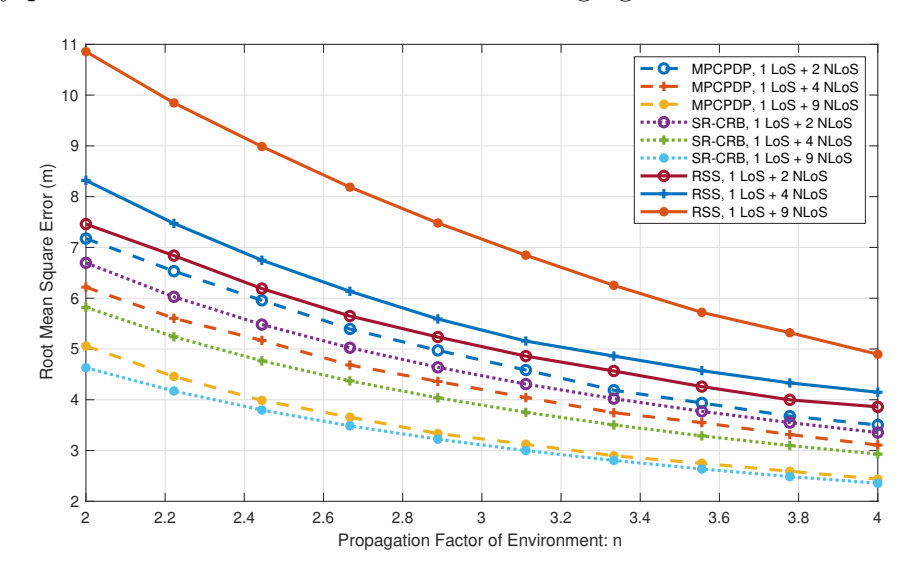


Figure 5.4: The impact of the environment propagation fading factor n and the number of NLoS paths on d_0 estimation with m = 1

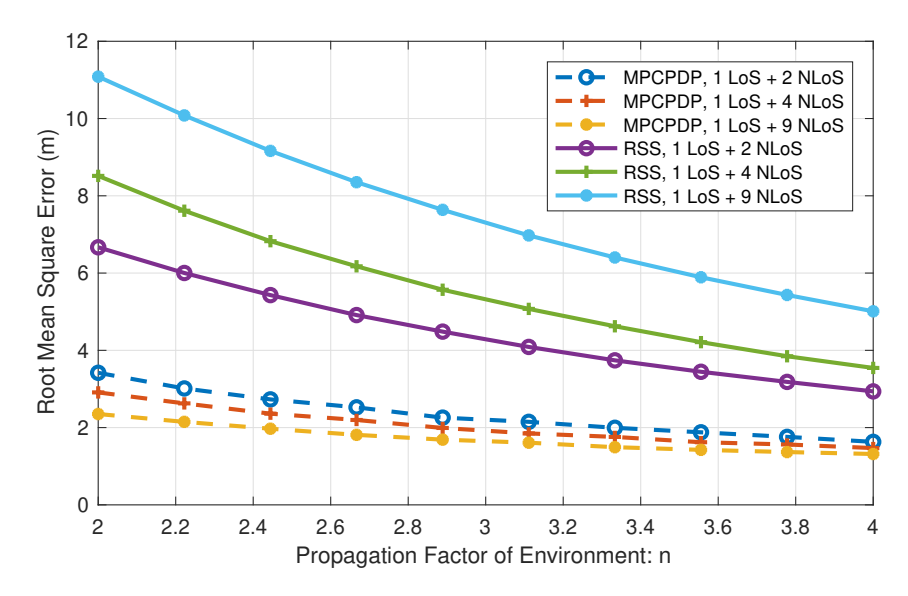


Figure 5.5: The impact of the environment propagation fading factor n and the number of NLoS paths on d_0 estimation with m=5

5.6.3 Impact of the shape parameter m and Number of NLoS Paths

In this simulation, we set n as 3, SNR as 10 dB, d_0 as 20 meters, and we examine the influence of the shape parameter of the Nakagami-m distribution, denoted as m, and the number of NLoS paths on the estimation bias. Fig. 5.6 presents the simulation results, indicating that varying m from 1 to 10 significantly affects the performance of MPCPDP-based ranging method. As m increases, the variance of Nakagami-m distribution decreases and the accuracy of estimation method gets higher. Moreover, with the number of NLoS paths increases, the performance of our method also increases but RSS-based ranging generally decreases. Obviously, under the same condition, the method proposed in this paper has the small range error compared to the RSS-based range method. In addition, the range error of the new method decreases along with the number of NLoS paths increases.

5.6.4 Impart of number of NLoS and the mismatched shape parameter m

We investigate the impact of a mismatched shape parameter m in the Nakagami-m distribution, where we set a true value of m=5, SNR = 10 and n=3. Our simulations reveal that the estimation error is relatively small when the deviation of m is not substantial. This observation underscores the robustness of our algorithm under theoretical conditions. However, achieving accurate parameter initialization in practical scenarios is challenging, and significant errors in initialization may lead to substantial estimation deviations. One approach to address this challenge is to jointly estimate all parameters using the EM algorithm, which remains a topic for our future research. While theoretically effective of the EM algorithm, this method encounters difficulties due to the complex nonlinear relationships among parameters and non-convex optimization problems. Moreover, increasing the number of parameters to estimate can degrade performance due to constraints imposed by available observed data. Another promising approach that warrants further research attention is minimizing errors resulting from model mismatches.

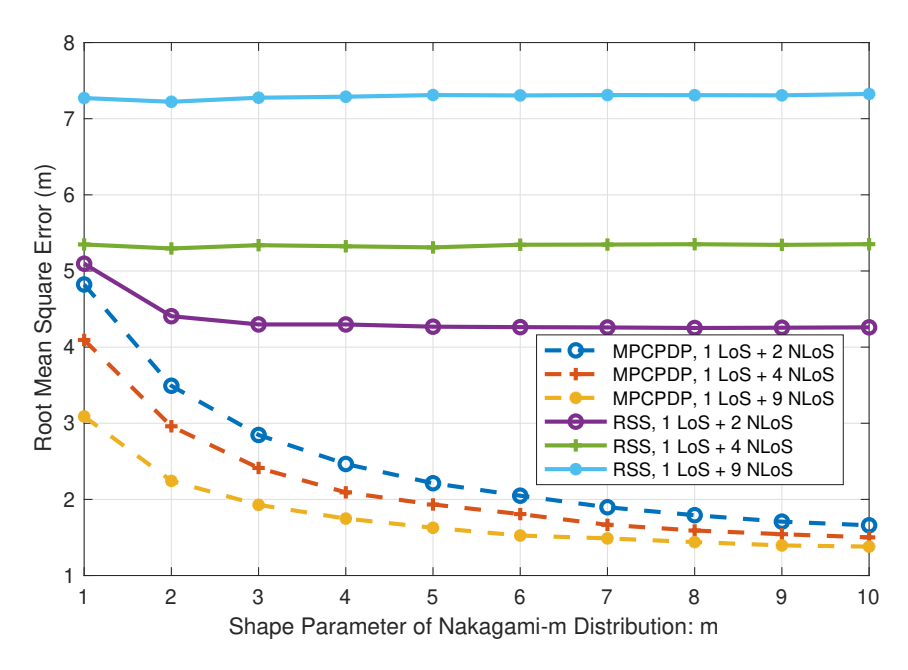


Figure 5.6: The impact of the Nakagami-m distribution's shape parameter m and the number of NLoS paths on d_0 estimation with n=3

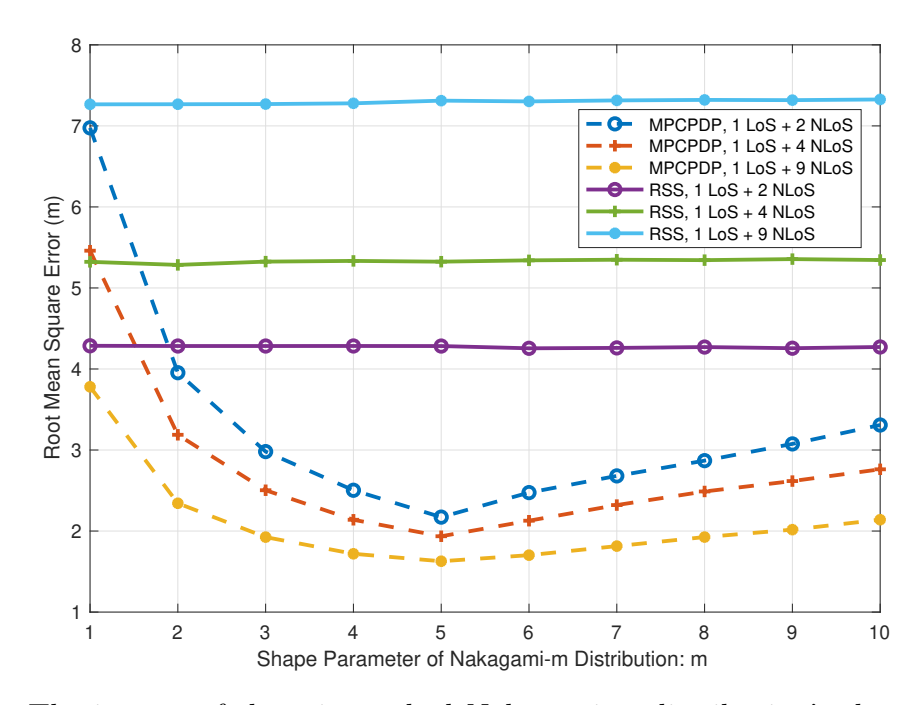


Figure 5.7: The impact of the mismatched Nakagami-m distribution's shape parameter m and the number of NLoS paths on d_0 estimation with true m=5

5.6.5 Simulation Conclusions

Based on experimental simulations with varying SNR values, n and m, and the number of NLoS paths, our method has demonstrated strong performance in diverse and complex environments. Notably, the number of NLoS paths has emerged as a crucial parameter, significantly influencing estimation accuracy. As the number of NLoS paths increases, our algorithm's accuracy improves, whereas the performance of the RSS-based method declines. Furthermore, as m or n increases, the variance of the fading channel decreases, thereby enhancing our method's performance. Consequently, in complex environments characterized by significant fading with large m and n and multiple NLoS paths, the MPCPDP-based ranging algorithm proves to be a more effective solution than the RSS-based method for estimating the LoS distance.

5.7 Conclusions

In conclusion, we propose a novel MPCPDP-based ranging method, aimed at exploit multipath effect. To theoretically validate the feasibility of our approach, we selected the widely adopted Nakagami-m statistical model and established a relationship between distribution parameters and propagation distance. On one hand, this model ensures its applicability across the majority of cases; on the other hand, it exemplifies many other statistical models that traditional estimation tools cannot approach. To address the challenges of ranging estimation, which involve hidden random variables and intractable posterior distributions due to complex statistical models such as the Nakagami-m model, we introduce the EM-ReVAMP algorithm. The simulation results convincingly demonstrate the effectiveness of our approach than the RSS-based ranging method, providing substantial evidence to support the accuracy and robustness of our approach. Moreover, the EM-ReVAMP algorithm can be adapted for other statistical fading models with minor modifications, assuming that the statistical models and their parameter initializations are sufficiently accurate. To further validate the practicality and effectiveness of our method, our next objective is to collect measurement data from diverse environments and conduct comprehensive experimental analysis. This pivotal step will enable us to assess the performance of our method in real-world scenarios. Additionally, exploring further application scenarios of EM-ReVAMP and investigating its theoretical performance are essential aspects that warrant attention. Finally, the robustness and accuracy of this algorithm need to undergo further testing.

Chapter 6

Multipath Component Power Delay Profile Based Sensing

6.1 Introduction

Our earlier chapter 5 proposed a multipath component power delay profile (MPCPDP)-based ranging approach in orthogonal frequency-division multiplexing (OFDM) systems. By modeling the power delay profile (PDP) using a Nakagami-m distribution, we established a relationship between the distribution parameters and the propagation distance, achieving more robust ranging than conventional RSS-based methods. However, while our approach reduced hardware requirements and susceptibility to multipath interference, it was originally limited to static environments and integer-delay assumptions, without accounting for Doppler effects caused by relative motion.

In this chapter, we focus on the more challenging case where both delays and Doppler shifts are non-integer (fractional). We formulate a time-domain estimation model that jointly enables communication channel estimation and sensing parameter recovery, thereby supporting integrated sensing and communication. For the delay domain, we construct an oversampled delay grid to represent fractional delays, which naturally leads to a sparse representation of the multipath channel. For the Doppler domain, we model the frequency shifts induced by relative motion, enabling the estimation of both the line-of-sight (LoS) distance and velocity.

To solve the resulting high-dimensional estimation problem, we propose an Expectation Maximization–Expectation Consistent (EM-EC) algorithm under the assumption that MPC amplitudes follow a Nakagami-m distribution and phases are uniformly distributed over $[0, 2\pi)$. The EM-EC framework jointly: 1) Identifies LoS and NLoS components in the oversampled delay grid; 2) Estimates Doppler shifts and the LoS path distance; and 3) Recovers the sparse scattering profile without prior knowledge of the number of paths.

In addition, we analyze the fixed points of the EM-EC algorithm, providing theoretical insights into its convergence behavior and estimation accuracy. Extensive simulations confirm the effectiveness of the proposed method in dynamic multipath environments, demonstrating accurate joint delay—Doppler estimation and robust sensing performance under different conditions.

The primary contributions of this chapter are:

• Fractional delay–Doppler modeling and time-domain estimation: We formulate a joint estimation model that explicitly accounts for non-integer delays and

Doppler shifts, which allows accurate communication channel estimation while simultaneously providing range—Doppler sensing capability in ISAC systems.

- EM-EC algorithm for sparse sensing and parameter estimation: We design an EM-EC framework that operates on an oversampled delay grid, capable of identifying LoS/NLoS components, estimating Doppler shifts, and determining the LoS distance under Nakagami-m amplitude and uniform phase assumptions.
- Fixed-point analysis of the EM-EC algorithm: We derive and study the fixed-point equations of the proposed algorithm, offering theoretical understanding of its convergence and accuracy.

The remainder of this chapter is organized as follows: Section 6.2 introduces the system model and time-domain signal representation. Section 6.3 describes the MPCPDP-based sensing formulation with fractional delay—Doppler grids. Section 6.4 presents the EM-EC algorithm for joint parameter and sparse component estimation. Section 6.5 analyzes the convergence and fixed points of the proposed method. Section 6.6 presents simulation results, and Section 6.7 concludes the chapter with a summary and future research directions.

6.2 Doubly Fractional System Model

6.2.1 Transmitter Structures

We consider a unified representation for different modulation schemes. Let $\mathbf{x} \in \mathbb{C}^N$ denote the modulation-domain symbol vector, and let $\mathbf{s} \in \mathbb{C}^N$ denote the corresponding time-domain transmit block after CP removal. The mapping between \mathbf{x} and \mathbf{s} can be expressed as

$$\mathbf{s} = \mathbf{U}^H \mathbf{x},\tag{6.1}$$

where $\mathbf{U} \in \mathbb{C}^{N \times N}$ is a unitary transformation matrix determined by the modulation scheme.

In orthogonal frequency-division multiplexing (OFDM), the modulation domain is the frequency domain. Let $\mathbf{F} \in \mathbb{C}^{N \times N}$ denote the normalized N-point discrete Fourier transform (DFT) matrix, given by

$$[\mathbf{F}]_{k,n} = \frac{1}{\sqrt{N}} e^{-j\frac{2\pi}{N}kn}, \quad k, n = 0, \dots, N - 1.$$
 (6.2)

The transformation matrix is

$$\mathbf{U} = \mathbf{F}, \quad \mathbf{s} = \mathbf{F}^H \mathbf{x}, \tag{6.3}$$

where \mathbf{x} contains the complex symbols mapped to subcarriers. OFDM simplifies equalization in frequency-selective channels, but suffers from high PAPR and sensitivity to carrier frequency offset.

6.2.2 Time-Domain Equivalent Channel Representation After CP Removal

We consider the baseband discrete-time model after CP removal at the receiver. Let $\mathbf{s} \in \mathbb{C}^N$ denote the N useful time-domain samples in a transmit block, and $\mathbf{y} \in \mathbb{C}^N$

the corresponding received block. The propagation channel is assumed to consist of L propagation paths. The ℓ -th path is characterized by the complex gain $\alpha_{\ell} \in \mathbb{C}$, delay τ_{ℓ} (possibly fractional), and Normalized Doppler shift ν_{ℓ} . The sampling period is T_s and the sampling rate $F_s = 1/T_s$.

We assume:

- The transmit waveform is bandlimited and sampled at the Nyquist rate.
- The CP length $N_{\rm cp}$ satisfies $\max_{\ell} \tau_{\ell} < N_{\rm cp} T_s$, ensuring that inter-block interference is avoided and the useful part of the block undergoes circular convolution.

1) Circular fractional-delay operator

For a bandlimited sequence, a delay of τ seconds corresponds in discrete time to a fractional shift implemented by the N-periodic Dirichlet kernel

$$\operatorname{sinc}_{N}(\Delta) \triangleq \frac{\sin(\pi \Delta)}{N \sin(\frac{\pi}{N} \Delta)}, \qquad \Delta \in \mathbb{R},$$
 (6.4)

which reduces to a circular shift when Δ is an integer. The associated *circular fractional-delay* matrix $\mathbf{C}(\tau) \in \mathbb{C}^{N \times N}$ is

$$\left[\mathbf{C}(\tau)\right]_{n,m} = \operatorname{sinc}_{N}\left(n - m - \frac{\tau}{T_{s}}\right), \qquad n, m = 0, \dots, N - 1.$$
(6.5)

This circulant Toeplitz matrix implements a delay of τ seconds modulo the block length NT_s .

2) Doppler modulation operator

A Normalized Doppler shift ν induces a per-sample phase rotation $e^{j2\pi\nu n/N}$ in discrete time. This is represented by the diagonal matrix

$$\left[\mathbf{D}(\nu)\right]_{n,m} = e^{j2\pi\nu n/N} \,\delta_{n,m}, \qquad n, m = 0, \dots, N - 1.$$
 (6.6)

The normalized Doppler shift ν can be expressed as:

$$\nu = \frac{v \cos(\theta) f_c}{c \Delta f} \tag{6.7}$$

where f_c is the carrier frequency, v is the velocity of the terminal, c is the speed of light, θ is the moving angle and uniformly distributed in the interval $[-\pi, \pi]$, and Δf is the chirp subcarrier spacing.

3) Per-path channel contribution

For a single path (α, τ, ν) , the received samples after CP removal and without noise can be written as

$$y[n] = \alpha e^{j2\pi\nu n/N} \sum_{m=0}^{N-1} \operatorname{sinc}_N \left(n - m - \frac{\tau}{T_s} \right) s[m].$$
 (6.8)

In matrix form, (6.8) becomes

$$\mathbf{y} = \alpha \,\mathbf{D}(\nu) \,\mathbf{C}(\tau) \,\mathbf{s},\tag{6.9}$$

which shows that the per-path channel matrix factorizes into a Doppler operator and a delay operator.

4) Multi-path equivalent channel matrix

By linear superposition over all L paths, the equivalent $N \times N$ channel matrix is

$$\mathbf{H}_{t} = \sum_{\ell=1}^{L} \alpha_{\ell} \mathbf{D}(\nu_{\ell}) \mathbf{C}(\tau_{\ell})$$
(6.10)

with the (n, m)-th entry of \mathbf{H}_t is

$$[\mathbf{H}_t]_{n,m} = \sum_{\ell=1}^{L} \alpha_{\ell} e^{j2\pi\nu_{\ell}n/N} \operatorname{sinc}_N \left(n - m - \frac{\tau_{\ell}}{T_s} \right), \qquad n, m = 0, \dots, N - 1,$$
 (6.11)

and the block input-output relation reads

$$\mathbf{y}_t = \mathbf{H}_t \mathbf{s} + \mathbf{v}, \quad \mathbf{v} \sim \mathcal{CN}(\mathbf{0}, \sigma_n^2 \mathbf{I}_N).$$
 (6.12)

6.3 MPCPDP-Based Sensing Problem Formulation

Based on (6.12), from the noisy block observation (6.12). Recalling the equivalent channel decomposition in (6.10), we have

$$\mathbf{y}_t = \sum_{\ell=1}^{L} \alpha_{\ell} \mathbf{D}(\nu_{\ell}) \mathbf{C}(\tau_{\ell}) \mathbf{s} + \mathbf{v}.$$
 (6.13)

As in channel estimation phase, the block pilot s is assumed to be known while $\{\alpha_{\ell}, \nu_{\ell}, \tau_{\ell}\}_{\ell=1}^{L}$ are unknown. Moreover, in practical wideband systems, the normalized Doppler shifts satisfy

$$|\nu_{\ell}| \ll 1, \quad \forall \ell,$$
 (6.14)

which allows the first-order Taylor expansion around $\nu_{\ell} = 0$

$$\mathbf{D}(\nu_{\ell}) \approx \mathbf{I}_N + \nu_{\ell} \mathbf{T},\tag{6.15}$$

where $\mathbf{T} = \text{diag}(0, j2\pi/N, \dots, j2\pi(N-1)/N)$. Substituting into (6.13) yields

$$\mathbf{y}_{t} \approx \underbrace{\sum_{\ell=1}^{L} \alpha_{\ell} \mathbf{C}(\tau_{\ell}) \mathbf{s}}_{\text{zero-Doppler term}} + \underbrace{\sum_{\ell=1}^{L} \nu_{\ell} \alpha_{\ell} \mathbf{T} \mathbf{C}(\tau_{\ell}) \mathbf{s}}_{\text{Doppler correction}} + \mathbf{v}. \tag{6.16}$$

Define

$$\mathbf{A} \triangleq \left[\mathbf{C}(\tau_1)\mathbf{s}, \ldots, \mathbf{C}(\tau_L)\mathbf{s} \right], \tag{6.17}$$

$$\mathbf{B} \triangleq \left[\mathbf{TC}(\tau_1)\mathbf{s}, \dots, \mathbf{TC}(\tau_L)\mathbf{s} \right], \tag{6.18}$$

$$\boldsymbol{\alpha} \triangleq [\alpha_1, \dots, \alpha_L]^\top, \quad \boldsymbol{\nu} \triangleq [\nu_1, \dots, \nu_L]^\top.$$
 (6.19)

Then (6.16) can be written compactly as

$$\mathbf{y}_t \approx (\mathbf{A} + \mathbf{B}\operatorname{diag}(\boldsymbol{\nu}))\boldsymbol{\alpha} + \mathbf{v}.$$
 (6.20)

For each individual element $\alpha_{\ell} = |\alpha_{\ell}| e^{j\phi_{\ell}}$ of α , the magnitude $|\alpha_{\ell}|$ is modeled by a Nakagami-m distribution, while the phase ϕ_{ℓ} follows a uniform distribution between $[-\pi, \pi]$. Consequently, the probability density functions (pdfs) of the magnitude and phase of α_{ℓ} are expressed as follows:

$$p(|\alpha_{\ell}|; \Omega_{\ell}) = \frac{2m^m |\alpha_{\ell}|^{2m-1}}{\Gamma(m)\Omega_{\ell}^m} \exp\left[-\frac{m|\alpha_{\ell}|^2}{\Omega_{\ell}}\right], m \ge 0.5;$$
(6.21a)

$$p(\phi_{\ell}) = \frac{1}{2\pi}, \phi_{\ell} \in [0, 2\pi),$$
 (6.21b)

where $\Gamma(\cdot)$ denotes the gamma function, Ω_{ℓ} is the average power intensity of the path i and m is the shape parameter of the Nakagami-m distribution. The shape parameter m governs the fading characteristics of the distribution. For lower values of m, the distribution approximates a Rayleigh distribution with a faster decay, while higher values of m result in a more concentrated distribution around its mean, indicating less severe fading. In practice, m is typically estimated from channel measurements to accurately capture the fading characteristics of the specific wireless channel. Moreover, the parameter Ω_{ℓ} is defined in a similar way as in Chapter 5 and can be expressed as

$$\Omega_{\ell}(d_0) = P_t G_t G_r \left[\frac{\lambda}{4\pi (d_0 + c\tau_{\ell})} \right]^{n_{\ell}} = G_0 (d_0 + c\tau_{\ell})^{-n_{\ell}}, \tag{6.22}$$

where the involved variables are given as follows: P_t is the transmitted power, G_t denotes the transmitting antenna gain, λ is the wavelength of the electromagnetic wave, c is the speed of light, d_0 represents the LoS distance, τ_ℓ denotes the excess delay of the ℓ -th path relative to the LoS path, and n_ℓ is the propagation loss exponent of the ℓ -th path determined by the surrounding environment. Different from the previous formulation, here we allow n_ℓ to take different values for the LoS and NLoS components, so that heterogeneous path-loss behaviors can be captured. We assume that the LoS path always exists.

6.3.1 Delay dictionary construction

Since the true delays $\{\tau_{\ell}\}$ are continuous, we approximate them using a delay grid

$$\mathcal{T} = \{\hat{\tau}_1, \dots, \hat{\tau}_{G_\tau}\},\tag{6.23}$$

with grid size G_{τ} . For each $\hat{\tau}_g \in \mathcal{T}$, define

$$\mathbf{a}_{a} = \mathbf{C}(\hat{\tau}_{a})\mathbf{s},\tag{6.24a}$$

$$\mathbf{b}_g = \mathbf{TC}(\hat{\tau}_g)\mathbf{s}.\tag{6.24b}$$

The corresponding delay dictionaries are

$$\tilde{\mathbf{A}} = [\mathbf{a}_1, \dots, \mathbf{a}_{G_{\tau}}], \tag{6.25a}$$

$$\tilde{\mathbf{B}} = [\mathbf{b}_1, \dots, \mathbf{b}_{G_\tau}]. \tag{6.25b}$$

By replacing (\mathbf{A}, \mathbf{B}) in (6.20) with $(\tilde{\mathbf{A}}, \tilde{\mathbf{B}})$, we obtain a parametric model

$$\mathbf{y}_t \approx (\tilde{\mathbf{A}} + \tilde{\mathbf{B}}\operatorname{diag}(\tilde{\boldsymbol{\nu}}))\mathbf{h} + \mathbf{v},$$
 (6.26)

where $\mathbf{h} \in \mathbb{C}^{G_{\tau}}$ stacks the grid gains, and $\boldsymbol{\nu} \in \mathbb{R}^{G_{\tau}}$ stacks the (small) Doppler shifts per grid atom. Moreover, \mathbf{h} is sparse with non-zero entries corresponding to the actual path delays.

Statistical prior on path gains

We impose the following prior model for each coefficient h_i : The amplitude $|h_i|$ follows a Nakagami-m distribution with shape parameter m > 0 and spread parameter Ω_i :

$$p(|h_i|) = \frac{2m^m |h_i|^{2m-1}}{\Gamma(m) \Omega_i^m} e^{-\frac{m}{\Omega_i} |h_i|^2}, \quad |h_i| \ge 0.$$

The phase $arg(h_i)$ is uniformly distributed over $[0, 2\pi)$, reflecting the lack of prior knowledge about phase.

Applying the Jacobi determinant [113], the pdf of the complex fading coefficient h_i (circularly symmetric with Nakagami-m envelope and uniform phase) is

$$p_{h_i}(h_i; \Omega_i) = \frac{m^m}{\pi \Gamma(m) \Omega_i^m} |h_i|^{2m-2} \exp\left(-\frac{m}{\Omega_i} |h_i|^2\right).$$

$$(6.27)$$

In our framework, m will be set from a calibration stage, while Ω_i is treated as a learnable large–scale parameter. Note that as $\Omega_i \to 0^+$, (6.27) collapses to a Dirac measure at the origin, implying $h_i = 0$ (sparsity on the delay grid).

For atoms that correspond to physical paths, we couple the spread parameter to a path-loss model,

$$\Omega_i = \Omega(d_0, d_i) = G_0 (d_0 + d_i)^{-n_i}, \tag{6.28}$$

with unknown offset d_0 (e.g., reference distance), known geometric increments d_i , reference gain G_0 , and exponent n_i . For atoms outside the support, we set $\Omega_i = 0$, which is consistent with $h_i = 0$ by (6.27).

Building on (6.23)–(6.28), we proceed as follows:

- 1. Using the known s and a delay grid \mathcal{T} , form $\hat{\mathbf{A}}$ and $\hat{\mathbf{B}}$ as defined earlier.
- 2. On the full grid, jointly estimate $(\mathbf{h}, \tilde{\boldsymbol{\nu}})$ from (6.26) under the circular Nakagami-m prior (6.27) for h_i (with learnable Ω_i). This step yields dense preliminary estimates in which most h_i are driven close to zero by the prior.
- 3. Apply a decision rule to declare the support $\widehat{S} = \{i : \widehat{h}_i \neq 0\}$, e.g., via magnitude thresholding or a posterior-odds criterion consistent with the degeneracy $\widehat{\Omega}_i \to 0 \Rightarrow h_i = 0$. Retain $\{\widehat{h}_i, \widehat{\nu}_i\}_{i \in \widehat{S}}$ and set $\widehat{h}_i = 0$ for $i \notin \widehat{S}$. Moreover, based on \widehat{S} , we can get estimated \widehat{d}_i as $\{\widehat{d}_i = c\widehat{\tau}_i\}_{i \in S}$.
- 4. With $\{\widehat{\Omega}_i\}_{i\in\widehat{\mathcal{S}}}$ and the coupling $\Omega_i = \Omega(d_0, d_i) = G_0(d_0 + d_i)^{-n_i}$ in (6.28), estimate d_0 in a subsequent large-scale fitting stage.

This staged program keeps the modeling consistent with (6.27) and (6.26): s is absorbed into the dictionary, sparsity is enforced through $\Omega_i \downarrow 0$, and Doppler enters linearly via the first-order expansion, enabling a clean separation between small-scale $(\mathbf{h}, \boldsymbol{\nu})$ and LoS distance (d_0) inference. The concrete algorithmic choices and optimizers are deferred to the next section.

6.3.2 MPCPDP-based Ranging and Doppler Shift Estimation

Our objectives are twofold: first, to estimate $\tilde{\Omega} = \{\Omega_i\}_{i=1}^{G_{\tau}}$ and $\tilde{\nu}$, and second, to derive d_0 from the estimated $\tilde{\Omega}$. To achieve the first objective, we employ the joint maximum likelihood estimation (MLE) method, which reformulates the problem as follows:

$$[\widehat{\tilde{\Omega}}, \widehat{\tilde{\nu}}] = \arg \max_{\tilde{\Omega}, \tilde{\nu}} \ell(\tilde{\Omega}, \tilde{\nu}; \mathbf{y}_{t}) = \arg \max_{\tilde{\Omega}, \tilde{\nu}} \ln p(\mathbf{y}_{t}; \tilde{\Omega}, \tilde{\nu}), \tag{6.29}$$

where $\ell(\cdot)$ denotes the log-likelihood function. Regarding the optimization problem, the likelihood function in (6.29) can be expressed as:

$$p(\mathbf{y}_{t}; \tilde{\mathbf{\Omega}}, \tilde{\boldsymbol{\nu}}) = \int p_{\mathbf{y}_{t}}(\mathbf{y}_{t}; \mathbf{h}, \tilde{\boldsymbol{\nu}}) p_{\mathbf{h}}(\mathbf{h}; \tilde{\mathbf{\Omega}}) d\mathbf{h}.$$
 (6.30)

The pdf $p(\mathbf{y}_t; \tilde{\mathbf{\Omega}}, \tilde{\boldsymbol{\nu}})$ is crucial for estimating $\tilde{\mathbf{\Omega}}$ and $\tilde{\boldsymbol{\nu}}$ based on received signal \mathbf{y}_t . However, solving the integral problem directly to acquire $p(\mathbf{y}_t; \tilde{\mathbf{\Omega}}, \tilde{\boldsymbol{\nu}})$ is intractable, as finding an analytical form poses significant challenges. Furthermore, the latent variable \mathbf{h} is unobserved, and its distribution is unknown before reaching $\tilde{\mathbf{\Omega}}$. To tackle these challenges, the EM-EC algorithm is introduced later on. Moreover, The parameter $d_i = c\tau_i$ representing the distance difference between the LoS path and the *i*-th path, also needs to be estimated.

6.4 Expectation Maximization (EM) - Expectation Consistant (EC) Algorithm

6.4.1 Review of Expectation Maximization

Since direct optimization of (6.29) is infeasible, we reformulate it into an iterative update process, laying the foundation for employing the EM algorithm. Using the MM framework, we construct a more tractable lower bound for the log-likelihood function in (6.29). Based on Bayes rules, we define the posterior pdf $p(\mathbf{h}|\mathbf{y}_t, \tilde{\Omega}, \tilde{\nu})$ as follows:

$$p(\mathbf{h}|\mathbf{y}_t, \tilde{\mathbf{\Omega}}, \tilde{\boldsymbol{\nu}}) = \frac{p_{\mathbf{y}_t}(\mathbf{y}_t; \mathbf{h}, \tilde{\boldsymbol{\nu}}) p_{\mathbf{h}}(\mathbf{h}; \tilde{\mathbf{\Omega}})}{\int p_{\mathbf{y}_t}(\mathbf{y}_t; \mathbf{h}, \tilde{\boldsymbol{\nu}}) p_{\mathbf{h}}(\mathbf{h}; \tilde{\mathbf{\Omega}}) d\mathbf{h}}.$$
(6.31)

At the t-th iteration, given the current estimates $\tilde{\Omega}^{(t)}$, we can express the problem as follows:

$$\ell(\tilde{\Omega}, \tilde{\nu}) - \ell(\tilde{\Omega}^{(t)}, \tilde{\nu}^{(t)}) \tag{6.32a}$$

$$= \ln \int p_{\mathbf{y}_t}(\mathbf{y}_t; \mathbf{h}, \tilde{\boldsymbol{\nu}}) p_{\mathbf{h}}(\mathbf{h}; \tilde{\boldsymbol{\Omega}}) d\mathbf{h} - \ln p(\mathbf{y}; \tilde{\boldsymbol{\nu}}^{(t)}, \tilde{\boldsymbol{\Omega}}^{(t)})$$
(6.32b)

$$= \ln \int \frac{p_{\mathbf{y}_t}(\mathbf{y}_t; \mathbf{h}, \tilde{\boldsymbol{\nu}}) p_{\mathbf{h}}(\mathbf{h}; \tilde{\boldsymbol{\Omega}})}{p(\mathbf{h}|\mathbf{y}_t, \tilde{\boldsymbol{\Omega}}^{(t)}, \tilde{\boldsymbol{\nu}}^{(t)})} p(\mathbf{h}|\mathbf{y}_t, \tilde{\boldsymbol{\Omega}}^{(t)}, \tilde{\boldsymbol{\nu}}^{(t)}) d\mathbf{h}$$

$$-\int p(\mathbf{h}|\mathbf{y}_t, \tilde{\mathbf{\Omega}}^{(t)}, \tilde{\boldsymbol{\nu}}^{(t)}) \ln p(\mathbf{y}_t; \tilde{\boldsymbol{\nu}}^{(t)}, \tilde{\mathbf{\Omega}}^{(t)}) d\mathbf{h}$$
(6.32c)

$$\geq \int p(\mathbf{h}|\mathbf{y}_t, \tilde{\mathbf{\Omega}}^{(t)}, \tilde{\boldsymbol{
u}}^{(t)})$$

$$\times \ln \frac{p_{\mathbf{y}_{t}}(\mathbf{y}_{t}; \mathbf{h}, \tilde{\boldsymbol{\nu}}) p_{\mathbf{h}}(\mathbf{h}; \tilde{\boldsymbol{\Omega}})}{p(\mathbf{y}_{t}; \tilde{\boldsymbol{\nu}}^{(t)}, \tilde{\boldsymbol{\Omega}}^{(t)}) p(\mathbf{h}|\mathbf{y}_{t}, \tilde{\boldsymbol{\Omega}}^{(t)}, \tilde{\boldsymbol{\nu}}^{(t)})} d\mathbf{h}$$
(6.32d)

$$= \mathbb{E}_{p(\mathbf{h}|\mathbf{y},\tilde{\mathbf{\Omega}}^{(t)},\tilde{\boldsymbol{\nu}}^{(t)})} \left[\ln \frac{p_{\mathbf{y}_t}(\mathbf{y}_t;\mathbf{h},\tilde{\boldsymbol{\nu}})p_{\mathbf{h}}(\mathbf{h};\tilde{\mathbf{\Omega}})}{p(\mathbf{y}_t;\tilde{\boldsymbol{\nu}}^{(t)},\tilde{\mathbf{\Omega}}^{(t)})p(\mathbf{h}|\mathbf{y}_t,\tilde{\mathbf{\Omega}}^{(t)},\tilde{\boldsymbol{\nu}}^{(t)})} \right].$$
(6.32e)

From (6.32e), it follows that the updates for the update $\tilde{\Omega}^{(t+1)}$ and $\tilde{\nu}^{(t+1)}$ can be derived as:

$$[\tilde{\mathbf{\Omega}}^{(t+1)}, \tilde{\boldsymbol{\nu}}^{(t+1)}] = \arg \max_{\tilde{\mathbf{\Omega}}, \tilde{\boldsymbol{\nu}}} \mathbb{E}_{p(\mathbf{h}|\mathbf{y}_t, \tilde{\mathbf{\Omega}}^{(t)}, \tilde{\boldsymbol{\nu}}^{(t)})} \left[\ln p(\mathbf{y}_t, \mathbf{h}; \tilde{\mathbf{\Omega}}, \tilde{\boldsymbol{\nu}}) \right]. \tag{6.33}$$

It is worth noting that the EM algorithm is guaranteed to converge to a (local) optimal point. Since $\tilde{\Omega}$ and $\tilde{\nu}$ are embedded within $p_{\mathbf{h}}(\mathbf{h}; \tilde{\Omega})$ and $p_{\mathbf{y}_t}(\mathbf{y}_t; \mathbf{h}, \tilde{\nu})$, respectively, a straightforward reorganization leads to the specific EM iteration expressed in (6.33) as:

$$\tilde{\mathbf{\Omega}}^{(t+1)} = \arg \max_{\tilde{\mathbf{\Omega}}} \mathbb{E}_{p(\mathbf{h}|\mathbf{y}_t, \tilde{\mathbf{\Omega}}^{(t)}, \tilde{\boldsymbol{\nu}}^{(t)})} [\ln p_{\mathbf{h}}(\mathbf{h}; \tilde{\mathbf{\Omega}})]; \tag{6.34a}$$

$$\tilde{\boldsymbol{\nu}}^{(t+1)} = \arg \max_{\tilde{\boldsymbol{\nu}}} \mathbb{E}_{p(\mathbf{h}|\mathbf{y}_{t},\tilde{\boldsymbol{\Omega}}^{(t)},\tilde{\boldsymbol{\nu}}^{(t)})} [\ln p_{\mathbf{y}_{t}}(\mathbf{y}_{t};\mathbf{h},\tilde{\boldsymbol{\nu}})]. \tag{6.34b}$$

For simplicity, we define the posterior mean and covariance of \mathbf{h} under the pdf $p(\mathbf{h}|\mathbf{y}_t, \tilde{\mathbf{\Omega}}^{(t)}, \tilde{\boldsymbol{\nu}}^{(t)})$ as follows:

$$\boldsymbol{\mu}_t = \mathbb{E}_{p(\mathbf{h}|\mathbf{y}_t, \tilde{\mathbf{\Omega}}^{(t)}, \tilde{\boldsymbol{\nu}}^{(t)})}[\mathbf{h}]; \tag{6.35a}$$

$$\Sigma_t = \mathbb{E}_{p(\mathbf{h}|\mathbf{y}_t,\tilde{\mathbf{\Omega}}^{(t)},\tilde{\boldsymbol{\nu}}^{(t)})}[(\mathbf{h} - \boldsymbol{\mu}_t)(\mathbf{h} - \boldsymbol{\mu}_t)^H]. \tag{6.35b}$$

It is worth noting that for the shape parameter $m \neq 1$ in the Nakagami-m distribution, solving (6.35) becomes intractable. Therefore, the EC algorithm [119] is employed to address this challenge later on. Before proceeding, let us outline the optimization process for $\tilde{\Omega}$ and $\tilde{\nu}$ given the approximated μ_t and Σ_t .

Optimize $\tilde{\Omega}$

As optimizing $\tilde{\Omega}$ can be decoupled to optimize each element $\tilde{\Omega}_i$ separately. Considering the pdf of h_i , the EM iteration for each $\tilde{\Omega}_i$ in (6.34a) can be reformulated as follows:

$$\tilde{\Omega}_{i}^{(t+1)} = \arg\min_{\Omega_{i}} \left[\ln \Omega_{i} + \frac{\mathbb{E}_{p(h_{i}|\mathbf{y}_{t},\tilde{\mathbf{\Omega}}^{(t)},\tilde{\boldsymbol{\nu}}^{(t)})}[|h_{i}|^{2}]}{\Omega_{i}} \right], \tag{6.36a}$$

$$= \mathbb{E}_{p(h_i|\mathbf{y}_t,\tilde{\mathbf{\Omega}}^{(t)},\tilde{\boldsymbol{\nu}}^{(t)})}[|h_i|^2] \tag{6.36b}$$

$$= |[\boldsymbol{\mu}_t]_i|^2 + [\boldsymbol{\Sigma}_t]_{ii}. \tag{6.36c}$$

In (6.36), the entire optimization function is convex, guaranteeing a unique global minimum point for $\tilde{\Omega}$ at each time.

Optimize $\tilde{\nu}$

When considering the likelihood $p_{\mathbf{y}_t}(\mathbf{y}_t; \mathbf{h}, \tilde{\boldsymbol{\nu}})$, the EM iteration in (6.34b) can be transformed as follows:

$$\tilde{\boldsymbol{\nu}}^{(t+1)} = \arg\min_{\tilde{\boldsymbol{\nu}}} \mathbb{E}_{p(\mathbf{h}|\mathbf{y},\tilde{\boldsymbol{\Omega}}^{(t)},\tilde{\boldsymbol{\nu}}^{(t)})} \left[\|\mathbf{y}_t - [\tilde{\mathbf{A}} + \tilde{\mathbf{B}}\operatorname{diag}(\tilde{\boldsymbol{\nu}})]\mathbf{h}\|^2 \right]
= \arg\min_{\tilde{\boldsymbol{\nu}}} \|\mathbf{y}_t - [\tilde{\mathbf{A}} + \tilde{\mathbf{B}}\operatorname{diag}(\tilde{\boldsymbol{\nu}})]\boldsymbol{\mu}_t\|^2$$
(6.37a)

+ tr
$$\left\{ (\tilde{\mathbf{A}} + \tilde{\mathbf{B}} \operatorname{diag}(\tilde{\boldsymbol{\nu}})) \boldsymbol{\Sigma}_t (\tilde{\mathbf{A}} + \tilde{\mathbf{B}} \operatorname{diag}(\tilde{\boldsymbol{\nu}}))^H \right\}$$
. (6.37b)

After straightforward algebraic manipulation, we obtain the first part in (6.37b):

$$\|\mathbf{y}_{t} - [\tilde{\mathbf{A}} + \tilde{\mathbf{B}}\operatorname{diag}(\tilde{\boldsymbol{\nu}})]\boldsymbol{\mu}_{t}\|^{2} = \|(\mathbf{y}_{t} - \tilde{\mathbf{A}}\boldsymbol{\mu}_{t}) - \tilde{\mathbf{B}}\operatorname{diag}(\boldsymbol{\mu}_{t})\tilde{\boldsymbol{\nu}}\|^{2}$$

$$= \tilde{\boldsymbol{\nu}}^{T}(\boldsymbol{\mu}_{t}\boldsymbol{\mu}_{t}^{H} \odot \tilde{\mathbf{B}}^{T}\tilde{\mathbf{B}}^{*})\boldsymbol{\mu}$$
(6.38a)

$$-2\mathcal{R}\left\{\operatorname{diag}(\boldsymbol{\mu}_t)\tilde{\mathbf{B}}^H(\mathbf{y}_t - \tilde{\mathbf{A}}\boldsymbol{\mu}_t)\right\}^T \tilde{\boldsymbol{\nu}} + C_1, \tag{6.38b}$$

and the second part in (6.37b):

$$\operatorname{tr}\left\{ (\tilde{\mathbf{A}} + \tilde{\mathbf{B}}\operatorname{diag}(\tilde{\boldsymbol{\nu}}))\boldsymbol{\Sigma}_{t}(\tilde{\mathbf{A}} + \tilde{\mathbf{B}}\operatorname{diag}(\tilde{\boldsymbol{\nu}}))^{H} \right\}$$
(6.39a)

$$= 2\mathcal{R} \left\{ \operatorname{diag}(\tilde{\mathbf{B}}^H \tilde{\mathbf{A}} \mathbf{\Sigma}_t) \right\}^T \tilde{\boldsymbol{\nu}} + \tilde{\boldsymbol{\nu}}^T (\mathbf{\Sigma}_t \odot \tilde{\mathbf{B}}^T \tilde{\mathbf{B}}^*) \tilde{\boldsymbol{\nu}} + C_2, \tag{6.39b}$$

where C_1 and C_2 are constants independents of $\tilde{\nu}$.

For the sake of simplicity, we define **P** and γ as follows:

$$\mathbf{P} = \mathcal{R} \left\{ (\boldsymbol{\mu}_t \boldsymbol{\mu}_t^H + \boldsymbol{\Sigma}_t) \odot \tilde{\mathbf{B}}^T \tilde{\mathbf{B}}^* \right\}, \tag{6.40a}$$

$$\gamma = \mathcal{R} \left\{ \operatorname{diag}(\boldsymbol{\mu}_t^*) \tilde{\mathbf{B}}^H (\mathbf{y}_t - \tilde{\mathbf{A}} \boldsymbol{\mu}_t) - \operatorname{diag}(\tilde{\mathbf{B}}^H \tilde{\mathbf{A}} \boldsymbol{\Sigma}_t) \right\}.$$
 (6.40b)

By combining (6.38), (6.39), and (6.40) into (6.37b), we can optimize $\tilde{\nu}$ as follows:

$$\tilde{\boldsymbol{\nu}}^{(t+1)} = \arg\min_{\tilde{\boldsymbol{\nu}}} \tilde{\boldsymbol{\nu}}^T \mathbf{P} \tilde{\boldsymbol{\nu}} - 2 \boldsymbol{\gamma}^T \tilde{\boldsymbol{\nu}} = \mathbf{P}^{-1} \boldsymbol{\gamma}, \tag{6.41}$$

Moreover, as **P** in (6.40a) is a positive semi-definite matrix, $\tilde{\boldsymbol{\nu}}^{(t+1)} = \mathbf{P}^{-1}\boldsymbol{\gamma}$ is a unique global optimal point.

6.4.2 Expectation Consistent Approach

As previously noted, the EM algorithm becomes intractable for a Nakagami-m prior (the shape parameter $m \neq 1$) due to the difficulty of obtaining the posterior mean and covariance in (6.35), which involves complex integration. Consequently, it is essential to develop an alternative algorithm that approximates the posterior distribution with a more tractable one. To address this challenge, we employ the EC algorithm.

Before describing the EC method, we introduce additional notation. Our goal is to approximate $p(\mathbf{h}|\mathbf{y}_t, \tilde{\mathbf{\Omega}}, \tilde{\boldsymbol{\nu}})$ with $q(\mathbf{h})$, which is chosen from an exponential family. The distribution $q(\mathbf{h})$ can be expressed as:

$$q(\mathbf{h}; \boldsymbol{\lambda}_q) = \frac{1}{Z_q} \exp(\boldsymbol{\lambda}_q^T \mathbf{g}(\mathbf{h})), \tag{6.42}$$

where the partition function Z_q is obtained by integration as:

$$Z_q = \int \exp(\boldsymbol{\lambda}_q^T \mathbf{g}(\mathbf{h})) d\mathbf{h}, \tag{6.43}$$

With either initialized or optimized $[\tilde{\Omega}, \tilde{\nu}]$, the EC algorithm attempts to calculate an estimated belief of the posterior pdf $p(\mathbf{h}; \mathbf{y}_t, \tilde{\Omega}, \tilde{\nu})$ of the form of $r(\mathbf{h})$ and $s(\mathbf{h})$ as follows:

$$r(\mathbf{h}) = \frac{1}{Z_r} p_{\mathbf{y}_t}(\mathbf{y}_t | \mathbf{h}, \tilde{\boldsymbol{\nu}}) \exp(\boldsymbol{\lambda}_r^T \mathbf{g}(\mathbf{h})), \tag{6.44a}$$

$$Z_r = \int p_{\mathbf{y}_t}(\mathbf{y}_t | \mathbf{h}, \tilde{\boldsymbol{\nu}}) \exp(\boldsymbol{\lambda}_r^T \mathbf{g}(\mathbf{h})) d\mathbf{h}$$
 (6.44b)

$$s(\mathbf{h}) = \frac{1}{Z_s} p_{\mathbf{h}}(\mathbf{h}; \tilde{\mathbf{\Omega}}) \exp(\boldsymbol{\lambda}_s^T \mathbf{g}(\mathbf{h}))$$
 (6.44c)

$$Z_s = \int p_{\mathbf{h}}(\mathbf{h}; \tilde{\mathbf{\Omega}}) \exp(\boldsymbol{\lambda}_s^T \mathbf{g}(\mathbf{h})) d\mathbf{h}$$
 (6.44d)

where the function vector $\mathbf{g}(\mathbf{h})$ is chosen to enable efficient and tractable computation of the required integrals $(Z_q, Z_r \text{ and } Z_s)$, with the parameters $\boldsymbol{\lambda}$ adjusted to optimize specific criteria. In this context, the terms "efficient" and "tractable" refer to a specific set of approximating functions $\mathbf{g}(\mathbf{h})$. Typically, the i.i.d. complex Gaussian component remains effective and computationally feasible as long as $\mathbf{g}(\mathbf{h})$ includes the first and second moments of \mathbf{h} . Furthermore, optimizing $\tilde{\Omega}$ (6.36) and $\tilde{\boldsymbol{\nu}}$ in (6.41) require only the posterior first-order and second-order moments, reinforcing the suitability of the Gaussian assumption. Under this framework, $\boldsymbol{\lambda}$ and $\mathbf{g}(\mathbf{h})$ can be expressed as:

$$\mathbf{g}(\mathbf{h}) = (2h_1, \dots, 2h_L, -|h_1|^2, \dots, -|h_L|^2)^T,$$
 (6.45a)

$$\boldsymbol{\lambda} = (\eta_1, \dots, \eta_L, \Lambda_1, \dots, \Lambda_L)^T. \tag{6.45b}$$

The detailed steps of the EC algorithm are outlined in Algorithm 6.1. In lines 6.46 and 6.47, these steps are commonly referred to as moment matching between $q(\mathbf{h})$ and $s(\mathbf{h})$ and $r(\mathbf{h})$, respectively, as detailed below:

$$\mathbb{E}_{r}[\mathbf{g}(\mathbf{h})|\mathbf{y}_{t},\boldsymbol{\lambda}_{r},\tilde{\boldsymbol{\nu}}] = \frac{\int \mathbf{g}(\mathbf{h})p(\mathbf{y}|\mathbf{h},\tilde{\boldsymbol{\nu}})\exp(\boldsymbol{\lambda}_{r}^{T}\mathbf{g}(\mathbf{h}))d\mathbf{h}}{\int p(\mathbf{y}_{t}|\mathbf{h},\tilde{\boldsymbol{\nu}})\exp(\boldsymbol{\lambda}_{r}^{T}\mathbf{g}(\mathbf{h}))d\mathbf{h}},$$
(6.48a)

$$\mathbb{E}_{s}[\mathbf{g}(\mathbf{h})|\boldsymbol{\lambda}_{s}, \tilde{\boldsymbol{\Omega}}] = \frac{\int \mathbf{g}(\mathbf{h})p(\mathbf{h}|\tilde{\boldsymbol{\Omega}})\exp(\boldsymbol{\lambda}_{s}^{T}\mathbf{g}(\mathbf{h}))d\mathbf{h}}{\int p(\mathbf{h}|\tilde{\boldsymbol{\Omega}})\exp(\boldsymbol{\lambda}_{s}^{T}\mathbf{g}(\mathbf{h}))d\mathbf{h}}.$$
(6.48b)

In (6.48a), since $p_{\mathbf{y}}(\mathbf{y}|\mathbf{h},\tilde{\boldsymbol{\nu}})$ follows a complex Gaussian distribution, we can express it as:

$$\mathbb{E}_r[\mathbf{h}] = (\operatorname{diag}(\boldsymbol{\lambda}_r) + \sigma_n^{-2} \boldsymbol{\Delta}^H \boldsymbol{\Delta})^{-1} (\sigma_n^{-2} \boldsymbol{\Delta}^H \mathbf{y} + \boldsymbol{\eta}_r); \tag{6.49a}$$

$$\mathbb{E}_r[\mathbf{h}\mathbf{h}^H] = \mathbb{E}_r[\mathbf{h}]\mathbb{E}_r[\mathbf{h}]^H + (\operatorname{diag}(\boldsymbol{\lambda}_r) + \sigma_n^{-2}\boldsymbol{\Delta}^H\boldsymbol{\Delta})^{-1}, \tag{6.49b}$$

Algorithm 6.1 Expectation Consistent Algorithm

1: Input: $\tilde{\mathbf{A}}$, $\tilde{\mathbf{B}}$, \mathbf{y}_t , $\mathbf{g}(\boldsymbol{\lambda})$, $\tilde{\boldsymbol{\Omega}}$, $\tilde{\boldsymbol{\nu}}$

2: Output: λ_q

3: Initialize: λ_r , λ_q , λ_s

4: while stopping criterion not fulfilled do

5: // Message: r to s

6: Solve λ_q by:

$$\mathbb{E}_{q}[\mathbf{g}(\mathbf{h}) \mid \boldsymbol{\lambda}_{q}] = \mathbb{E}_{r}[\mathbf{g}(\mathbf{h}) \mid \mathbf{y}_{\mathrm{af}}, \boldsymbol{\lambda}_{r}, \tilde{\boldsymbol{\nu}}]$$
(6.46)

7: Update: $\lambda_s \leftarrow \lambda_q - \lambda_r$

8: // Message: s to r

9: Solve λ_q by

$$\mathbb{E}_{q}[\mathbf{g}(\mathbf{h}) \mid \boldsymbol{\lambda}_{q}] = \mathbb{E}_{s}[\mathbf{g}(\mathbf{h}) \mid \boldsymbol{\lambda}_{s}, \tilde{\boldsymbol{\Omega}}]$$
(6.47)

10: Update: $\lambda_r \leftarrow \lambda_q - \lambda_s$.

11: end while

where

$$\Delta = \tilde{\mathbf{A}} + \tilde{\mathbf{B}}\operatorname{diag}(\tilde{\boldsymbol{\nu}}); \tag{6.50}$$

therefore, the $\lambda_q = [\boldsymbol{\eta}_q^T, \boldsymbol{\lambda}_q^T]^T$ in line 6.46 can be calculated as:

$$\lambda^{q} = (\mathbb{E}_{r}[\mathbf{h}\mathbf{h}^{H}] - \mathbb{E}_{r}[\mathbf{h}]\mathbb{E}_{r}[\mathbf{h}]^{H})^{-1}; \tag{6.51a}$$

$$\boldsymbol{\eta}^q = \boldsymbol{\lambda}^q \odot \mathbb{E}_r[\mathbf{h}].$$
(6.51b)

Moreover, in (6.48b), as $p_{\mathbf{h}}(\mathbf{h}; \hat{\Omega})$ is given in (6.27), we can have

$$\mathbb{E}_{s}[h_{\ell}] = \frac{m\Omega_{\ell}\eta_{s,l}}{m + \Lambda_{s,l}\Omega_{\ell}} \frac{{}_{1}F_{1}(m+1;2; \frac{\Omega_{\ell}|\eta_{s,l}^{2}|}{m + \Lambda_{s,l}\Omega_{\ell}})}{{}_{1}F_{1}(m;1; \frac{\Omega_{\ell}|\eta_{s,l}^{2}|}{m + \Lambda_{s,l}\Omega_{\ell}})}, \tag{6.52a}$$

$$\mathbb{E}_{s}[|h_{\ell}|^{2}] = \frac{m\Omega_{\ell}\eta_{s,l}}{m + \Lambda_{s,l}\Omega_{\ell}} \frac{{}_{1}F_{1}(m+1;1;\frac{\Omega_{\ell}|\eta_{s,l}^{2}|}{m + \Lambda_{s,l}\Omega_{\ell}})}{{}_{1}F_{1}(m;1;\frac{\Omega_{\ell}|\eta_{s,l}^{2}|}{m + \Lambda_{s,l}\Omega_{\ell}})},$$
(6.52b)

where ${}_{1}F_{1}(a;b;z)$ represents the confluent hypergeometric function, defined by the hypergeometric series:

$$_{1}F_{1}(a;b;z) = \sum_{k=0}^{+\infty} \frac{(a)_{k}z^{k}}{(b)_{k}k!};$$

$$(6.53)$$

where

$$(a)_0 = 1, (a)_k = a(a+1)(a+2)\cdots(a+k-1), \tag{6.54}$$

is the rising factorial. Similar to the approach used previously, the $\lambda_q = [\eta_q^T, \lambda_q^T]^T$ in line 6.47 can be computed as:

$$\boldsymbol{\lambda}^q = (\mathbb{E}_s[\mathbf{h}\mathbf{h}^H] - \mathbb{E}_s[\mathbf{h}]\mathbb{E}_s[\mathbf{h}]^H)^{-1}; \tag{6.55a}$$

$$\boldsymbol{\eta}^q = \boldsymbol{\lambda}^q \odot \mathbb{E}_s[\mathbf{h}].$$
(6.55b)

In addition, it can also be represented as the solution of minimum KL-divergence as bellow:

$$q_r(\mathbf{h}) = \underset{q(\mathbf{h})}{\arg\min} D_{KL}[r(\mathbf{h}; \tilde{\boldsymbol{\nu}}) || q(\mathbf{h})], \tag{6.56}$$

$$q_s(\mathbf{h}) = \underset{q(\mathbf{h})}{\arg\min} D_{KL}[s(\mathbf{h}; \tilde{\mathbf{\Omega}}) || q(\mathbf{h})]. \tag{6.57}$$

The fixed point utilized in the EC algorithm can be expressed as:

$$\mathbb{E}_r[\mathbf{g}(\mathbf{h}); \tilde{\boldsymbol{\nu}}] = \mathbb{E}_s[\mathbf{g}(\mathbf{h}); \tilde{\boldsymbol{\Omega}}] = \mathbb{E}_q[\mathbf{g}(\mathbf{h})]. \tag{6.58}$$

6.4.3 Estimate LoS range d_0 and related velocity $v \cos(\theta_1)$ in LoS direction

Given the estimated PDP $\hat{\tilde{\Omega}}$ from the previous step, we first detect significant components:

$$S = \{ i \mid \hat{\tilde{\Omega}}_i > \epsilon_{\rm th} \}, \tag{6.59}$$

where $\epsilon_{\rm th}$ is a predefined threshold (e.g., 1% of the maximum estimated $\hat{\Omega}_i$).

Here, the index i refers to a delay grid point in the dictionary used for sparse recovery, rather than the actual physical delay sample of the system. The delay grid is intentionally designed with a resolution finer than the system's nominal delay resolution 1/B (where B is the system bandwidth), so that fractional delays—which are difficult to estimate directly—can be approximated by the nearest grid point. Specifically, the grid spacing is given by

$$\Delta_{\tau} = \frac{1}{\eta B}, \quad \eta \ge 1, \tag{6.60}$$

where η is the oversampling factor ($\eta > 1$ corresponds to a finer-than-system grid).

After sparse recovery, each detected grid index $i \in \mathcal{S}$ is mapped to its nominal delay

$$\tau_i = i \cdot \Delta_{\tau},\tag{6.61}$$

and the corresponding excess path length is

$$d_i = c \cdot \tau_i, \tag{6.62}$$

with c denoting the propagation speed.

We then optimize the LoS range d_0 by solving the EM update:

$$d_0^{(t+1)} = \arg\min_{d_0} \sum_{i \in \mathcal{S}} \left[\ln \Omega_i(d_0, d_i) + \frac{\mathbb{E}_{p(h_i|\mathbf{y}_t, \tilde{\mathbf{\Omega}}^{(t)}, \tilde{\boldsymbol{\nu}}^{(t)})}[|h_i|^2]}{\Omega_i(d_0, d_i)} \right], \tag{6.63a}$$

$$= \arg\min_{d_0} \sum_{i \in \mathcal{S}} \left[\ln \Omega_i(d_0, d_i) + \frac{\widehat{\widetilde{\Omega}}_i}{\Omega_i(d_0, d_i)} \right], \tag{6.63b}$$

where $\Omega_i(d_0, d_i)$ denotes the path power model parameterized by the LoS range d_0 and the excess delay d_i . In the second line, the posterior expectation $\mathbb{E}[|h_i|^2]$ is replaced by the corresponding estimated variance $\widehat{\Omega}_i$ obtained from the previous inference stage. Moreover, both $\ln \Omega_i(d_0, d_i)$ and $\frac{1}{\Omega_i(d_0, d_i)}$ are convex function w.r.t. d_0 . This property

Algorithm 6.2 MPCPDP-based Sensing Algorithm

```
1: Input: \mathbf{y}_t, P_n, m, n_\ell, \sigma_n^2
 2: Output: d_0, \nu
 3: Initialize \tilde{\boldsymbol{\nu}} and \hat{\boldsymbol{\Omega}}
 4: Set A and B based on \tilde{\nu} using Eq. (6.25)
 5: while EM stopping criterion not fulfilled do
          // EC algorithm to update oldsymbol{\Omega}
 6:
 7:
         Initialize \lambda_r, \lambda_s
         while EC stopping criterion not fulfilled do
 8:
              Solve \lambda_q using Eq. (6.51)
 9:
              Update \lambda_r using Eq. (6.49)
10:
              Solve \lambda_q using Eq. (6.55)
11:
12:
              Update \lambda_s using Eq. (6.52)
13:
         end while
          // EM algorithm to update \hat{\Omega} and \tilde{m{
u}}
14:
         Optimize \Omega using Eq. (6.36)
15:
         Optimize \tilde{\boldsymbol{\nu}} using Eq. (6.41)
16:
17: end while
18: Determine the active set \hat{\Omega}_{\mathcal{S}} by detecting non-zero components of \hat{\Omega}.
19: Optimize d_0 using active set of \Omega_{\mathcal{S}} via Eq. (6.63)
```

ensures that the entire optimization function is convex, guaranteeing a unique global minimum point for d_0 .

After detecting the LoS path from the estimated power delay profile $\tilde{\Omega}$, the corresponding Doppler shift ν_1 can be extracted from $\hat{\nu}$. This allows us to compute the LoS-direction velocity component $v\cos(\theta_1)$ directly from (6.6). Such an estimate provides valuable kinematic information for tracking, as it captures the relative motion along the direct path and can be fused with range estimates to enhance trajectory prediction.

6.4.4 MPCPDP-based Sensing Algorithm

The algorithm for MPCPDP-based sensing is outlined in Algorithm 6.2. Initially, vector $\tilde{\nu}$ is set to zero, and $\tilde{\Omega}$ is initialized based on the LoS distance d_0 , which is set to 10 meters. The vectors λ_r and λ_q are initialized to all ones. Instead of requiring the EC step to undergo a fixed number of iterations, the process is halted when the normalized difference $|\lambda_q^{\text{new}} - \lambda_q^{\text{old}}|^2/|\lambda_q^{\text{new}}|^2$ falls below a tolerance threshold ϵ_1 . Similarly, in the EM algorithm, iterations cease when the normalized difference $|\tilde{\Omega}^{\text{new}} - \tilde{\Omega}^{\text{old}}|^2/|\tilde{\Omega}^{\text{new}}|^2$ is less than another tolerance threshold ϵ_2 . The parameter ϵ_{th} is set to be one percent of the maximum estimated value of $\hat{\Omega}$, i.e., $\epsilon_{\text{th}} = 0.01 \cdot \text{max} |\hat{\Omega}|$.

6.5 Theoretical Performance for the MPCPDP-based Sensing Method

We now demonstrate that the parameter updates in the EM-EC algorithm for the MPCPDP-based sensing method can be interpreted as an approximation of the EM algorithm [120].

The optimization function for EM-EC [121] is defined as:

$$F(q, r, s, \boldsymbol{\theta}) \triangleq -D_{KL}[r \| p(\mathbf{y}_t | \mathbf{h}, \tilde{\boldsymbol{\nu}})] - D_{KL}[s \| p(\mathbf{h}; \tilde{\boldsymbol{\Omega}})] - H(q), \tag{6.64}$$

where $\boldsymbol{\theta} = [\tilde{\Omega}, \tilde{\boldsymbol{\nu}}^T]^T$ and H(q) denotes the entropy of the pdf q. It's also worth noting that -F is commonly referred to as the energy equation in the EM-EC algorithm. However, by incorporating the constraint conditions derived from (6.58), commonly known as moment matching constraints, the optimization problem can be formulated as follows:

$$\hat{\boldsymbol{\theta}} = \arg \max_{\boldsymbol{\theta}} \max_{r,s} \min_{q} F(q, r, s, \boldsymbol{\theta})$$
such to $\mathbb{E}_r[\mathbf{g}(\mathbf{h}); \tilde{\boldsymbol{\nu}}] = \mathbb{E}_q[\mathbf{g}(\mathbf{h})]$ (6.65a)

such to
$$\mathbb{E}_r[\mathbf{g}(\mathbf{h}); \tilde{\boldsymbol{\nu}}] = \mathbb{E}_q[\mathbf{g}(\mathbf{h})]$$

 $\mathbb{E}_s[\mathbf{g}(\mathbf{h}); \tilde{\boldsymbol{\Omega}}] = \mathbb{E}_q[\mathbf{g}(\mathbf{h})].$ (6.65b)

It is important to note that the fixed points of the EM-EC algorithm align with the stationary points of the optimization problem defined in (6.65). The Lagrangian for this constrained optimization in (6.65) is given by:

$$L(\boldsymbol{\theta}, q, r, s, \boldsymbol{\lambda}_1, \boldsymbol{\lambda}_2) \triangleq F(q, r, s, \boldsymbol{\theta}) + \boldsymbol{\lambda}_1(\mathbb{E}_r[\mathbf{g}(\mathbf{h})|\tilde{\boldsymbol{\nu}}] - \mathbb{E}_q[\mathbf{g}(\mathbf{h})]) + \boldsymbol{\lambda}_2(\mathbb{E}_s[\mathbf{g}(\mathbf{h}); \tilde{\boldsymbol{\Omega}}] - \mathbb{E}_q[\mathbf{g}(\mathbf{h})]).$$
(6.66)

In order, we first solve for $q(\mathbf{h}; \lambda_q)$ in (6.66) as

$$\hat{\boldsymbol{\lambda}}_{q} = \underset{\boldsymbol{\lambda}_{q}}{\operatorname{arg\,min}} L(\boldsymbol{\theta}, \hat{\boldsymbol{\lambda}}_{s}, \hat{\boldsymbol{\lambda}}_{r}, \boldsymbol{\lambda}_{q}, \boldsymbol{\lambda}_{1}, \boldsymbol{\lambda}_{2})$$

$$= \underset{\boldsymbol{\lambda}_{q}}{\operatorname{arg\,min}} [\boldsymbol{\lambda}_{q}^{T} - (\boldsymbol{\lambda}_{1} + \boldsymbol{\lambda}_{2})] \mathbb{E}_{q}[\mathbf{g}(\mathbf{h})|\boldsymbol{\lambda}_{q}]. \tag{6.67a}$$

By performing the first-order and second-order derivatives with respect to λ_q , we obtain:

$$\frac{\partial L(\boldsymbol{\theta}, \hat{\boldsymbol{\lambda}}_{s}, \hat{\boldsymbol{\lambda}}_{r}, \boldsymbol{\lambda}_{q}, \boldsymbol{\lambda}_{1}, \boldsymbol{\lambda}_{2})}{\partial \boldsymbol{\lambda}_{q}} \\
= [\boldsymbol{\lambda}_{q}^{T} - (\boldsymbol{\lambda}_{1} + \boldsymbol{\lambda}_{2})^{T}] \left\{ \mathbb{E}_{q}[\mathbf{g}(\mathbf{h})\mathbf{g}(\mathbf{h})^{H}] - \mathbb{E}_{q}[\mathbf{g}(\mathbf{h})]\mathbb{E}_{q}[\mathbf{g}(\mathbf{h})]^{H} \right\}, \qquad (6.68)$$

$$\frac{\partial^{2} L(\boldsymbol{\theta}, \hat{\boldsymbol{\lambda}}_{s}, \hat{\boldsymbol{\lambda}}_{r}, \boldsymbol{\lambda}_{q}, \boldsymbol{\lambda}_{1}, \boldsymbol{\lambda}_{2})}{\partial \boldsymbol{\lambda}_{q} \partial \boldsymbol{\lambda}_{q}^{T}} \\
= \left\{ \mathbb{E}_{q}[\mathbf{g}(\mathbf{h})\mathbf{g}(\mathbf{h})^{H}] - \mathbb{E}_{q}[\mathbf{g}(\mathbf{h})]\mathbb{E}_{q}[\mathbf{g}(\mathbf{h})]^{H} \right\}^{T} > 0, \qquad (6.69)$$

therefore (6.67) is a convex function with only one minimum point $\hat{\lambda}_q$ as:

$$\hat{\lambda}_q = \lambda_1 + \lambda_2. \tag{6.70}$$

Next, we turn to solving for $s(\mathbf{h}; \boldsymbol{\lambda}_s)$ and $r(\mathbf{h}; \boldsymbol{\lambda}_r)$,

$$[\hat{\lambda}_s, \hat{\lambda}_r] = \underset{\lambda_s, \lambda_r}{\arg \max} L(\boldsymbol{\theta}, \lambda_s, \lambda_r, \hat{\lambda}_q, \lambda_1, \lambda_2)$$
(6.71a)

$$= \arg \max_{\boldsymbol{\lambda}_{s}, \boldsymbol{\lambda}_{r}} (\boldsymbol{\lambda}_{1}^{T} - \boldsymbol{\lambda}_{r}^{T}) \mathbb{E}_{r}[\mathbf{g}(\mathbf{h})|\boldsymbol{\lambda}_{r}] + (\boldsymbol{\lambda}_{2}^{T} - \boldsymbol{\lambda}_{s}^{T}) \mathbb{E}_{s}[\mathbf{g}(\mathbf{h})|\boldsymbol{\lambda}_{s}].$$
(6.71b)

Through simple algebraic analysis w.r.t. (6.71), it becomes evident that this function is concave and possesses fixed points as follows:

$$\hat{\lambda}_r = \lambda_1, \quad \hat{\lambda}_s = \lambda_2. \tag{6.72}$$

Table 6.1: Parameters setting for MPCPDP-based Sensing

——————————————————————————————————————	Value
$\frac{1}{G_0}$	1.
N = N	128
f_c	$90~\mathrm{GHz}$
Δf	$60~\mathrm{kHz}$
L	3, 7, 11
v	Ranging from 120 km/h to 360 km/h
SNR (dB)	Range from 0 to 30
$n_1 \text{ (LoS)}$	2.19
$n_{i\neq 1}$ (NLoS)	3.19
m	Ranging from 1 to 10
d_0 (m)	100.
$\tau_i \; (\mathrm{m})$	Random between $3/B$ to $30 B$, minimum gap is $3/B$
$ heta_i$	Random between 0 to 2π
α	10

Finally, $\boldsymbol{\theta} = [\tilde{\boldsymbol{\Omega}}, \tilde{\boldsymbol{\nu}}^T]^T$ can be optimized as:

$$\hat{\boldsymbol{\theta}} = [\hat{d}_0, \hat{\tilde{\boldsymbol{\nu}}}] = \underset{\boldsymbol{\theta}}{\operatorname{arg max}} L(\boldsymbol{\theta}, \hat{\boldsymbol{\lambda}}_s, \hat{\boldsymbol{\lambda}}_r, \hat{\boldsymbol{\lambda}}_q, \boldsymbol{\lambda}_1, \boldsymbol{\lambda}_2)$$

$$= \underset{\tilde{\boldsymbol{\nu}}}{\operatorname{arg max}} \mathbb{E}_r[\ln p(\mathbf{y}_t | \mathbf{h}, \tilde{\boldsymbol{\nu}})] + \underset{\tilde{\boldsymbol{\Omega}}}{\operatorname{arg max}} \mathbb{E}_s[\ln p(\mathbf{h}; \tilde{\boldsymbol{\Omega}})]. \tag{6.73}$$

We then have the following theorem:

Theorem 1: At any fixed points of the EM-EC algorithm, we have:

$$\lambda_1 = \hat{\lambda}_r, \quad \lambda_2 = \hat{\lambda}_s, \quad \hat{\lambda}_q = \lambda_1 + \lambda_2;$$
 (6.74)

$$\hat{q}(\mathbf{h}) = \frac{\exp(\hat{\boldsymbol{\lambda}}_q^T \mathbf{g}(\mathbf{h}))}{\int \exp(\hat{\boldsymbol{\lambda}}_q^T \mathbf{g}(\mathbf{h})) d\mathbf{h}};$$
(6.75)

$$\hat{r}(\mathbf{h}) = \frac{p(\mathbf{y}_t | \mathbf{h}, \hat{\hat{\boldsymbol{\nu}}}) \exp(\hat{\boldsymbol{\lambda}}_r^T \mathbf{g}(\mathbf{h}))}{\int p(\mathbf{y}_t | \mathbf{h}, \hat{\hat{\boldsymbol{\nu}}}) \exp(\hat{\boldsymbol{\lambda}}_r^T \mathbf{g}(\mathbf{h})) d\mathbf{h}};$$
(6.76)

$$\hat{s}(\mathbf{h}) = \frac{p(\mathbf{h}|\hat{\tilde{\mathbf{\Omega}}}) \exp(\hat{\boldsymbol{\lambda}}_s^T \mathbf{g}(\mathbf{h}))}{\int p(\mathbf{h}|\hat{d}_0) \exp(\hat{\boldsymbol{\lambda}}_s^T \mathbf{g}(\mathbf{h})) d\mathbf{h}},$$
(6.77)

where \hat{q} , \hat{r} , and \hat{s} denote the critical points of the Lagrangian in (6.66) that satisfy the moment matching constraints in (6.58). If the EM-EC algorithm converges, its limit points correspond to the local optima of the EM-EC auxiliary function.

6.6 Simulation Results

In this section, we present simulation results to evaluate the performance of our proposed algorithm in estimating range and Doppler shift. Table 6.1 summarizes the key simulation parameters, which are set based on [122]. The effectiveness of our MPCPDP-based sensing method is influenced by several environmental factors, including the number of distinguishable MPCs, signal-to-noise ratio (SNR), Nakagami-m distribution shape parameter m, and target velocity v. The following subsections analyze the impact of these

factors on ranging accuracy. For each scenario, we conducted 1,000 Monte Carlo simulations, computing the root mean square error (RMSE) for range estimation and the normalized RMSE (NRMSE) for the Doppler shift ν_1 of the LoS path. Additionally, we benchmark our results against the state-of-the-art RSS-based ranging method (referred to as RSS-Nakagami in this paper) described in [118]. The thresholds ϵ_1 and ϵ_2 are set to 10^{-3} , and the maximum number of iterations for both the Expectation-Maximization and Expectation-Consistent algorithms is 1000. To further assess the performance, we also include the Genie Bound as a reference. For the ranging task, the Genie Bound assumes perfect knowledge of the channel attenuation and path delays, allowing the range to be estimated under ideal conditions. For Doppler estimation, the perfectly estimated range is substituted into the first-order Taylor expansion model to obtain an idealized Doppler frequency estimate. This bound serves as a theoretical performance limit for our proposed method under the given channel conditions.

6.6.1 Impact of SNR

We fix the target velocity at 240 km/h and examine how SNR affects the LoS range and Doppler estimation of the proposed MPCPDP method. Figs. 6.1 and 6.2 report the range RMSE for m=1 and m=5, respectively, over L=3,7,11 paths. Across all SNRs, MPCPDP consistently outperforms the RSS-Nakagami baseline, and its error monotonically decreases with SNR. The gap between MPCPDP and the Genie Bound shrinks as SNR grows, especially when the number of paths is larger (e.g., L=11), indicating that MPCPDP benefits from richer resolvable multipath in the PDP. Moreover, weaker fading (larger m) further improves performance: under m=5, the MPCPDP curves as a whole shift downward relative to m=1, and at moderate-to-high SNR they closely track the Genie Bound.

Figs. 6.3 and 6.4 show the Doppler NRMSE for m=1 and m=5. The MPCPDP method exhibits a clear SNR-driven improvement: NRMSE steadily reduces from low to high SNR and approaches the Genie Bound in the high-SNR regime. Compared with the range task, the influence of L on Doppler accuracy is much milder—the curves for different L are closely spaced—while the fading severity remains a primary factor: under m=5, MPCPDP achieves uniformly lower NRMSE (on the order of 10^{-2}) across SNRs than under m=1. These observations confirm that the proposed EM–EC-based MPCPDP estimator effectively exploits the PDP structure for both range and Doppler: increasing SNR tightens its performance toward the Genie Bound, larger L chiefly helps range via multipath diversity, and milder fading (larger m) benefits both tasks.

6.6.2 Impact of the Nakagami-m Shape Parameter

We fix the SNR at 10 dB and the target velocity at 240 km/h to examine how the fading shape parameter m affects the estimation accuracy of the proposed MPCPDP method. Fig. 6.5 reports the LoS range RMSE versus m for $L \in \{3,7,11\}$, together with the Genie Bound and the RSS-Nakagami baseline. The MPCPDP curves decrease monotonically with m: milder randomness (larger m) concentrates energy, thus lowering the ranging error. For any fixed m, increasing L further reduces the RMSE, indicating that richer resolvable multipath is beneficial for range estimation under the MPCPDP model. Across the entire m-range, MPCPDP consistently outperforms RSS-Nakagami.

Fig. 6.6 shows the Doppler NRMSE versus m under the same settings. In contrast

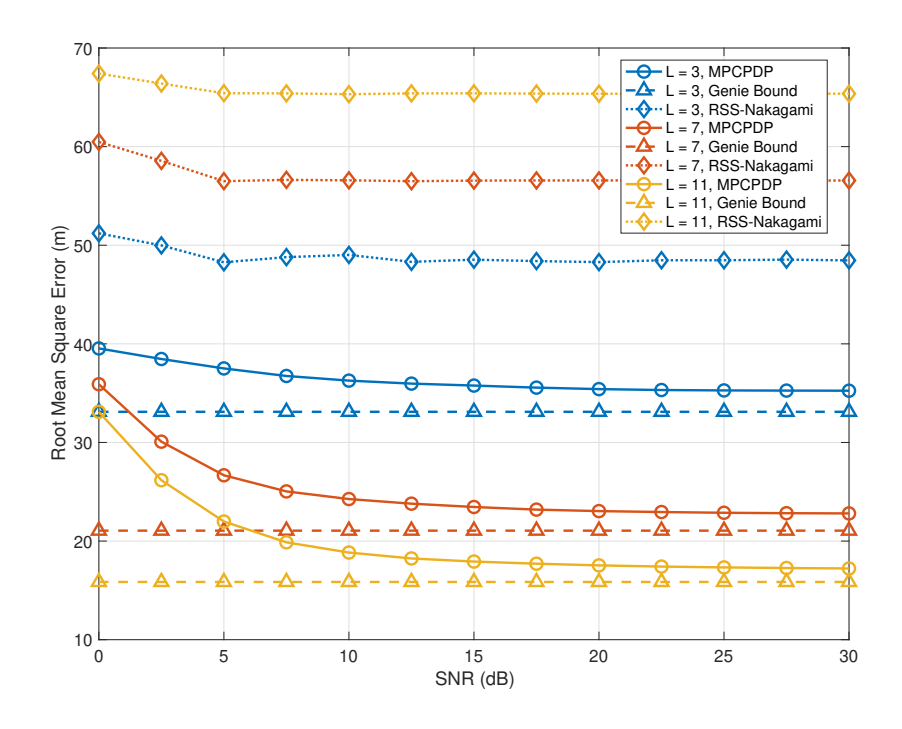


Figure 6.1: m=1: RMSE of Range Estimation vs. SNR for Different Numbers of Paths and Methods

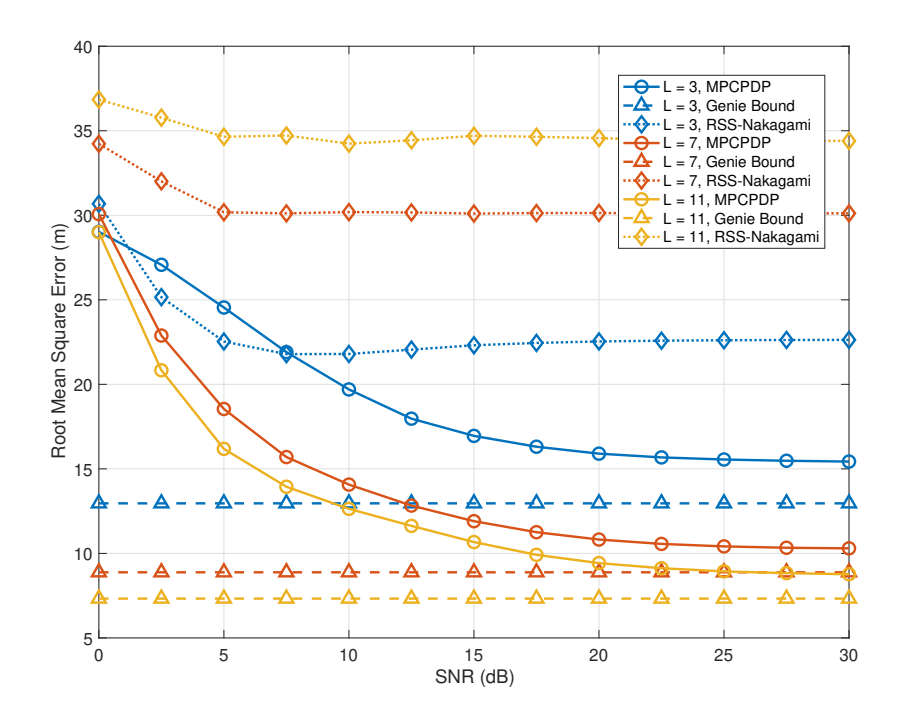


Figure 6.2: m=5: RMSE of Range Estimation vs. SNR for Different Numbers of Paths and Methods

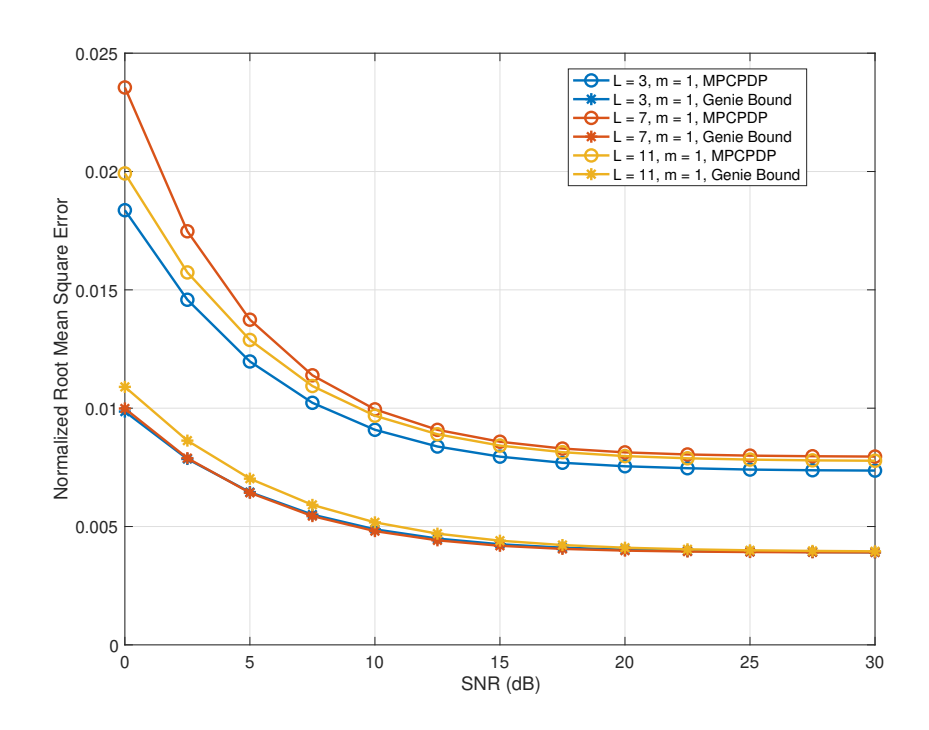


Figure 6.3: m=1: NRMSE of LoS Doppler Shift Estimation vs. SNR for Different Numbers of Paths

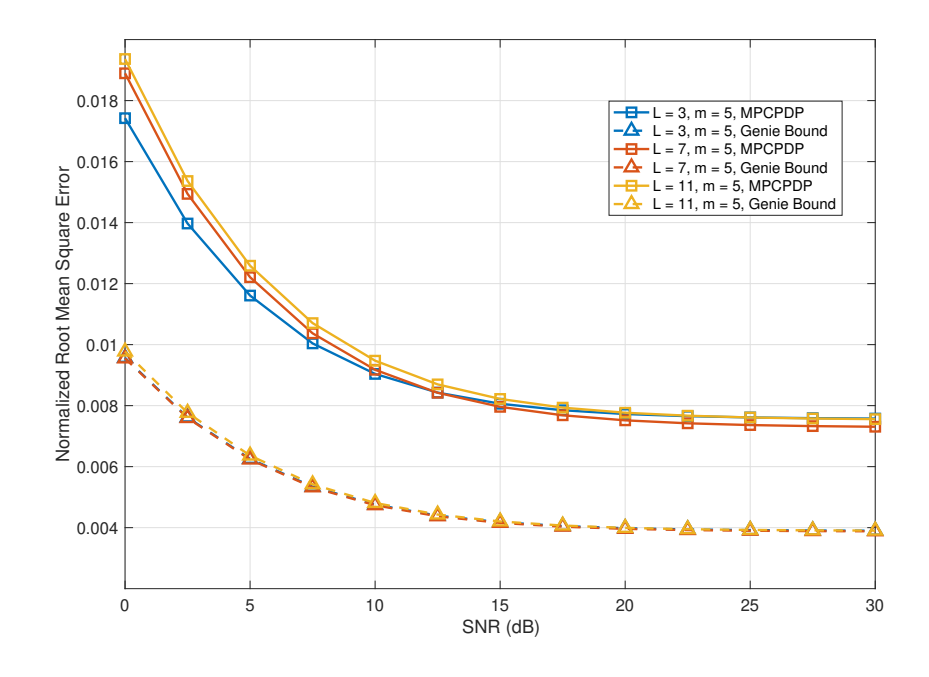


Figure 6.4: m=5: NRMSE of LoS Doppler Shift Estimation vs. SNR for Different Numbers of Paths

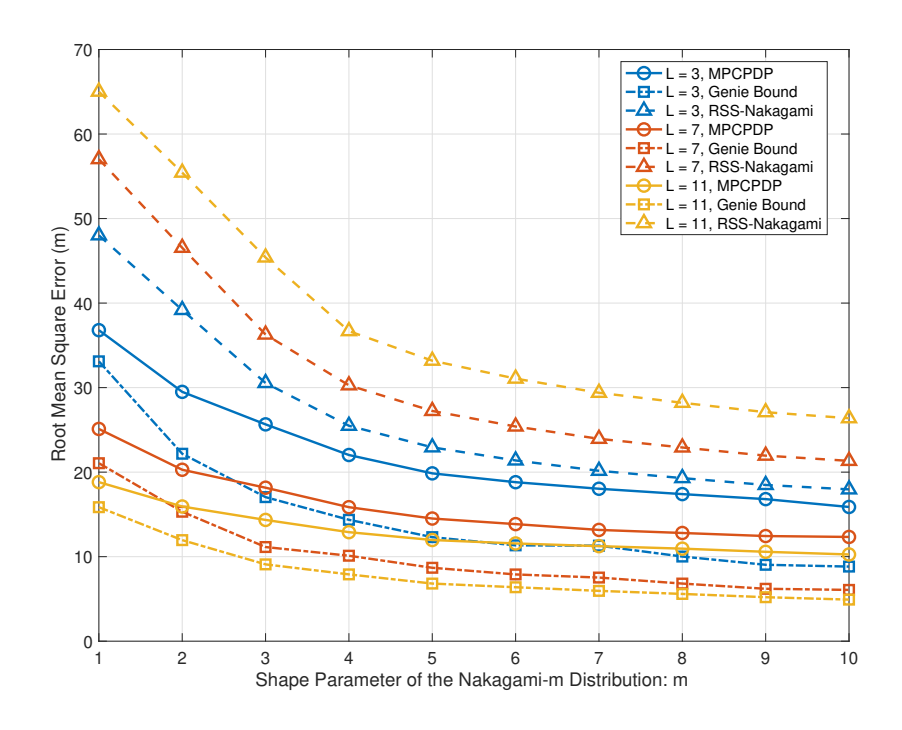


Figure 6.5: RMSE of Range Estimation Across Different Number of Paths and Methods vs. m

to range, the Doppler curves (both MPCPDP and Genie Bound) exhibit only a weak dependence on m, and the performance difference across L=3,7,11 is negligibly small. Moreover, unlike the range results, MPCPDP does not approach the Genie Bound closely at this SNR; a non-trivial gap persists across the tested m values. Overall, while larger m yields a mild improvement in Doppler accuracy, the influence of m and L on Doppler is much smaller than on range. The Genie Bound curves display the same weak sensitivity to m and L, indicating that the observed behavior is an inherent property of the signal/measurement model (finite observation length and phase noise at 10 dB) rather than a deficiency of the proposed EM-EC estimator.

6.6.3 Impact of Absolute Velocity (v)

We fix the SNR at 10 dB and investigate how the absolute velocity of the target influences the LoS range and Doppler estimation performance of the proposed MPCPDP method. Fig. 6.7 presents the RMSE of range estimation versus v for $m \in \{1,5\}$ and $L \in \{3,7,11\}$. For all settings, range RMSE increases gradually as velocity grows. This degradation is attributed to the reduced accuracy of the first-order Taylor approximation used in the Doppler model: at higher Doppler shifts, the linearization around zero introduces non-negligible modeling error, which propagates into the joint delay–Doppler estimation and slightly degrades the recovered LoS delay.

Fig. 6.8 shows that the NRMSE of LoS Doppler estimation first decreases with velocity and then increases for all tested m and L, with only minor differences across these parameters. The initial drop occurs because the normalized error is dominated by noise at low velocities; as the true Doppler shift ν increases, the same absolute estimation variance translates into a smaller relative (normalized) error, and the first-order Taylor

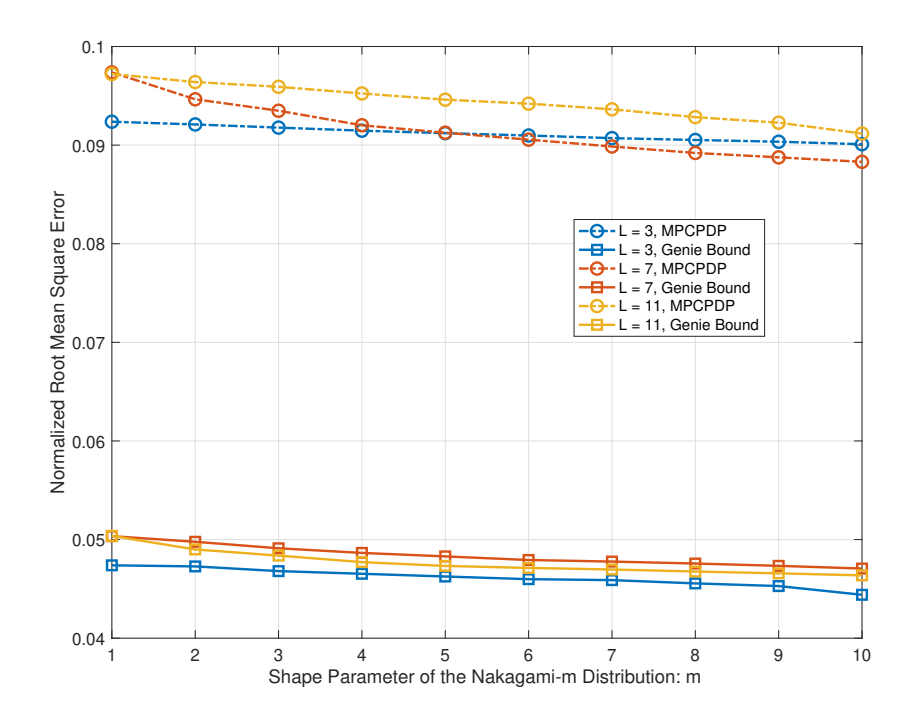


Figure 6.6: NRMSE of LoS Doppler Shift Estimation Across Different Number of Paths of Paths vs. m.

approximation remains sufficiently accurate. At higher velocities, however, the neglected higher-order terms in the Doppler phase model grow quadratically with ν , reducing the validity of the linearization and introducing model bias. This bias eventually dominates, causing the NRMSE to rise again. The minimal impact of L arises because Doppler estimation relies primarily on the phase evolution of the dominant LoS path, while m has limited influence since it affects amplitude fading rather than the phase dynamics that govern Doppler estimation.

6.6.4 Simulation Conclusions

Based on experimental simulations varying SNR values, velocity v, shape parameter m, and the number of NLoS paths, our method has shown strong performance across diverse and complex environments. Notably, the number of NLoS paths and the shape parameter m are critical factors, significantly influencing ranging estimation accuracy. As the number of NLoS paths increases, our MPCPDP-based sensing method improves in ranging accuracy, while Doppler shift estimation almost remains consistent. Additionally, an increase in m reduces the variance of the fading channel, which enhances our method's performance. Although higher velocities slightly reduce the performance of our sensing method, the overall impact is minimal. These results underscore the effectiveness of our MPCPDP-based sensing in numerical simulations under the OFDM system, particularly when considering Doppler shifts.

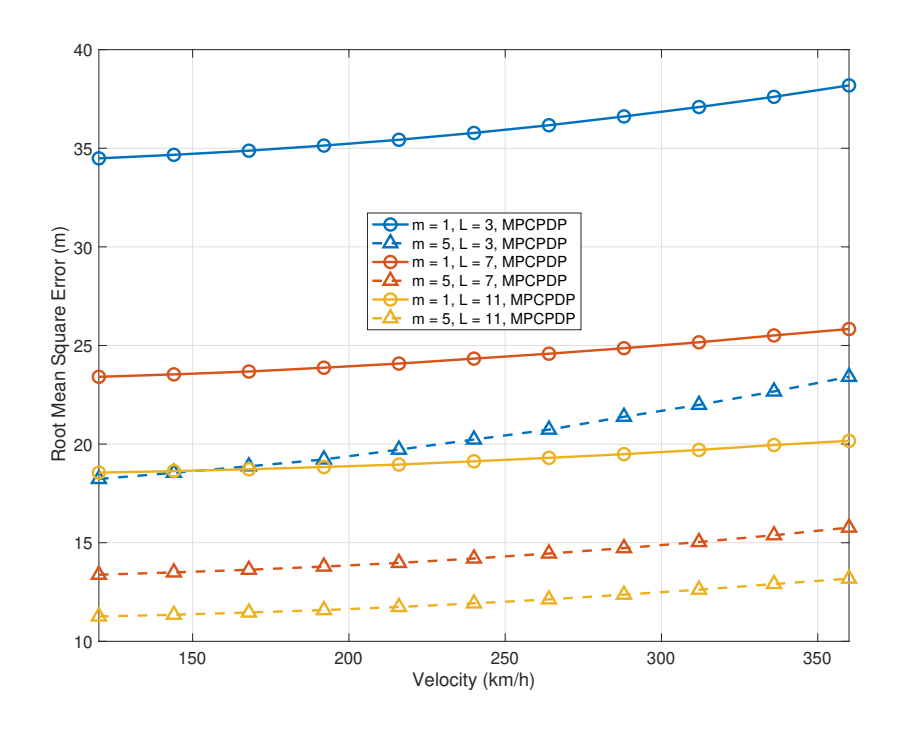


Figure 6.7: RMSE of Range Estimation Across Different Number of Paths vs. Velocity v

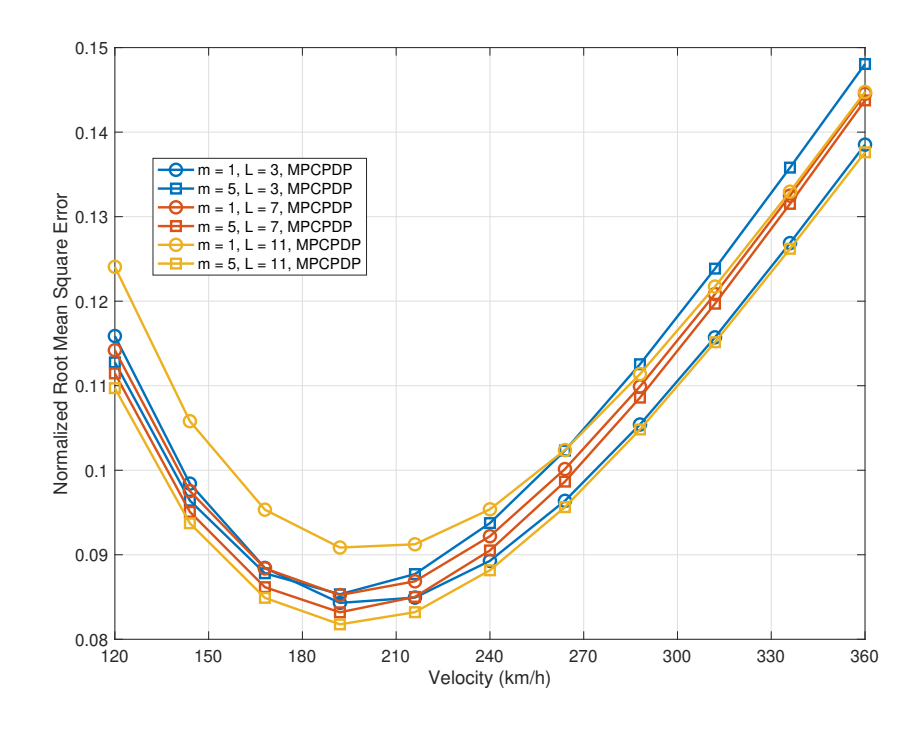


Figure 6.8: NRMSE of LoS Doppler Shift Estimation Across Different Number of Paths vs. Velocity \boldsymbol{v}

6.7 Conclusions

This chapter addressed joint range and Doppler sensing in OFDM systems under doubly fractional delay–Doppler conditions. We formulated a time-domain MPCPDP-based model with an oversampled delay grid and a circular Nakagami-m envelope plus uniform phase prior, and proposed an EM-EC algorithm that simultaneously estimates largescale fading hyperparameters, recovers the sparse delay–Doppler structure (separating LoS/NLoS), and extracts the LoS Doppler for velocity inference; we further established the algorithm's fixed-point conditions to clarify its convergence behavior. Simulations demonstrated that, across a wide range of SNRs, path counts, fading severities, and target speeds, the proposed method achieves accurate ranging and Doppler estimation and generally outperforms an RSS-Nakagami baseline; in particular, ranging error decreases markedly with SNR and larger L, and approaches a Genie Bound in favorable conditions, while Doppler NRMSE exhibits weak dependence on L and m and follows a characteristic decrease-then-increase trend versus speed due to the transition from noise-dominated to model-mismatch-dominated regimes under first-order Doppler linearization. Overall, these results confirm the practicality of MPCPDP-based sensing for integrated sensing and communication with low hardware complexity. Future work will incorporate higherorder Doppler modeling to mitigate high-speed bias, consider non-Gaussian disturbances and model uncertainties, and validate the approach on real measurements and prototype ISAC platforms.

Chapter 7

Conclusion and Future Work

In this dissertation, we have systematically explored high-precision ranging techniques in multipath-rich wireless communication environments, leveraging the Power Delay Profile (PDP) derived from Channel State Information (CSI). The work focused on addressing key challenges in accurate distance estimation under complex channel conditions, particularly in the context of next-generation integrated sensing and communication (ISAC) systems. Through theoretical modeling, algorithm development, and comprehensive simulation studies, several important contributions have been made.

First, we proposed a high-resolution PDP estimation framework that combines sparse recovery methods with off-grid modeling techniques. This approach enables more accurate delay discrimination and path separation, effectively overcoming limitations of conventional PDP estimation in low signal-to-noise ratio (SNR) scenarios and dense multipath propagation environments. Second, we established a statistical mapping between PDP energy and physical distance, allowing for robust and efficient ranging without requiring additional sensing overhead. This approach extends the applicability of communication-centric signals to environmental sensing tasks, laying the groundwork for future ISAC deployment.

Furthermore, recognizing the need to operate reliably under mobility, we developed a time-domain OFDM sensing framework for doubly fractional delay—Doppler scenarios. We constructed an oversampled delay grid to represent fractional delays and modeled multipath amplitudes with a Nakagami-m envelope and uniformly distributed phase. A computationally efficient EM—EC algorithm was introduced to jointly estimate large-scale fading hyperparameters, recover the sparse multipath structure (separating LoS/NLoS), and extract the LoS range and Doppler from a single pilot block under a first-order Doppler linearization. We also characterized the algorithm's fixed points to clarify convergence behavior and employed a Genie Bound to benchmark achievable performance. Extensive numerical simulations validate the effectiveness of these methods, showing significant improvements over existing state-of-the-art approaches in terms of delay resolution, ranging accuracy, and robustness to mobility.

Despite these promising contributions, several challenges and open questions remain. The proposed algorithms have been validated in simulation environments that approximate real-world conditions, but practical implementation in hardware is an essential next step. Future work will focus on experimental verification, including the impact of hardware impairments, synchronization offsets, and environmental uncertainties. Additionally, while this dissertation has primarily addressed one-dimensional ranging, extending the framework to three-dimensional localization and tracking—via multi-receiver/sensor

fusion—will be crucial for robust positioning in dense multipath and non-line-of-sight (NLoS) conditions. Another important direction is the theoretical characterization of performance limits for the proposed framework when classical Cramér—Rao Bounds (CRBs) are not directly applicable; alternative bounds or approximate analyses will help quantify fundamental accuracy and guide algorithmic design. Finally, refining Doppler modeling beyond first-order linearization (e.g., higher-order expansions or bias-compensation schemes), stress-testing robustness under non-Gaussian disturbances, and developing real-time implementations will further enhance estimation precision in realistic propagation conditions.

Appendix A

A.1 Derivation of Nakagami-m Posterior Mean and Variance

In this appendix, we will derive the expressions for \hat{a}_i and τ_{a_i} in (5.35a) and (5.35b) based on the pdf $p_{a_i}(a_i|\Omega_i)$. In the EM-ReVAMP algorithm presented in Algorithm 5.2, we have the following expressions:

$$\hat{a}_i = \frac{\int a_i p_{a_i}(a_i | \Omega_i) \mathcal{CN}(a_i; r_i, \tau_{r_i}) da_i}{\int p_{a_i}(a_i | \Omega_i) \mathcal{CN}(a_i; r_i, \tau_{r_i}) da_i}; \tag{A.1a}$$

$$\tau_{a_i} = \frac{\int |a_i - \hat{a}_i|^2 p_{a_i}(a_i | \Omega_i) \mathcal{CN}(a_i; r_i, \tau_{r_i}) da_i}{\int p_{a_i}(a_i | \Omega_i) \mathcal{CN}(a_i; r_i, \tau_{r_i}) da_i},$$
(A.1b)

where Z_i is defined as:

$$Z_i = \int p_{a_i}(a_i|\Omega_i) \mathcal{CN}(a_i; r_i, \tau_{r_i}) da_i.$$
 (A.2)

For calculating Z_i , we have the integral:

$$Z_{i} = \int \frac{m^{m} |a_{i}|^{2m-2}}{\pi \Gamma(m) \Omega_{i}^{m}} \exp\left[-\frac{m |a_{i}|^{2}}{\Omega_{i}}\right] \times \frac{1}{\pi \tau_{r_{i}}} \exp\left(-\frac{(a_{i} - r_{i})^{*}(a_{i} - r_{i})}{\tau_{r_{i}}}\right) da_{i}.$$
(A.3)

Inside the integral, we have:

$$\int_0^{2\pi} \exp\left(\frac{2}{\tau_{r_i}}(|r_i|r\cos(\phi - \phi_{r_i}))\right) d\phi = 2\pi J_0\left(j\frac{2}{\tau_{r_i}}r|r_i|\right),\tag{A.4}$$

where $J_0(x)$ is the Bessel function of the first kind. By incorporating the equations and clarifying the expressions, the derivation of Z_i becomes more comprehensible. Moreover, we can simplify the remaining integral using the confluent hypergeometric function:

$$\int_{0}^{+\infty} x^{\mu} \exp(-\alpha x^{2}) J_{v}(\beta x) dx$$

$$= \frac{\beta^{v} \Gamma(0.5(v + \mu + 1))}{2^{v+1} \alpha^{0.5(v + \mu + 1)} \Gamma(v + 1)^{1}} F_{1}\left(0.5(v + \mu + 1); v + 1; -\frac{\beta^{2}}{4\alpha}\right), \tag{A.5}$$

where ${}_{1}F_{1}(a;b;z)$ is the confluent hypergeometric function. By utilizing these results, we can evaluate Z_{i} and proceed with the derivation of \hat{a}_{i} and $\tau_{a_{i}}$. Simplifying the integral and applying the properties of the confluent hypergeometric function, we obtain:

$$\int_{0}^{+\infty} r^{2m-1} \exp\left(-\left(\frac{m}{\Omega_{i}} + \frac{1}{\tau_{r_{i}}}\right) r^{2}\right) J_{0}\left(j\frac{2}{\tau_{r_{i}}} r | r_{i}|\right) dr
= \frac{\Gamma(m)}{2\left(\frac{m}{\Omega_{i}} + \frac{1}{\tau_{r_{i}}}\right)^{m} {}_{1}F_{1}(m; 1; \frac{\Omega_{i} | r_{i}|^{2}}{m\tau_{r_{i}}^{2} + \tau_{r_{i}}\Omega_{i}}).$$
(A.6)

Based on the previous results, we can express the Z_i as follows:

$$Z_{i} = \frac{m^{m}}{\pi \Omega_{i}^{m} \tau_{r_{i}} \left(\frac{m}{\Omega_{i}} + \frac{1}{\tau_{r_{i}}}\right)^{m}} {}_{1}F_{1}(m; 1; \frac{\Omega_{i} |r_{i}|^{2}}{m \tau_{r_{i}}^{2} + \tau_{r_{i}} \Omega_{i}}). \tag{A.7}$$

Then for $\int a_i p_i(a_i) \mathcal{CN}(a_i; r_i, \tau_{r_i}) da_i$, it can be written as:

$$\int a_{i}p_{i}(a_{i})\mathcal{C}\mathcal{N}(a_{i};r_{i},\tau_{r_{i}})da_{i} = \frac{m^{m}}{\pi^{2}\Gamma(m)\Omega_{i}^{m}\tau_{r_{i}}} \int_{0}^{+\infty} \int_{0}^{2\pi} (\cos\phi + j\sin\phi) \exp\left\{\frac{2}{\tau_{r_{i}}}[|r_{i}|r\cos(\phi - \phi_{r_{i}})]\right\} d\phi r^{2m-1} \exp\left[-(\frac{m}{\Omega_{i}} + \frac{1}{\tau_{r_{i}}})r^{2}\right] r dr.$$
(A.8)

Inside this expression, we have the following intermediate results:

$$\int_{0}^{2\pi} (\cos \phi + j \sin \phi) \exp(\frac{2}{\tau_{r_{i}}} (|r_{i}|r \cos(\phi - \phi_{r_{i}}))) d\phi
= -j2\pi \exp(j\phi_{r_{i}}) J_{1}(j\frac{2r|r_{i}|}{\tau_{r_{i}}}),$$
(A.9)

and

$$\int_{0}^{+\infty} r^{2m} \exp\left(-\left(\frac{m}{\Omega_{i}} + \frac{1}{\tau_{r_{i}}}\right)r^{2}\right) J_{1}\left(j\frac{2}{\tau_{r_{i}}}r|r_{i}|\right) dr
= \frac{j|r_{i}|\Gamma(m+1)}{2\tau_{r_{i}}\left(\frac{m}{\Omega_{i}} + \frac{1}{\tau_{r_{i}}}\right)^{(m+1)} {}_{1}F_{1}(m+1;2;\frac{\Omega_{i}|r_{i}|^{2}}{m\tau_{r_{i}}^{2} + \tau_{r_{i}}\Omega_{i}}).$$
(A.10)

Thus, $\int a_i p_i(a_i) \mathcal{CN}(a_i; r_i, \tau_{r_i}) da_i$ can be expressed as follows:

$$\int a_{i}p_{i}(a_{i})\mathcal{CN}(a_{i}; r_{i}, \tau_{r_{i}})da_{i} = \frac{m^{m+1}|r_{i}|}{\pi\Omega_{i}^{m}\tau_{r_{i}}^{2}(\frac{m}{\Omega_{i}} + \frac{1}{\tau_{r_{i}}})^{(m+1)}} \times \exp(j\phi_{r_{i}})_{1}F_{1}(m+1; 2; \frac{\Omega_{i}|r_{i}|^{2}}{m\tau_{r_{i}}^{2} + \tau_{r_{i}}\Omega_{i}}).$$
(A.11)

For $\int a_i^* a_i p_i(a_i) \mathcal{CN}(a_i; r_i, \tau_{r_i}) da_i$, we can compute it as follows:

$$\begin{split} \int a_{i}^{*}a_{i}p_{i}(a_{i})\mathcal{CN}(a_{i};r_{i},\tau_{r_{i}})da_{i} &= \frac{m^{m}}{\pi^{2}\,\Gamma(m)\,\Omega_{i}^{m}\,\tau_{r_{i}}} \int_{0}^{+\infty} \int_{0}^{2\pi} \\ &\exp\left\{\frac{2}{\tau_{r_{i}}}[|r_{i}|r\cos(\phi-\phi_{r_{i}})]\right\}d\phi\,r^{2m} \exp\left[-(\frac{m}{\Omega_{i}}+\frac{1}{\tau_{r_{i}}})r^{2}\right]rdr. \end{split} \tag{A.12}$$

Inside this expression, we have the following intermediate results:

$$\int_0^{2\pi} \exp(\frac{2}{\tau_{r_i}}(|r_i|r\cos(\phi - \phi_{r_i})))d\phi = 2\pi J_0(j\frac{2}{\tau_{r_i}}r|r_i|),\tag{A.13}$$

and

$$\int_{0}^{+\infty} r^{2m+1} \exp\left(-\left(\frac{m}{\Omega_{i}} + \frac{1}{\tau_{r_{i}}}\right)r^{2}\right) J_{0}\left(j\frac{2}{\tau_{r_{i}}}r|r_{i}|\right) dr = \frac{\Gamma(m+1)}{2\left(\frac{m}{\Omega_{i}} + \frac{1}{\tau_{r_{i}}}\right)^{(m+1)}} {}_{1}F_{1}(m+1;1;\frac{\Omega_{i}|r_{i}|^{2}}{m\tau_{r_{i}}^{2} + \tau_{r_{i}}\Omega_{i}}).$$
(A.14)

Therefore, $\int a_i a_i^* p_i(a_i) \mathcal{CN}(a_i; r_i, \tau_{r_i}) da_i$ can be given as:

$$\int a_{i} a_{i}^{*} p_{i}(a_{i}) \mathcal{C} \mathcal{N}(a_{i}; r_{i}, \tau_{r_{i}}) da_{i}
= \frac{m^{(m+1)}}{\pi \Omega_{i}^{m} \tau_{r_{i}} (\frac{m}{\Omega_{i}} + \frac{1}{\tau_{r_{i}}})^{(m+1)}} {}_{1} F_{1}(m+1; 1; \frac{\Omega_{i} |r_{i}|^{2}}{m \tau_{r_{i}}^{2} + \tau_{r_{i}} \Omega_{i}}).$$
(A.15)

Thus, we can obtain the expressions for $\mathbb{E}[a_i]$ and $\mathbb{E}[a_i a_i^*]$ as follows:

$$\mathbb{E}[a_i] = \frac{m\Omega_i r_i}{m\tau_{r_i} + \Omega_i} \frac{{}_{1}F_1(m+1; 2; \frac{\Omega_i |r_i|^2}{m\tau_{r_i}^2 + \tau_{r_i} d_0})}{{}_{1}F_1(m; 1; \frac{\Omega_i |r_i|^2}{m\tau_{r_i}^2 + \tau_{r_i} \Omega_i})};$$
(A.16a)

$$\mathbb{E}[a_i a_i^*] = \frac{m\Omega_i \tau_{r_i}}{m\tau_{r_i} + \Omega_i} \frac{{}_{1}F_1(m+1; 1; \frac{\Omega_i |r_i|^2}{m\tau_{r_i}^2 + \tau_{r_i}\Omega_i})}{{}_{1}F_1(m; 1; \frac{\Omega_i |r_i|^2}{m\tau_{r_i}^2 + \tau_{r_i}\Omega_i})}.$$
(A.16b)

Finally, we obtain the expressions for \hat{a}_i and τ_{a_i} as follows:

$$\hat{a}_{i} = \frac{m\Omega_{i}r_{i}}{m\tau_{r_{i}} + \Omega_{i}} \frac{{}_{1}F_{1}(m+1; 2; \frac{\Omega_{i}|r_{i}|^{2}}{m\tau_{r_{i}}^{2} + \tau_{r_{i}}\Omega_{i}})}{{}_{1}F_{1}(m; 1; \frac{\Omega_{i}|r_{i}|^{2}}{m\tau_{r_{i}}^{2} + \tau_{r_{i}}\Omega_{i}})};$$
(A.17a)

$$\tau_{a_i} = \frac{m\Omega_i \tau_{r_i}}{m\tau_{r_i} + \Omega_i} \frac{{}_{1}F_1(m+1; 1; \frac{\Omega_i |r_i|^2}{m\tau_{r_i}^2 + \tau_{r_i}\Omega_i})}{{}_{1}F_1(m; 1; \frac{\Omega_i |r_i|^2}{m\tau_{r_i}^2 + \tau_{r_i}\Omega_i})} - \hat{a}_i \hat{a}_i^*.$$
(A.17b)

A.2 List of Publications

The following publications have resulted from the research conducted in this dissertation:

Journal Articles

 Fangqing Xiao and Dirk Slock, "Multipath Component Power Delay Profile Based Ranging," *IEEE Journal on Selected Topics in Signal Processing*, DOI: 10.1109 JSTSP.2024.3491580.

Conference Papers

- Fangqing Xiao and Dirk Slock, "Multipath Component Power Delay Profile Based Ranging," IEEE Journal on Selected Topics in Signal Processing, DOI: 10.1109/JSTSP.2024.349158
- 2. Fangqing Xiao and Dirk Slock, "Performance analysis of hyperparameter optimization in sparse Bayesian learning via Stein's unbiased risk estimator," *EUSIPCO* 2025, Palermo, Italy, Sept. 2025.
- 3. Fangqing Xiao, Xiyao Zhou, Zunqi Li, Hongwei Hou and Dirk Slock, "High-Precision LoS Localization Using Composite Nakagami-m Log-Normal Model," *IEEE Mediter-ranean Conference on Communications and Networking (Meditcom)*, July 2025, Nice, France.
- 4. Fangqing Xiao and Dirk Slock, "Single Snapshot Direction of Arrival Estimation Using the EP-SURE-SBL Algorithm," *IEEE ICASSP*, 2025, Hyderabad, India.
- 5. Fangqing Xiao and Dirk Slock, "Breaking the Gaussian Barrier: Leveraging ReG-VAMP to Extend EKF, SOEKF, and IEKF," Asilomar Conference on Signals, Systems, and Computers, Oct. 2024, Pacific Grove, USA.
- 6. Zilu Zhao, Fangqing Xiao and Dirk Slock, "Extrinsics and Linearized CWCU MMSE Estimation as in GAMP," Asilomar Conference on Signals, Systems, and Computers, Oct. 2024, Pacific Grove, USA.
- 7. Mehdi Ashury et al., "Joint Estimation of Channel, Range, and Doppler for FMCW Radar with Sparse Bayesian Learning," *IEEE SPAWC*, Sept. 2024, Lucca, Italy.
- 8. Fangqing Xiao and Dirk Slock, "Fast Expectation Propagation for Sparse Signal Reconstruction with a Fourier Dictionary," *IEEE PIMRC*, Sept. 2024, Valencia, Spain.
- 9. Fangqing Xiao and Dirk Slock, "Towards Hyperparameter Optimizing of Sparse Bayesian Learning Based on Stein's Unbiased Risk Estimator," *IEEE ISIT*, Learn to Compress Workshop, July 2024, Athens, Greece.
- 10. Fangqing Xiao and Dirk Slock, "Parameter Estimation via Expectation Maximization Expectation Consistent Algorithm," *IEEE ICASSP*, Apr. 2024, Seoul, Korea.
- 11. Zilu Zhao, Fangqing Xiao and Dirk Slock, "Vector Approximate Message Passing for Not So Large n.i.i.d. Generalized I/O Linear Models," *IEEE ICASSP*, Apr. 2024, Seoul, Korea.
- 12. Fangqing Xiao, Zilu Zhao and Dirk Slock, "Power Delay Profile Based Ranging via Approximate EM-reVAMP," *IEEE CAMAD*, Nov. 2023, Edinburgh, UK.
- 13. Zilu Zhao, Fangqing Xiao and Dirk Slock, "Approximate Message Passing for Not So Large NIID Generalized Linear Models," *IEEE SPAWC*, Sept. 2023, Shanghai, China.
- 14. Fangqing Xiao and Dirk Slock, "A Cramér–Rao Bound for Indoor Power Delay Profile Based Ranging," *IPIN-WiP*, Sept. 2023, Nuremberg, Germany.

Poster Presentations

1. Fangqing Xiao, Zilu Zhao and Dirk Slock, "Channel State Information Based Ranging via EM-reVAMP Algorithm," *IEEE SECON*, Sept. 2023, Madrid, Spain.

Submitted Manuscripts

1. Fangqing Xiao, Zunqi Li and Dirk Slock, "Multipath Component Power Delay Profile Based Joint Range and Doppler Estimation for AFDM-ISAC Systems," submitted to Arxiv.

Bibliography

- [1] G. Fettweis and S. Alamouti, "5g: Personal mobile internet beyond what cellular did to telephony," *IEEE Communications Magazine*, vol. 52, no. 2, pp. 140–145, 2014.
- [2] ITU-R, "Imt vision framework and overall objectives of the future development of imt for 2020 and beyond," ITU, Tech. Rep. M.2083-0, Sep 2015.
- [3] Ericsson, "Ericsson Mobility Report," https://www.ericsson.com/en/reports-and-papers/mobility-report, November 2023.
- [4] A. Gupta and R. K. Jha, "A survey of 5g network: Architecture and emerging technologies," *IEEE Access*, vol. 3, pp. 1206–1232, 2015.
- [5] Verizon, "What are embb, urllc and mmtc? 5g technology," https://www.verizon.com/about/news/5g-understanding-embb-urllc-mmtc, 2023, accessed: 2025-05-26.
- [6] 5G Americas, "Global 5g connections reach nearly two billion," https://www.5gamericas.org/global-5g-connections-reaches-nearly-two-billion/, 2024, accessed: 2025-05-26.
- [7] IPLOOK, "Global 5g connections surpass 2 billion: A milestone for the industry," https://www.iplook.com/info/global-5g-connections-surpass-2-billion-a-milestone-for-the-industry-i00468i1.html, 2025, accessed: 2025-05-26.
- [8] PwC, "The global economic impact of 5g. powering your tomorrow," https://www.pwc.com/gx/en/tmt/5g/global-economic-impact-5g.pdf, 2020, accessed: 2025-05-26.
- [9] 6G Flagship, "6g wireless summit 2019 archive," https://www.6gsummit.com/6g-summit-2019-archive/, 2019, accessed: 2025-05-26.
- [10] Nokia, "Nokia to lead the eu's 6g project hexa-x," https://www.nokia.com/newsroom/nokia-to-lead-the-eus-6g-project-hexa-x/, 2020, accessed: 2025-05-26.
- [11] Hexa-X-II, "Hexa-x-ii european level 6g flagship project," https://hexa-x-ii.eu/, 2023, accessed: 2025-05-26.
- [12] International Telecommunication Union, "Imt towards 2030 and beyond (imt-2030)," https://www.itu.int/en/itu-r/study-groups/rsg5/rwp5d/imt-2030/pages/default.aspx, 2023, accessed: 2025-05-26.
- [13] IMT-2030 (6G) Promotion Group, "Introduction on imt-2030(6g) promotion group in china," https://hexa-x-ii.eu/wp-content/uploads/2024/02/ Introduction-on-IMT-20306G-PG-20240201.pdf, 2024, accessed: 2025-05-26.

- [14] 3GPP, "Release 18 3gpp," https://www.3gpp.org/specifications-technologies/releases/release-18, 2024, accessed: 2025-05-26.
- [15] W. Saad, M. Bennis, and M. Chen, "A vision of 6g wireless systems: Applications, trends, technologies, and open research problems," *IEEE Network*, vol. 34, no. 3, pp. 134–142, 2020.
- [16] M. Giordani, M. Polese, M. Mezzavilla, S. Rangan, and M. Zorzi, "Toward 6g networks: Use cases and technologies," *IEEE Communications Magazine*, vol. 58, no. 3, pp. 55–61, 2020.
- [17] Hexa-X-II Consortium, "6g vision, use cases and key societal values," https://hexa-x-ii.eu/wp-content/uploads/2023/06/Hexa-X-II-D1.1.pdf, 2023, accessed: 2025-05-26.
- [18] M. Latva-aho and K. Leppänen, "Key drivers and research challenges for 6g ubiquitous wireless intelligence," https://www.6gflagship.com/wp-content/uploads/2020/09/Key-Drivers-and-Research-Challenges-for-6G.pdf, 2020, accessed: 2025-05-26.
- [19] International Telecommunication Union (ITU), "Imt towards 2030 and beyond: Framework and overall objectives," https://www.itu.int/en/ITU-R/study-groups/rsg5/rwp5d/imt-2030/Pages/default.aspx, 2023, accessed: 2025-05-26.
- [20] F. Liu, Y. Cui, C. Masouros, J. Xu, T. X. Han, Y. C. Eldar, and S. Buzzi, "Integrated sensing and communications: Toward dual-functional wireless networks for 6g and beyond," *IEEE Journal on Selected Areas in Communications*, vol. 40, no. 6, pp. 1728–1767, 2022.
- [21] Smart Networks and Services Joint Undertaking (SNS JU), "6g kpis definitions and target values," SNS JU, Tech. Rep., February 2025. [Online]. Available: https://smart-networks.europa.eu/wp-content/uploads/2025/02/white-paper-kpis_17_2_2025_for-rel_.pdf
- [22] Green6G Project Consortium, "Green6G: Greener Communications for 6G," https://green6g.eu, 2023, accessed: 2025-05-26.
- [23] RISE-6G Consortium, "RISE-6G: Reconfigurable Intelligent Sustainable Environments for 6G Wireless Networks," https://cordis.europa.eu/project/id/101017011, 2023, funded by the European Union's Horizon 2020 Programme. Accessed: 2025-05-26.
- [24] A. Liu, Z. Huang, M. Li, Y. Wan, W. Li, T. X. Han, C. Liu, R. Du, D. K. P. Tan, J. Lu et al., "A survey on fundamental limits of integrated sensing and communication," *IEEE Commun. Surveys & Tutorials*, vol. 24, no. 2, pp. 994–1034, 2022.
- [25] A. Bayesteh, J. He, Y. Chen, P. Zhu, J. Ma, A. W. Shaban, Z. Yu, Y. Zhang, Z. Zhou, and G. Wang, "Integrated sensing and communication (isac) from concept to practice," Huawei Tech, 2022. [Online]. Available: https://www.huawei.com/en/huaweitech/future-technologies/integrated-sensing-communication-concept-practice
- [26] Ericsson, "Integrated sensing and communication (isac)," Ericsson Blog, 2024. [Online]. Available: https://www.ericsson.com/en/blog/2024/6/integrated-sensing-and-communication

- [27] X. Cheng, J. Tang, and et al., "A survey on integrated sensing and communication in 6g: Current trends and open challenges," *IEEE Internet of Things Journal*, vol. 8, no. 6, pp. 4315–4336, 2021.
- [28] D. Zhang, D. Zhang, H. Wang, and R. Zhang, "Csi-based passive human sensing for internet of things: A survey," *IEEE Internet of Things Journal*, vol. 9, no. 5, pp. 3764–3785, 2022.
- [29] H. Abdelaziz and J. A. Nossek, "High-resolution delay estimation using sparse pdp reconstruction in massive mimo systems," *IEEE Transactions on Signal Processing*, vol. 70, pp. 3043–3058, 2022.
- [30] F. Xiao and D. T. M. Slock, "A cramér—rao bound for indoor power delay profile based ranging," in 13th International Conference on Indoor Positioning and Indoor Navigation (IPIN), 2023.
- [31] Y. He, W. Xu, and W. Yang, "Robust and low-complexity pdp estimation under dynamic multipath channels," *IEEE Transactions on Wireless Communications*, vol. 22, no. 4, pp. 2511–2524, 2023.
- [32] S. Hu, Z. Wang, and et al., "Off-grid sparse channel estimation and path parameter extraction for mimo-ofdm systems," *IEEE Transactions on Wireless Communications*, vol. 20, no. 3, pp. 1542–1557, 2021.
- [33] A. Bemani, N. Ksairi, and M. Kountouris, "Integrated sensing and communications with affine frequency division multiplexing," arXiv preprint arXiv:2402.16468, 2024.
- [34] Y. Gu, A. Lo, and I. Niemegeers, "A Survey of Indoor Positioning Systems for Wireless Personal Networks," *IEEE Communications Surveys & Tutorials*, vol. 11, no. 1, pp. 13–32, 2009.
- [35] A. A. D'Amico, U. Mengali, and L. Taponecco, "Cramer-Rao Bound for Clock Drift in UWB Ranging Systems," *IEEE Wireless Communications Letters*, vol. 2, no. 6, pp. 591–594, 2013.
- [36] E. Leitinger, M. Fröhle, P. Meissner, and K. Witrisal, "Multipath-Assisted Maximum-Likelihood Indoor Positioning Using UWB Signals," in 2014 IEEE International Conference on Communications Workshops (ICC), 2014, pp. 170–175.
- [37] B. V. Herbruggen, J. V.-V. Gerwen, S. Luchie, Y. Durodie, B. Vanderborght, M. Aernouts, A. Munteanu, J. Fontaine, and E. D. Poorter, "Industrial UWB TWR and TDOA Localization Dataset in LOS/NLOS Scenarios," 2023. [Online]. Available: https://dx.doi.org/10.21227/tr65-4795
- [38] M. Kolakowski and V. Djaja-Josko, "TDOA-TWR Based Positioning Algorithm for UWB Localization System," in 2016 21st International Conference on Microwave, Radar and Wireless Communications (MIKON), 2016, pp. 1–4.
- [39] G. Boquet, A. Boquet-Pujadas, I. Pisa, A. Dabak, X. Vilajosana, and B. Martinez, "Indoor Position Estimation Using Angle of Arrival Measurements: An Efficient Multi-Anchor Approach with Outlier Rejection," *Internet of Things*, vol. 26, p. 101236, 2024. [Online]. Available: https://www.sciencedirect.com/science/article/pii/S254266052400177X
- [40] G. K. Fischer, T. Schaechtle, A. Gabbrielli, J. Bordoy, I. H"aring, F. H"oflinger, and S. J. Rupitsch, "A Systematic Survey and Comparative Analysis of Angular-Based Indoor

- Localization and Positioning Technologies," *IEEE Communications Surveys & Tutorials*, 2025.
- [41] P. Sambu and M. Won, "An Experimental Study on Direction Finding of Bluetooth 5.1: Indoor vs Outdoor," in 2022 IEEE Wireless Communications and Networking Conference (WCNC), 2022, pp. 1934–1939.
- [42] K. Xiao, F. Hao, W. Zhang, N. Li, and Y. Wang, "Research and Implementation of Indoor Positioning Algorithm Based on Bluetooth 5.1 AOA and AOD," Sensors, vol. 24, no. 14, 2024.
- [43] M. Nikodem, G. Trajnowicz, G. Salvatore de Blasio, and F. Alexis Quesada-Arencibia, "Experimental Evaluation of Multicarrier Phase Difference Localization in Bluetooth Low Energy," *IEEE Sensors Journal*, vol. 25, no. 1, pp. 1548–1560, 2025.
- [44] I. M. Khan, A. Thompson, A. Al-Hourani, K. Sithamparanathan, and W. S. T. Rowe, "RSSI and Device Pose Fusion for Fingerprinting-Based Indoor Smartphone Localization Systems," *Future Internet*, vol. 15, no. 6, 2023. [Online]. Available: https://www.mdpi.com/1999-5903/15/6/220
- [45] N. Chuku and A. Nasipuri, "RSSI-Based Localization Schemes for Wireless Sensor Networks Using Outlier Detection," *Journal of Sensor and Actuator Networks*, vol. 10, no. 1, 2021. [Online]. Available: https://www.mdpi.com/2224-2708/10/1/10
- [46] D. Janczak, W. Walendziuk, M. Sadowski, A. Zankiewicz, K. Konopko, M. Slowik, and M. Gulewicz, "Indoor Positioning Based on Bluetooth RSSI Mean Estimator for the Evacuation Supervision System Application," *IEEE Access*, vol. 12, pp. 55843–55858, 2024.
- [47] T. G. Hailu, X. Guo, H. Si, L. Li, and Y. Zhang, "Theories and Methods for Indoor Positioning Systems: A Comparative Analysis, Challenges, and Prospective Measures," Sensors, vol. 24, no. 21, 2024. [Online]. Available: https://www.mdpi.com/1424-8220/24/21/6876
- [48] X. Shen, B. Xu, and H. Shen, "Indoor Localization System Based on RSSI-APIT Algorithm," Sensors, vol. 23, no. 24, 2023. [Online]. Available: https://www.mdpi.com/1424-8220/23/24/9620
- [49] D. Dardari, A. Conti, U. Ferner, A. Giorgetti, and M. Z. Win, "Ranging With Ultrawide Bandwidth Signals in Multipath Environments," *Proceedings of the IEEE*, vol. 97, no. 2, pp. 404–426, 2009.
- [50] H. Wymeersch, S. Marano, W. M. Gifford, and M. Z. Win, "A Machine Learning Approach to Ranging Error Mitigation for UWB Localization," *IEEE Transactions on Communications*, vol. 60, no. 6, pp. 1719–1728, 2012.
- [51] T. Kazaz, G. J. M. Janssen, J. Romme, and A.-J. van der Veen, "Delay Estimation for Ranging and Localization Using Multiband Channel State Information," *IEEE Transactions on Wireless Communications*, vol. 21, no. 4, pp. 2591–2607, 2022.
- [52] A. Venus, E. Leitinger, S. Tertinek, and K. Witrisal, "A Graph-based Algorithm for Robust Sequential Localization Exploiting Multipath for Obstructed-LOS-Bias Mitigation," *IEEE Transactions on Wireless Communications*, 2023.
- [53] A. Venus, E. Leitinger, S. Tertinek, F. Meyer, and K. Witrisal, "Graph-based Simultaneous Localization and Bias Tracking for Robust Positioning in Obstructed LOS

- Situations," in 2022 56th Asilomar Conference on Signals, Systems, and Computers, 2022, pp. 777–784.
- [54] E. Leitinger, P. Meissner, C. Rüdisser, G. Dumphart, and K. Witrisal, "Evaluation of Position-Related Information in Multipath Components for Indoor Positioning," *IEEE Journal on Selected Areas in Communications*, vol. 33, no. 11, pp. 2313–2328, 2015.
- [55] C. Gentner, T. Jost, W. Wang, S. Zhang, A. Dammann, and U.-C. Fiebig, "Multipath Assisted Positioning with Simultaneous Localization and Mapping," *IEEE Transactions* on Wireless Communications, vol. 15, no. 9, pp. 6104–6117, 2016.
- [56] E. Leitinger, F. Meyer, F. Hlawatsch, K. Witrisal, F. Tufvesson, and M. Z. Win, "A Belief Propagation Algorithm for Multipath-Based SLAM," *IEEE Transactions on Wireless Communications*, vol. 18, no. 12, pp. 5613–5629, 2019.
- [57] E. Leitinger, S. Grebien, and K. Witrisal, "Multipath-Based SLAM Exploiting AoA and Amplitude Information," in 2019 IEEE International Conference on Communications Workshops (ICC Workshops), 2019, pp. 1–7.
- [58] H. Kim, K. Granström, L. Svensson, S. Kim, and H. Wymeersch, "PMBM-Based SLAM Filters in 5G mmWave Vehicular Networks," *IEEE Transactions on Vehicular Technology*, vol. 71, no. 8, pp. 8646–8661, 2022.
- [59] S. S. Chen, D. L. Donoho, and M. A. Saunders, "Atomic Decomposition by Basis Pursuit," *SIAM Journal on Scientific Computing*, vol. 20, no. 1, pp. 33–61, 1998.
- [60] J. A. Tropp and A. C. Gilbert, "Signal Recovery From Random Measurements Via Orthogonal Matching Pursuit," *IEEE Transactions on Information Theory*, vol. 53, no. 12, pp. 4655–4666, 2007.
- [61] D. Wipf and S. Nagarajan, "Iterative Reweighted ℓ_1 and ℓ_2 Methods for Finding Sparse Solutions," *IEEE Journal of Selected Topics in Signal Processing*, vol. 4, no. 2, pp. 317–329, 2010.
- [62] R. Giri and B. D. Rao, "Sparse Bayesian Learning With a Truncated Hierarchical Prior," *IEEE Transactions on Signal Processing*, vol. 66, no. 19, pp. 5141–5155, 2018.
- [63] M. E. Tipping, "Sparse Bayesian Learning and the Relevance Vector Machine," *Journal of Machine Learning Research*, vol. 1, pp. 211–244, 2001.
- [64] D. P. Wipf and B. D. Rao, "Sparse Bayesian Learning for Basis Selection," *IEEE Transactions on Signal Processing*, vol. 52, no. 8, pp. 2153–2164, 2004.
- [65] T. Park and G. Casella, "The Bayesian Lasso," Journal of the American Statistical Association, vol. 103, no. 482, pp. 681–686, 2008.
- [66] M. E. Tipping and A. C. Faul, "Fast Marginal Likelihood Maximisation for Sparse Bayesian Models," *International Workshop on Artificial Intelligence and Statistics* (AISTATS), 2003.
- [67] D. L. Donoho, A. Maleki, and A. Montanari, "Message Passing Algorithms for Compressed Sensing," *Proceedings of the National Academy of Sciences*, vol. 106, no. 45, pp. 18914–18919, 2009.
- [68] S. Rangan, "Generalized Approximate Message Passing for Estimation with Random Linear Mixing," 2011 IEEE International Symposium on Information Theory Proceedings, pp. 2168–2172, 2011.

- [69] S. Rangan, P. Schniter, and A. K. Fletcher, "Vector Approximate Message Passing," 2014 IEEE International Symposium on Information Theory, pp. 1588–1592, 2014.
- [70] S. Rangan, P. Schniter, A. K. Fletcher, C. Rush, and J. Vila, "Vector Approximate Message Passing," *IEEE Transactions on Information Theory*, vol. 65, no. 10, pp. 6664–6684, 2019.
- [71] D. T. M. Slock, "Convergent Approximate Message Passing by Alternating Constrained Minimization of Bethe Free Energy," in *Proceedings of the IEEE 7th Forum on Research and Technologies for Society and Industry Innovation (RTSI)*, Paris, France, Aug. 2022.
- [72] —, "Convergent approximate message passing," in *Proc. IEEE Int'l Mediterranean Conf. Communications and Networking (MEDITCOM)*, Athens, Greece, Sept. 2022.
- [73] M. J. Beal, "Variational Algorithms for Approximate Bayesian Inference," Ph.D. Dissertation, University College London, 2003.
- [74] X. Tan and J. Li, "Computationally Efficient Sparse Bayesian Learning via Belief Propagation," *IEEE Transactions on Signal Processing*, vol. 58, no. 4, pp. 2010–2021, 2010.
- [75] E. Riegler, G. E. Kirkelund, C. N. Manchon, M. R. Khanzadi, M. Jakobsson, P. Popovski, and B. H. Fleury, "Merging Belief Propagation and the Mean Field Approximation: A Free Energy Approach," *IEEE Transactions on Information Theory*, vol. 59, no. 1, pp. 588–602, 2013.
- [76] R. Ghods, C. Rush, and R. Rangan, "No-Parameter Tuning for Approximate Message Passing Using SURE," *IEEE Transactions on Signal Processing*, vol. 65, no. 2, pp. 287–294, 2017.
- [77] P. Mattsson, D. Zachariah, and P. Stoica, "Tuned Regularized Estimators for Linear Regression via Covariance Fitting," 2022, arXiv:2201.08756.
- [78] W. James and C. M. Stein, "Estimation With Quadratic Loss," Proceedings of the Fourth Berkeley Symposium on Mathematical Statistics and Probability, pp. 361–379, 1961.
- [79] C. M. Stein, "Estimation of the Mean of a Multivariate Normal Distribution," *Annals of Statistics*, vol. 9, no. 6, pp. 1135–1151, 1981.
- [80] Y. C. Eldar, "Generalized SURE for Exponential Families: Applications to Regularization," *IEEE Transactions on Signal Processing*, vol. 57, no. 2, pp. 471–481, 2008.
- [81] G. Pillonetto and G. D. Nicolao, "A New Kernel-Based Approach for Linear System Identification," *Automatica*, vol. 46, no. 1, pp. 81–93, 2010.
- [82] G. Pillonetto, F. Dinuzzo, T. Chen, G. D. Nicolao, and L. Ljung, "Kernel Methods in System Identification, Machine Learning and Function Estimation: A Survey," *Automatica*, vol. 50, no. 3, pp. 657–682, 2014.
- [83] B. Mu, X. Yuan, and L. Shen, "SURE-Based Regularization Parameter Selection for Signal Estimation Without Hyperparameter Tuning," *IEEE Transactions on Signal Processing*, vol. 66, no. 8, pp. 2011–2026, 2018.
- [84] C. K. Thomas and D. Slock, "Posterior variance predictions in sparse Bayesian learning under approximate inference techniques," in *IEEE Asilomar Conference on Signals*, Systems and Computers, Pacific Grove, CA, USA, Nov. 2020.

- [85] Y. C. Eldar, "Generalized SURE for Exponential Families," *IEEE Transactions on Signal Processing*, vol. 57, no. 2, pp. 471–481, 2009.
- [86] M. Triki and D. Slock, "Component-wise conditionally unbiased bayesian parameter estimation: General concept and applications to kalman filtering and lmmse channel estimation," in *Proceedings of the Asilomar Conference on Signals, Systems, and Computers*, Nov. 2005.
- [87] T. K. Moon, "The Expectation-Maximization Algorithm," *IEEE Signal Processing Magazine*, vol. 13, no. 6, pp. 47–60, 1996.
- [88] T. Heskes, O. Zoeter, and W. Wiegerinck, "Approximate Expectation Maximization," in Advances in Neural Information Processing Systems (NIPS), vol. 16, 2003.
- [89] Y. Tsaig and D. L. Donoho, "Extensions of Compressed Sensing," *Elsevier Signal Processing*, vol. 86, no. 3, pp. 549–571, 2006.
- [90] O. Y. Feng, R. Venkataramanan, C. Rush, and R. J. Samworth, "A Unifying Tutorial on Approximate Message Passing," Foundations and Trends in Machine Learning, vol. 15, no. 4, pp. 335–536, 2022.
- [91] T. Lesieur, F. Krzakala, and L. Zdeborová, "Constrained Low-Rank Matrix Estimation: Phase Transitions, Approximate Message Passing and Applications," *Journal of Statistical Mechanics: Theory and Experiment*, no. 7, p. 073403, 2017.
- [92] R. Berthier, A. Montanari, and P.-M. Nguyen, "State Evolution for Approximate Message Passing with Non-Separable Functions," *Information and Inference*, vol. 9, no. 1, pp. 33–79, 2020.
- [93] F. Caltagirone, L. Zdeborová, and F. Krzakala, "On Convergence of Approximate Message Passing," in *IEEE International Symposium on Information Theory (ISIT)*, 2014, pp. 1812–1816.
- [94] K. Takeuchi, "Convolutional Approximate Message-Passing," *IEEE Signal Processing Letters*, vol. 27, pp. 416–420, 2020.
- [95] A. K. Fletcher and P. Schniter, "Learning and Free Energies for Vector Approximate Message Passing," in *IEEE International Conference on Acoustics, Speech and Signal Processing (ICASSP)*, 2017, pp. 4247–4251.
- [96] G. Yi, W. Shengchu, and Z. Lin, "Approximate Message Passing Based Cooperative Localization in WSN with AOA Measurements," in *IEEE Wireless Communications and Networking Conference (WCNC)*, 2018, pp. 1–6.
- [97] J. Ma, G. Plonka, and M. Y. Hussaini, "Compressive Video Sampling with Approximate Message Passing Decoding," *IEEE Transactions on Circuits and Systems for Video Technology*, vol. 22, no. 9, pp. 1354–1364, 2012.
- [98] M. A. Beaumont, J.-M. Cornuet, J.-M. Marin, and C. P. Robert, "Adaptive Approximate Bayesian Computation," *Biometrika*, vol. 96, no. 4, pp. 983–990, 2009.
- [99] Y.-Y. Huang, Y.-W. Jing, and Y.-B. Shi, "Non-Parametric Mobile Node Localization for IoT by Variational Bayesian Approximations Adaptive Kalman Filter," *Cognitive Systems Research*, vol. 52, pp. 27–35, 2018.
- [100] M. Opper, O. Winther, and M. J. Jordan, "Expectation Consistent Approximate Inference," *Journal of Machine Learning Research*, vol. 6, no. 12, 2005.

- [101] M. Opper and O. Winther, "Expectation Consistent Free Energies for Approximate Inference," Neural Information Processing Systems (NeurIPS), vol. 17, 2004.
- [102] A. K. Fletcher, M. Sahraee-Ardakan, S. Rangan, and P. Schniter, "Expectation Consistent Approximate Inference: Generalizations and Convergence," in *IEEE International Symposium on Information Theory (ISIT)*, 2016, pp. 190–194.
- [103] F. Mogyorósi, P. Revisnyei, A. Pašić, Z. Papp, I. Törös, P. Varga, and A. Pašić, "Positioning in 5G and 6G networks—A Survey," *Sensors*, vol. 22, no. 13, p. 4757, 2022.
- [104] A. A. Saleh and R. Valenzuela, "A statistical model for indoor multipath propagation," *IEEE J. Sel. Areas Commun.*, vol. 5, no. 2, pp. 128–137, 1987.
- [105] G. Steinböck, T. Pedersen, B. H. Fleury, W. Wang, and R. Raulefs, "Distance dependent model for the delay power spectrum of in-room radio channels," *IEEE Trans. on Antennas and Propagation*, vol. 61, no. 8, pp. 4327–4340, 2013.
- [106] M. Triki and D. T. M. Slock, "Component-Wise Conditionally Unbiased Bayesian Parameter Estimation: General Concept and Applications to Kalman Filtering and LMMSE Channel Estimation," in *Proc. Asilomar Conf. Signals, Syst., Comput.*, 2005, pp. 670–674.
- [107] Z. Zhao, F. Xiao, and D. Slock, "Approximate Message Passing for Not So Large niid Generalized Linear Models," in 2023 IEEE 24th Int. Workshop on Signal Processing Advances in Wire. Commu. (SPAWC), pp. 386–390.
- [108] S. Rangan, P. Schniter, and A. K. Fletcher, "Vector Approximate Message Passing," 2018.
- [109] A. M. Graff, W. N. Blount, P. A. Iannucci, J. G. Andrews, and T. E. Humphreys, "Analysis of OFDM signals for ranging and communications," in *Proc. 34th Int. Tech. Meet. Satellite Div. Inst. Navig. (ION GNSS+ 2021)*, pp. 2910–2924.
- [110] A. Goldsmith, Wireless communications. Cambridge University Press, 2005.
- [111] J. Liu, "Be cautious when using the FIR channel model with the OFDM-based communication systems," *IEEE Trans. Veh. Technol.*, vol. 58, no. 3, pp. 1607–1612, 2008.
- [112] V. A. Aalo, C. Mukasa, and G. P. Efthymoglou, "Effect of mobility on the outage and BER performances of digital transmissions over Nakagami-*m* fading channels," *IEEE Trans. Veh. Technol.*, vol. 65, no. 4, pp. 2715–2721, 2015.
- [113] L. Mirsky, An introduction to linear algebra. Courier Corporation, 2012.
- [114] S. Borman, "The expectation maximization algorithm-a short tutorial," *Submitted for publication*, vol. 41, 2004.
- [115] D. R. Hunter and K. Lange, "A Tutorial on MM Algorithms," Am. Stat., vol. 58, no. 1, pp. 30–37, 2004.
- [116] T. P. Minka, "Expectation propagation for approximate Bayesian inference," arXiv preprint arXiv:1301.2294, 2013.
- [117] H. Buchholz, The confluent hypergeometric function: with special emphasis on its applications. Springer, 2013, vol. 15.
- [118] A. U. Ahmed, R. Arablouei, F. d. Hoog, B. Kusy, N. Bergmann, and R. Jurdak, "Nakagami-m distribution of RSSI in shadowing pathloss model for indoor localization," in *IEEE Sensors Appl. Symp. (SAS)*, 2019, pp. 1–6.

- [119] M. Opper and O. Winther, "Expectation Consistent Approximate Inference," J. Mach. Learn. Res., vol. 6, no. 73, pp. 2177–2204, 2005.
- [120] R. M. Neal and G. E. Hinton, "A view of the em algorithm that justifies incremental, sparse, and other variants," in *Springer: Learning in graphical models*, 1998, pp. 355–368.
- [121] F. Xiao and D. Slock, "Parameter Estimation Via Expectation Maximization Expectation Consistent Algorithm," in *IEEE Int. Conf. Acoust. Speech Signal Process.* (ICASSP), 2024, pp. 9506–9510.
- [122] "Study on channel model for frequencies from 0.5 to 100 ghz," 3GPP, Technical Report TR 38.901, 2024, release 18.